Unraveling Mechanisms and Quantifying Active Sites by Using *in-situ* and *ex-situ* Infrared Spectroscopy

By

Shao-Chun Wang

A dissertation submitted in partial fulfillment of

the requirements for the degree of

Doctor of Philosophy

(Chemistry)

at the

UNIVERSITY OF WISCONSIN-MADISON

2022

Date of final oral examination: 5/6/2022

The dissertation is approved by the following members of the Final Oral Committee:

Ive Hermans, Professor, Chemistry and Chemical & Biological Engineering
Song Jin, Professor, Chemistry (Material Chemistry)
Thomas C. Brunold, Professor, Chemistry (Inorganic Chemistry)
John F. Berry, Professor, Chemistry (Inorganic Chemistry)

Acknowledgements

First of all, I would like to thank Professor Ive Hermans gave me the opportunity to learn and conduct research in University of Wisconsin-Madison. I really appreciate the freedom and the time you gave me to discover the interesting topic in heterogeneous catalysis. I would also like to thank my committee members, Professor Song Jin, Thomas Brunold, and John Berry for taking their time giving me suggestions on my research dissertation. Haiyang, Ahmad, Prasad, and Ivan from BASF Corporation provided information and opinions on the Cu-CHA work and I am grateful that we succeed to the goal as a team.

During the time in the Hermans group, I feel very happy and energetic every day because of the group environment and members. Phil taught me MES and IR technique as the start in the lab. Joe and Juan were always very helpful on the reaction kinetic questions. Sam showed me how to operate Autochem and we usually went out for lunch during workday. I always remember that Alyssa and Sarah helped me finish the proposal until late night just before Christmas. Will always answered my questions for Swagelok parts which I learned a lot. Also, Melissa proofread most of my writings and gave nice suggestions and edited text. I am very glad I had the opportunity to help Theo, Natalie, Jacob, Son, Conner, Abdullah, Edgard, Unni, Faysal, and Ryan on their projects and I also learned new knowledge and ideas when discussing with them! Although there is only short time overlapped, I also gain new concept from Lesli, Peter, Matias, and Kevin. In addition, Steve, supervisor of the machine shop, is very patient and helpful on the instrument design; without his design, it is very difficult to conduct some of the *in-situ* IR experiments. The administrative staff in Chemistry, especially Arrietta, I always feel refresh after talking our life in Madison and the possible career in the future for a Chemistry student.

I would also like to thank the support from my family, dad, mom and my sister. The frequency they came to Madison to visit me is more than I went home. Zoey supported me to finish my PhD study and tolerated my anxiety and impatience when I had a hard time with the experimental results and exams. I am also glad that I have my roommates and friends in Madison who played softball with me and we went hiking on the weekends which I can relax from the research. Thanks everyone who helped and accompanied me during my time in Madison!

Abstract

The molecular-level understanding of surface sites and reaction mechanisms is key for the development of the field of heterogeneous catalysis. Infrared spectroscopy, studying molecular vibrations, is widely used to investigate the structures of surface-bound species in heterogeneous catalysts. Heterogeneous catalytic reactions proceed *via* adsorption of the reagent(s), surface reaction, and desorption of the product(s), leading to complex *in-situ* or *operando* IR spectra. However, the information of active species is usually concealed by spectator species which do not participate in the catalytic cycle. Modulation excitation spectroscopy serves as a tool to increase the signal-to-noise level and to differentiate between the active species and spectator species during a catalytic reaction. In Chapter 2, we report on the use of diffuse reflectance FT-IR spectroscopy (DRIFTS) with a modulation excitation (ME) approach followed by mass spectrometry (MS) to investigate the reaction of ethanol to *n*-butanol over hydroxyapatite (HAP). The approach allows for a vibrational characterization of the active surface species and the formulation of a consistent mechanism. Based on our experimental observations, Ca^{2+}/OH^- can be put forward as the main active site for the aldol condensation. POH/OH^- acid-base pair is proposed as the active site for the Meerwein-Ponndorf-Verley (MPV) direct hydrogen transfer for the *n*-butanol formation.

In Chapter 3, we describe the use of NO as a probe molecule in low-temperature IR spectroscopy to identify and quantify copper species in the state-of-the-art commercial NO_x abatement catalyst, Cu ion-exchanged chabazite zeolite. While bulk analysis can reveal the total concentration of copper in the catalyst, the amount of ion-exchanged copper is more difficult to determine due to the appearance of non-exchanged Cu species, CuO_x. Molecules such as carbon monoxide (CO) and nitric oxide (NO) are routinely used as a probe to investigate the copper speciation in order to draw structure-

activity correlations. However, NO is easy to decompose and reacts with copper species at ambient temperature, causing complexity in IR spectra. Here, we develop NO adsorption IR spectroscopy at cryogenic conditions to avoid the undesired reactions. The observed IR peaks for $Cu^{+}(NO)_2$ and $Cu^{2+}(NO)$ species can be used to quantify the amount of exchanged copper species in a broad range of samples, including a commercial wash-coated honeycomb. Calibration curves for $Cu^{+}(NO)_2$ and $Cu^{2+}(NO)$ are determined for copper loadings up to 3.99 wt% with silica to alumina ratio of 16-22 and quantitative agreement with complementary hydrogen temperature-programmed reduction (H_2-TPR) results is established. Our methodology allows us to identify different Cu species in Cu-CHA, such as $Z_2Cu(II)$, $Z_1Cu(II)OH$ and Cu dimers, based on their distinct IR signatures. In addition, the perturbed T-O-T framework vibration – characterized at 400 ^{o}C – can also be used as a complementary method to quantify $Z_2Cu(II)$ species. This work demonstrates that cryogenic NO-IR is a facile technique to identify and quantify the exchanged copper species in Cu-CHA to accelerate catalyst development.

In chapter 4, we extend the NO-IR method to characterize the ion-exchanged species in Cu-ZSM-5 and Fe-CHA. The adsorbed NO shows distinct IR characteristics for exchanged copper species at 1914 cm^{-1} and the calibration curve for Cu^{2+} species for estimating high Cu-loading Cu-ZSM-5 is determined. In the case of Fe-CHA, the NO-IR is not efficient due to the formation of NO monomer and trimer on copper species, causing complexity in the IR spectra. Carbon monoxide (CO) is then applied as an alternative probe molecule. The results of CO-IR for Fe-CHA showed more defined IR features for $Fe^{2+}(CO)$ than in NO-IR. With this toolbox in hand, the calibration curve for the concentration of Fe^{2+} in Fe-CHA by CO-IR is then established.

Perspectives for future research are outlined in Chapter 5, the preliminary results for

a Cu-Ga binary catalyst for methanol production from CO_2 hydrogenation was tested by using the DRIFTS cell with ambient pressure. However, due to thermodynamic limitation, the reaction favors reverse water gas shift under ambient pressure. The newly designed *operando* DRIFTS cell allows to minimize the exchange time of concentration modulation and have the capability of holding at high pressure (> 25 bar) and high temperature (> 250 ^{o}C) which is suitable for investigating the heterogeneous catalysts for CO_2 hydrogenation. With the well-establish tool, we will be able to investigate surface-bound species and reaction mechanisms under working conditions by IR spectroscopy.

Not only can gas phase catalytic reactions be studied by DRIFTS, but heterogeneous catalytic reactions in liquid phase can also be investigated by attenuation total reflection IR spectroscopy (ATR-IR). Competitive adsorption with reactants and solvents is especially important in the case of (micro-) porous catalysts where the composition inside the pores can be very different from the bulk due to size exclusion and confinement effects. ATR-IR with the ME approach can shed light on mechanistic insights for liquid phase reactions.

Lastly, with the success of low temperature NO and CO-IR method development, characterizing different metal ion-exchanged zeolites for various applications such as methane to methanol, syngas to dimethyl ether, and NO_x abatement is crucial for structure-reactivity correlation. Ultimately, low temperature NO and CO-IR can be established as facile techniques to identify and quantify metal ion species located in different types of zeolites.

Table of Content

Chapter 1: Introduction

1.1 Heterogeneous Catalysis

Heterogeneous catalysis is the core technology for many industrial processes, due to the enhancement of reaction rate with low cost, high conversion, and high product selectivity. Over 85% of chemical production is produced by using heterogeneous catalysts.[1-2] The catalyst market is evaluated to be USD 33.9 billion with an anticipated annual growth rate of 4.4% from 2020 to 2027.[3] With the increased attention to renewable energy, environment protection, and waste upcycling, the demand for heterogeneous catalysts with low cost and high efficiency is rising. For example, carbon dioxide (CO_2), one of the key greenhouse gases, can be hydrogenated to valuable chemical products, such as methanol to mitigate the CO_2 concentration in the atmosphere.[4-8] In order to enhance and improve the activity and selectivity of the heterogeneous catalyst, understanding the structures and active sites of heterogeneous catalysts with the attempt to elucidate the reactivity is the key for catalysis research.

The signature feature of heterogeneous catalysis is that the phase of reactants and products differ from the phase of a catalyst. The main advantage of heterogeneous catalysts is efficiently in product separations with catalysts. In addition, heterogeneous catalysts can be easily recycled and regenerated after several rounds of reaction cycles compared to homogeneous catalysts in which reactants, products, and catalysts are all in the same phase. The heterogeneous catalytic reactions are mostly solid-gas and solid-liquid phase interactions. In other words, gas or liquid reactants contact the active sites on the solid catalyst to lower the activation barrier of the reaction. A heterogeneous catalytic reaction involves adsorption, surface reaction, and desorption.[9] During a catalytic reaction, the interaction of reactant(s) and active sites, formation of

intermediate(s), and product(s) desorption from active sites are key steps to heterogeneous catalysts.[10]

The active sites can be metals, acids, or bases.[11-15] For example, catalysts with platinum-group metals are used for hydrogenation reactions due to the ability to activate molecular hydrogen into the atomic hydrogen.[16-17] Acid catalysts such as zeolites are applied for catalytic cracking[18-19] and methanol to hydrocarbons[20-21] because of the appearance of Brønsted acid sites and high surface area to promote the dehydration reactivity. Base catalysts such as metal oxides,[22-23] such as magnesium oxide (MgO),[24-26] are often used as the catalyst support to enhance the capability of dehydrogenation due to the enhanced ability to abstract proton to the oxide. Structure-activity relationships drive the understanding of the underlying reaction mechanisms, allowing the design of more active and selective heterogeneous catalysts. However, establishing the mechanisms of chemical reactions in heterogeneous catalysis is challenging due to the complexity of the catalysts. For instance, different solid supports for metals can alter the catalytic efficiency because of the appearance of other surface species or changing the oxidation state of the metal.[27-30] In addition, porous materials such as zeolite as a support can also enhance the catalyst reactivity due to the enhanced surface area.[31-32] Some studies even pointed out that the synergistic effect of acid-base pairs is important for catalysts with different sites or supports, which can further increase the catalytic efficiency.[33-37] To address these complexities, a technique capable of probing surface sites on catalysts and the interactions between active sites and reactants is the key. Several different techniques have been developed, and this thesis focuses on the implementation of such as approach for vibrational spectroscopy.

1.2 Fourier Transform Infrared Spectroscopy (FT-IR) in Heterogeneous Catalysis

Fourier Transform Infrared Spectroscopy (FT-IR), a vibrational spectroscopy, is widely used to investigate the structures of surface-bound species in heterogeneous catalysts.[38-40] Because different chemical species have distinct IR absorption features, IR spectroscopy can reveal fingerprints of a catalytic reaction. This powerful tool can also be applied to *in-situ* or *operando* spectroscopy to explore the key intermediates under reaction conditions.[40-42] This technique can be extended by using probe molecules to reveal the surface sites by investigating the interactions between adsorbates.[43-45] The changes in the vibrational frequency of probe molecules depend on how probe molecules geometrically and electronically interact with the surface sites in heterogeneous catalysts. Therefore, the spectral information is sensitive to the structures of surface sites, which may provide a valuable connection to the catalysts' performance.

In order to characterize the details of surface sites on solid catalysts, some essential factors need to be considered for the probe molecules: 1) the size of the molecule in order to enter porous catalysts and monitor all accessible surface sites, 2) detectable by infrared and show distinct IR features for different surface sites, 3) high molar extinction coefficients to ensure sensitivity, 4) the capability for quantitative determinations and, 5) background signal with the catalyst support should be insignificant to avoid the interference.[45] Some examples of probe molecules are provided below.

Probe molecule I: Pyridine

Pyridine has been a well-established probe molecule for decades to study acidic heterogeneous catalysts. The Lewis acid and Brønsted acid sites in catalysts can be identified and quantified by the adsorbed pyridine. While the adsorbed pyridine behaves as a pyridinium ion on Brønsted acid site at 1540 cm^{-1}, the nitrogen atom on pyridine acts

as an electron donating group to coordinate with the electron deficient Lewis acid site, which shows a different IR feature at 1455 cm^{-1} (**Figure 1.1**).[46-47] The extinction coefficients for both Brønsted acid sites and Lewis acid sites could be determined by carefully performing controll experiments.[48-52] In short, zeolite samples were pelletized into self-supported IR wafers and pretreated at 450 ^{o}C under vacuum to remove adsorbed water on the sample surface. Pyridine was then added stepwise with the amount of 2 μmol at 150 ^{o}C to prevent any pyridine physisorption, whereas IR spectra were collected after each 2 μmol pyridine dosage. As a result, the intensity of the IR peak for pyridine chemisorption increased until the surface acid sites were staurated.[48] The amount of the adsorbed pyridine can then be recorded. The extinction coefficients for IR feature at both Brønsted acid sites and Lewis acid sites at 1540, and 1455 cm^{-1}, respectively, can be obtained by applying Beer's law.[53] $A = \varepsilon bc$, where A is the absorbance from transmitted IR, b is path length, c is the concentration, and ε is the molar extinction coefficient. Therefore, the estimated Lewis acid and Brønsted acid site density can then be correlated with its catalytic reactivity to benefit catalyst development.

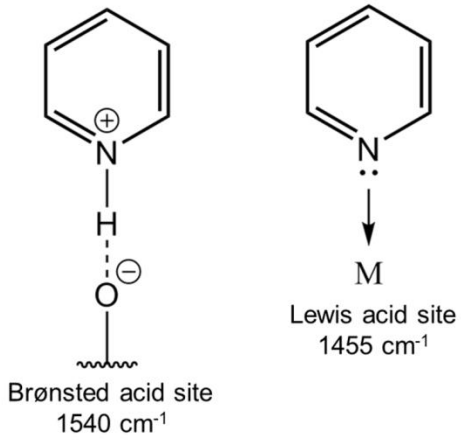

Figure 1.1. Schematic of adsorbed pyridine on Brønsted acid site and Lewis acid site.

In previous literature, the amount of the adsorbed pyridine was obtained from the partial pressure change by sequential pyridine dosage into the IR cell.[48] In this case, the pyridine can also adsorb on the wall of the IR cell or tubing, which is taken into account for the pressure change for the concentration calculation, leading to imprecise results. In responding to this issue, introducing high-precision thermogravimetry as a complementary method has been reported.[54] By combing pyridine adsorption IR with thermogravimetry, the systematic error in extinction coefficients can be resolved, establishing more precise extinction coefficients, especially for individual acid catalysts such as ZSM-5, BEA, and FAU zeolites.[54] In this technique, there is an incorporative microbalance in the *in-situ* IR cell which gives high accuracy to correlate with the weight change and pyridine adsorbed IR peaks. With this tool in hand, it has been observed that the molar extinction coefficients for Brønsted acid sites are dependent on the types of zeolite structures, such as ZSM-5, BEA, MOR, and FAU. Especially, FAU showed more than 40% difference in extinction coefficient than the value of ZSM-5. In contrast, the molar extinction coefficients for Lewis acid sites are independent to the structure. Therefore, gravimetric analysis and IR (AGIR) can be a precise benchmark for further pyridine adsorption IR investigations in comparing for different types of catalysts.

Pyridine can also assess and compare the surface acidity among various transition metal impregnated catalysts.[55-60] The strength of the acid site can be revealed by stepwise increased temperature in the IR cell. In other words, based on the pyridine desorption temperature on the surface, we can benchmark the strength of the acid site. However, the disadvantage of using pyridine as a probe is that it has a kinetic diameter size of 0.533 nm which means pyridine will encounter difficulties when investigating catalysts with microporous structures, because it may not be able to access the acid sites in the pore.[61-62]

Probe molecule II: Carbon Monoxide (CO)

The formation of carbonyl species on the surface from carbon monoxide (CO) adsorption has been studied for decades.[63-67] CO can interact with metal sites on catalysts' surfaces with different IR features, indicating the nature of the metal sites. The metal sites can be formed by using transition-metal or alkaline cations. Below are the three main factors that can alter the vibrational frequency of the carbon-oxygen (C-O) bond (**Figure 1.2**).[45] 1) The local electric field determined by the types of metal cations can affect the polarization of CO molecules. The C-O stretching frequency of affected CO molecules shifts to higher wavenumbers (blueshift) compared to the gas-phase CO at 2143 cm^{-1}. The blueshift of the C-O stretching frequency is attributed to the increased force constant and the shortened bond length of the C-O bond. 2) The lone electron pair in CO donates to the acceptors, such as a metal cation with empty orbitals (*i.e.,* Lewis acid site). In this case, a formation of σ-coordination from CO to metal cation leads the C-O bond order to increase due to the loss of electrons from σ^* orbital.[68] The outcome of σ-coordination drives the C-O stretching frequency higher than gas-phase CO, which is also a blueshift. In addition, the higher blueshift observed, the stronger the σ interaction, which can provide insights into the Lewis acid strength of the metal sites.[67, 69] 3) With the partially filled d-orbitals in some transition-metal cations or metal nanoparticles, the π-donation from metal sites to CO can occur. This leads to the increased electronic density in the CO anti-bonding orbitals, resulting in decreased C-O bond energy and elongated bond length of C-O bond, which cause the redshift of C-O stretching frequency as compared to gas-phase CO. The π-donation from metal sites is pronounced in platinum-group metals, and has been well-characterized by single crystals, such as Pt, Pd and Rh.[70-71] Three possible C-O stretching modes has been observed and reported elsewhere: a) linear carbonyls (on-top sites) at 2130-2000 cm^{-1}, b) 2-fold bridged

carbonyls at 2000-1850 cm^{-1}, and c) 3-fold bridged carbonyls (on hollow sites) can be found at 1920-1800 cm^{-1}.[72-73]

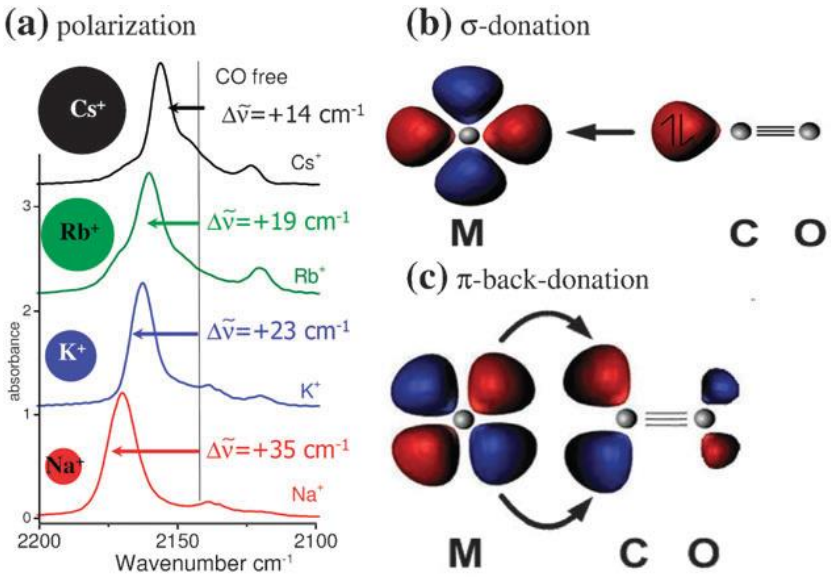

Figure 1.2. Three different interactions between CO and metal center: (a) electrostatic interaction, causing ν(CO) to blue-shift, (b) σ* electron donation from CO to empty orbital of metal center, leading ν(CO) to blue-shift, and (c) π* electron donation from metal center to CO, leading ν(CO) to red-shift. Adapted from ref 45.

Probe Molecule III: Nitric Oxide (NO)

Nitric oxide (NO) is a similar probe to CO, but with one extra electron in the π* orbital.[63, 74-76] The adsorption of NO to alkaline cations causes the blueshift of N-O stretching frequency due to the electrostatic interaction which is the same case of CO adsorption. Although NO can adsorb on metal sites with the formation of nitrosyl species similar to the carbonyl in CO adsorption, the interaction energy of NO on the surface is weaker than CO due to NO as a radical character and tendency to dimerize to form a more stable N_2O_2 species.[77] As a result, the adsorbed NO species on metal sites are

mostly dimeric or even trimeric which makes the IR spectra more complex. In addition, NO is more reactive than CO at room temperature on metal sites, leading to decomposition or reaction which increases the complexity to interpret the spectral features. In order to eliminate the NO decomposition or reaction, operating NO adsorption at a low temperature (~100 K) environment can avoid the undesired reaction.[78]

The most significant difference of the extra electron in π^* orbital in NO is that NO can establish a stronger bonding character on metal sites with respect to CO. The π^* back donation from NO to metal center enhance the bond order in NO, resulting in a pronounced blueshift of NO stretching frequency. This effect gives distinct IR feature when metal sites with several oxidation states.[45] For example, when NO adsorbs on Cu ion-exchanged zeolite such as Cu-CHA, the IR feature of NO adsorption on Cu^{2+} ion at 1887-1950 cm^{-1} differs from NO adsorption on Cu^{+} ion at 1807 cm^{-1}, showing the capability to clearly distinguish different oxidation states of copper on the same surface.[79]

Operando (*in-situ*) IR spectroscopy

Besides of the applied probe molecules to characterize the catalysts' surface by IR spectroscopy, *operando* IR spectroscopy can provide a direct investigation to probe catalytic systems during reaction conditions.[42, 80-83] The strength of the IR spectroscopy for catalyst characterization is that it can provide the details about an active catalyst and mechanistic insight in a reaction process. Therefore, expanding the IR spectroscopy to monitor the reaction process under a given condition may elucidate key intermediates that determine the catalytic activity and selectivity. The *operando* spectroscopy is critical because of the dynamic nature of the catalysts under reaction conditions. This type of spectral information contrasts with the standard spectroscopy protocol without operating

under working conditions, which can be less relevant for probing reaction mechanisms directly associated with the catalytic performance. Thus, collecting IR spectroscopy under catalyst's working conditions is an important way to compare with the characterization of fresh and spent catalysts.

Modulation excitation spectroscopy (MES)

Although *operando* IR spectroscopy can reproduce surface interaction under reaction conditions, the interpretation of the experimental spectra quickly becomes challenging due to the occurrence of various physical and chemical phenomena at the same time. In heterogeneous catalytic systems, the adsorption/desorption of different species and the formation of the products take place simultaneously, resulting complex IR spectra for relatively simple systems in *operando* spectroscopy. One of the main challenges is to differentiate between actual intermediates, so-called active species, and species that adsorb but do not play an essential role in the reaction mechanism, so-called spectator species. Unfortunately, signals from spectator species usually overshadow the experimental spectra making it challenging to draw reliable mechanistic conclusions.

Modulation excitation spectroscopy (MES) combine with IR spectroscopy has shown potential to detangle signals from the active species and spectator species.[84-89] MES works similarly to a lock-in amplifier and makes use of the orthogonality of sinusoidal functions.[90] The basic concept is to stimulate a system with an external parameter such as temperature, reagent concentration, pressure, pH, or radiation in a periodic manner.[91] In most of the heterogeneous catalytic system, concentration modulation is widely used and easy to apply. The system will then be perturbed by a concentration change with the frequency ω and the response of the signal will oscillate with the same frequency ω, but

with a specific time delay ∆t (**Figure 1.3**). After several modulations to reach a quasi-steady state, the random noise and spectator species which are not involved in the catalytic reaction mechanism will not be affected by the perturbation. In other words, the signals coming from active species can be isolated from the bulk. In addition, phase-sensitive detection (PSD), the mathematical treatment that converts spectra from the time domain into the phase domain indicating a phase delay ϕ for active species.[92] The equation for phase-sensitive detection is described as follow:

$$A_k\left(\varphi_k^{PSD}\right) = \frac{2}{T}\int_0^T A(t)\sin\left(k\omega t + \varphi_k^{PSD}\right)dt \qquad (1.1)$$

During the catalytic reaction, each different active species (*i.e.,* intermediates) could reveal distinct phase delays in its IR signal which are the hints for micro-kinetic analysis. For example, in the ideal case of a two-step reaction A → B → C, the IR signals of the different species will show distinct phase delay as $\phi_A < \phi_B < \phi_C$. The consecutive appearance of the reactive species and the correlation of the phase delay allows for investigating the reaction pathway. The PSD spectra can also be able to differentiate the heavily overlapped IR peaks, assuming the species exhibit different kinetics during modulation. In addition, with averaging the spectra over several periods, the results lead to enhanced signal-to-noise in which we can observe some weak signals that we usually won't find in *operando* spectroscopy. Although the MES and PSD are based on mathematical sine-wave stimulation, square-wave modulations are commonly used in concentration modulations due to the ease of the setup.

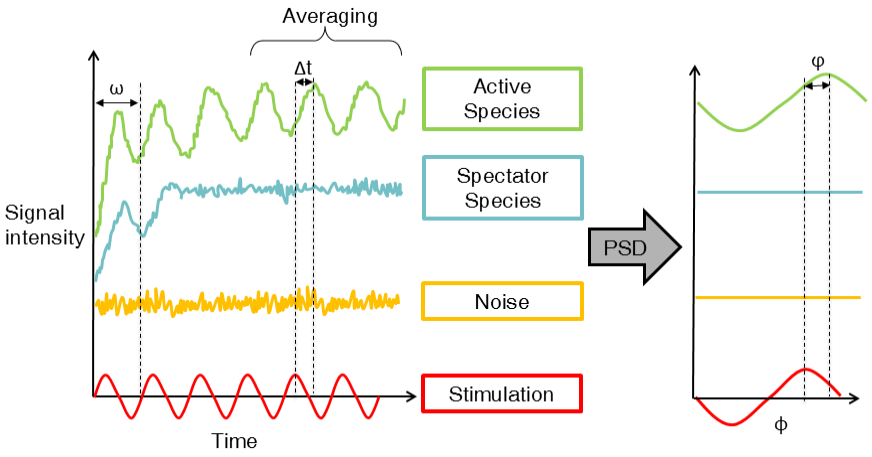

Figure 1.3. Working principle of MES. PSD yields micro-kinetic information while filtering out unwanted signals originating from spectator species or noise. Adapted from ref 84.

Attenuated total reflection FT-IR spectroscopy (ATR-IR)

Attenuated total reflection FT-IR (ATR-IR) spectroscopy is an appropriate sampling technique to detect the solid-liquid interactions in liquid phase heterogeneous catalytic reactions.[93-96] The solid catalysts can be deposited on IR internal reflection elements (IRE) such as ZeSe, Si, or ZnS and the liquid containing reactants can be flowed through the IRE to make contact with the surface site on the deposited catalysts. The IR beam will pass through the bottom of the IRE and generate a single or multiple total reflections from the surface of IRE (**Figure 1.4**). The IR absorbance signals will then be collected by an MCT detector. The important factors for investigating solid-liquid interactions in ATR-IR are the penetration depth of IR beam and thickness of the solid catalyst's layer. In fact, the evanescent wave for the penetration depth which can be calculated by the equation:[97-98]

$$d_p = \frac{\lambda}{2\pi\sqrt{(n_1^2 sin^2(\theta) - n_2^2)}} \qquad (1.2)$$

Where λ is the wavelength, n_1 and n_2 are the refractive indices of the IRE and sample, respectively, and θ is the angle of incidence of IR beam. For our case, n_1 = 2.4

for ZnSe, n_2 = 1.2 for the catalyst/solvent mixture,[96] and the angle of incidence θ is 45°. The choice of λ depends on the wavenumber of interest in the IR spectrum. Therefore, the solid thickness needs to be carefully considered. If the thickness of the catalyst layer is bigger than the penetration depth, the ATR-IR spectrum would not include the information from bulk solution which can ensure the observed vibrational absorbance is either the adsorbed species on the surface sites or the diffusion of the solvent molecule into catalyst's structure. In contrast, if the catalyst layer is smaller than the penetration depth, the ATR-IR spectrum would contain vibrational information from both surface interactions and bulk solution which usually cause complexity in the spectra.

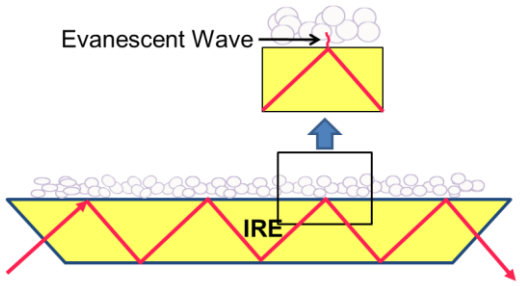

Figure 1.4. Catalyst coated on an Internal Reflection Element (IRE) and the formation of the evanescent wave.

Diffuse reflectance Infrared Fourier Transform spectroscopy (DRIFTS)

The diffuse reflectance Infrared Fourier Transform spectroscopy (DRIFTS) is a sampling technique to monitor the vibration of solid-gas interactions in gas phase heterogeneously catalytic reaction.[99-101] The solid catalysts can be placed into a porous ceramic cup without any sample preparation compared to ATR-IR and the conventional transmission IR. The gas phase reactant can flow through the catalyst to contact with the surface sites while the IR beam focuses on catalyst's surface and the diffuse reflection IR

signal is collected by MCT detector. (**Figure 1.5**) In addition, other than the advantage for simple sample preparation of this technique, the sample can be easily raised to high temperature or high pressure due to the design of the IR cell which can simulate the working condition of the catalyst. Although the technique seems suitable for studying the IR vibrations of gas-solid interactions, the IR signal intensities are relatively weak comparing to ATR-IR and transmission IR because of the intensity loss from diffuse reflection. In addition, the particle size of catalyst and packing of the bed might influence the results of the measurement which make quantitative study more difficult by using DRIFTS.[102-104] The IR signals contributions from gas phase molecule can sometimes overwhelm the gas-solid interaction IR features which appropriate reference spectrum is needed. Therefore, combing MES with DRIFTS can improve and eliminate the unwanted signal from the catalytic system which we will discuss in the next chapter.

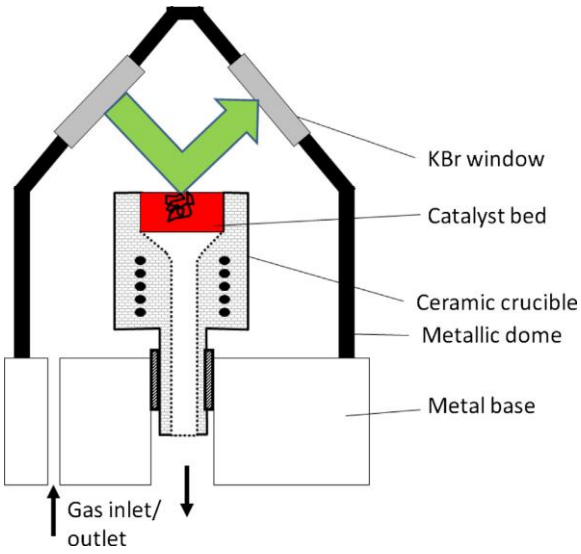

Figure 1.5. Schematic of DRIFTS cell. Adapted from ref 105.

1.3 Scope of the Thesis

This thesis includes the case study of an *in-situ* (*operando*) and *ex-situ* FT-IR research. In chapter 2, we applied MES to DRIFTS in order to discern a reaction

pathway with several consecutive reaction steps of bio-ethanol to *n*-butanol via hydroxyapatite (HAP) as a catalyst. In chapter 3, we showcase the power of NO as probe molecule in transmission IR spectroscopy and develop a low temperature FT-IR methodology to identify and quantify the copper species in a commercialized NO_x abatement catalyst, Cu-CHA. In chapter 4, we further applied the low temperature FT-IR technique in Cu-ZSM-5 and Fe-CHA, indicating the wide opportunity for this method. Finally, perspectives for the mechanistic IR study by using *operando* MES in other undiscovered system to benefit fundamental research and catalyst development.

Chapter 2: Insights into Ethanol Coupling over Hydroxyapatite Using Modulation Excitation *Operando* Infrared Spectroscopy

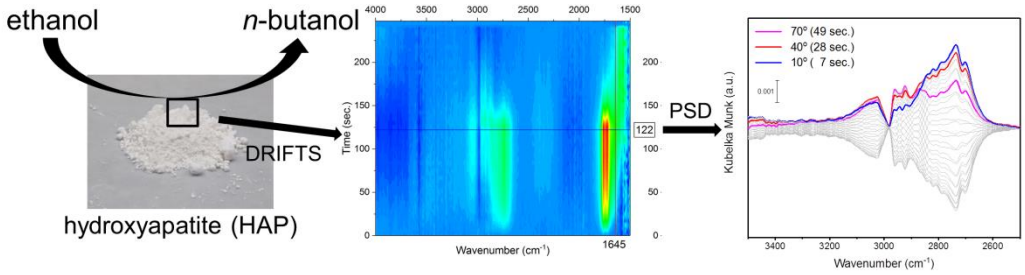

This chapter showcases the capability of MES-DRIFTS-MS to investigate the ethanol upgrading reaction *via* hydroxyapatite (HAP). The reaction mechanism and possible acid-base pairs for each reaction step were elucidated. This work was published in ChemCatChem.[105]

2.1 Introduction

With the increased corn-based bio-ethanol production in the United States, the catalytic upgrading of ethanol to more valuable chemicals such as higher alcohols and alkenes has drawn renewed interest. Special attention is geared towards *n*-butanol – the simplest upgrading product, formed from condensation of two ethanol molecules – because of its wide range of applications such as a fuel additive, a solvent, and additive in perfumes, amongst others.[106] When used as a fuel additive, *n*-butanol is superior to ethanol because of its higher energy density, and the fact that it is less corrosive and less water soluble.[107] The conventional petrochemical route for synthesizing *n*-butanol is hydroformylation of propylene to butanal, and the subsequent hydrogenation of butanal to *n*-butanol. The hydroformylation process to synthesize *n*-butanol requires high pressures and uses homogeneous cobalt, rhodium, palladium, or ruthenium catalysts,[108-

[109] which are expensive and create separation issues. Hence, there exists an interest to explore alternative approaches to produce *n*-butanol under milder conditions using heterogeneous catalysts, and preferably starting from a biomass-derived feedstock. The Guerbet reaction offers one attractive alternative route for producing *n*-butanol from ethanol through C-C bond formation and hydrogenation.[110-113]

Several heterogeneous catalysts have been investigated for the Guerbet reaction including metal oxides, zeolites, hydroxyapatite, and supported metals.[114-115] Those studies indicate that hydroxyapatite ($Ca_{10}(PO_4)_6(OH)_2$, HAP) shows promising conversion (10%) and selectivity toward *n*-butanol (75%) under atmospheric condition because of its favorable acid-base properties.[116-119] The widely accepted description of the reaction involves four main steps as depicted in **Scheme 2.1**.[111, 114, 117, 120-121] Ethanol first dehydrogenates/oxidizes into acetaldehyde, followed by acetaldehyde self-aldol condensation. Under the reaction conditions, the aldol addition product dehydrates very rapidly to form crotonaldehyde. Crotonaldehyde is then transformed to crotyl alcohol in a first hydrogenation. Finally, crotyl alcohol is converted to *n*-butanol through a second hydrogenation. This reaction pathway has been established using conventional kinetics and steady-state isotopic transient kinetic analysis (SSITKA). The latter revealed that acetaldehyde, obtained from ethanol dehydrogenation, remains on the surface to undergo consecutive reactions to generate *n*-butanol.[122] However, there is still a debate on the second hydrogenation step from crotyl alcohol to *n*-butanol. Two different hydrogenation pathways have been suggested in the literature and are summarized in Scheme 1. The first pathway is a surface-mediated hydrogenation of the C=C bond of crotyl alcohol, where the surface hydrogen comes from ethanol dehydrogenation in the first step.[123] In an alternative mechanism, crotyl alcohol first isomerizes and tautomerizes to butanal. The C=O can then be directly hydrogenated by ethanol *via* the Meerwein-

Ponndorf-Verley (MPV) reaction to form *n*-butanol.[124-125] We propose to take another approach to investigate ethanol coupling over HAP to clarify the second hydrogenation step and gain a deeper understanding of the reaction mechanism in general that could potentially benefit future catalyst design.

Ho *et al.* reported Ca-O species to be responsible for ethanol dehydrogenation and direct hydrogen transfer, while the self-aldol condensation of acetaldehyde is proposed to occur on CaO/PO_4^{3-} as an acid-base pair as identified in CO_2 titration experiments.[124] On the other hand, the OH^-/POH acid-base pair was suggested to be the active site for ethanol coupling over HAP by applying the amphoteric probe molecule, acetylene, using IR spectroscopy.[126] Hill *et al.* also investigated the surface sites on HAP using CO_2, pyridine, acetylene, and glycine adsorption, and found that it is possible to have Ca^{2+} and POH as acid sites and OH^- as a basic site on HAP.[127] Recently, Ca^{2+}/OH^- and POH/OH^- were reported as acid-base pairs responsible for ethanol dehydrogenation and aldol condensation, respectively, by using *operando* DRIFTS measurement.[128] Although there are already various studies that point out the importance of the acid-base pair on HAP during ethanol coupling to *n*-butanol, the role of the specific sites on HAP during each step, including hydrogenation, is still unclear. Therefore, direct spectroscopic evidence from *operando* experiments is needed to elucidate the relationship between each step and surface site.

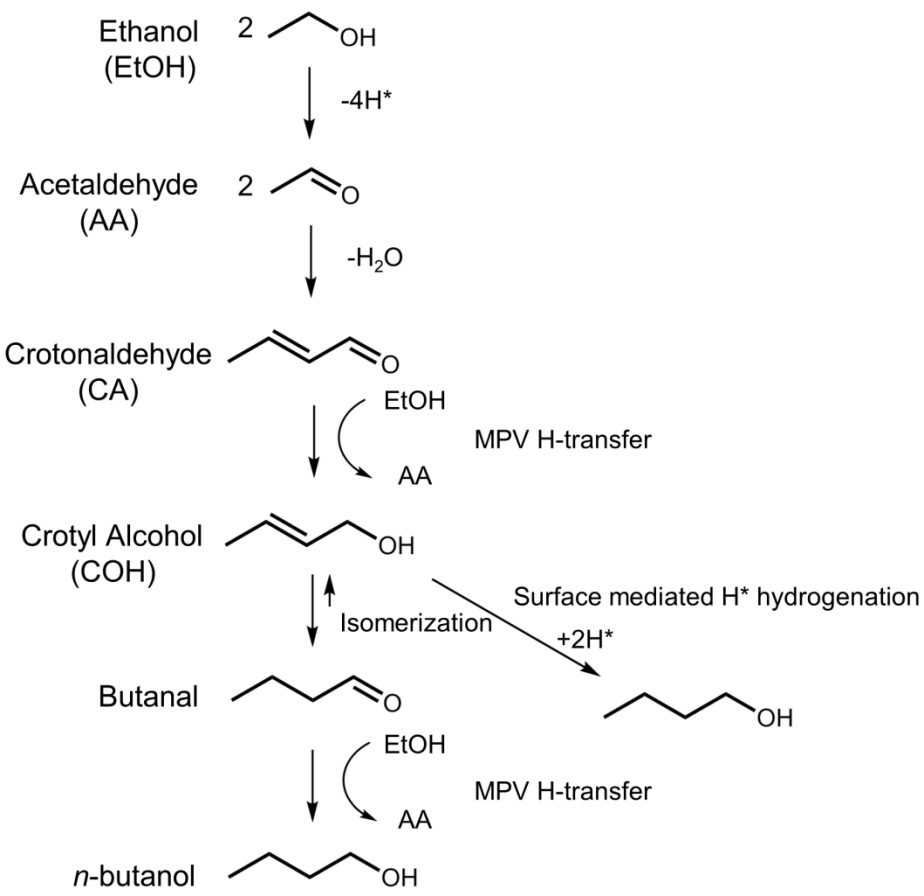

Scheme 2.1. Generally accepted pathways of ethanol coupling to n-butanol over hydroxyapatite (HAP), MPV stands for Meerwein-Ponndorf-Verley reaction.

Here, we investigate ethanol coupling to *n*-butanol over hydroxyapatite (HAP) using diffuse reflectance infrared Fourier transform spectroscopy coupled with mass spectrometry (DRIFTS-MS) to simultaneously monitor the surface species and the product distribution in the gas phase.[87, 129] In addition, we use modulation excitation (ME) to intensify the signal for active species and enhance the signal-to-noise ratio.[84-85] Moreover, by operating with phase-sensitive detection (PSD), the spectroscopic signatures of consecutive reaction intermediates can be revealed in the phase-domain, providing micro-kinetic information.[91] Our *operando* DRIFTS-MS with ME experiments show spectroscopic evidence to support the generally accepted reaction mechanism of

ethanol coupling over HAP *via* the Guerbet pathway. In addition, Ca^{2+}/OH^- pair sites are proposed as main active site for aldol condensation and POH/OH^- pair sites are proposed to be responsible for Meerwein-Ponndorf-Verley (MPV) direct hydrogen transfer for hydrogenation. Spectroscopic evidence for the isomerization of crotyl alcohol that we observed supports direct hydrogen transfer as the second hydrogenation step during ethanol coupling. Interactions between surface species and different reaction intermediates are discussed to guide further catalyst design for ethanol upgrading.

2.2 Results and Discussion

In this work we use modulation excitation (ME) with diffuse reflectance infrared Fourier Transform spectroscopy coupled with mass spectrometry (DRIFTS-MS). Modulation excitation spectroscopy works similarly to a lock-in amplifier which is used to enhance the signal-to-noise ratio and extract the desired signals from noisy condition.[91, 130-131] The same concept can also apply to a spectroscopic technique by periodically perturbing the system with one variable such as reactant concentration, temperature, pressure, or radiation.[84] When a catalytic system is perturbed under quasi steady-state conditions, reaction intermediates will oscillate with the same frequency. After averaging several periods, the signal from active species will be enhanced while the spectator species will not respond to the stimulation and can thus be easily distinguished. In addition, the signal-to-noise ratio will increase because of the averaging. Moreover, by operating with phase sensitive detection (PSD) to transform from time-domain to phase-domain, different active species will show distinct phase-delays compared to the starting reactant and these different phase shifts contain kinetic information.

The transmission IR spectrum of HAP from Sigma-Aldrich is shown in **Figure S2.1**. The peak at 3572 cm^{-1} corresponds to the columnar hydroxyl group (OH^-) on HAP. The

band at 3648 cm^{-1} is attributed to bulk POH group; 3674 and 3706 cm^{-1} correspond to surface POH site which coincide with previous report. The combination bands and overtone of P-O feature can also be observed at 2200-1900 cm^{-1}. The bands between 1550 and 1250 cm^{-1} are attributed to carbonate species.[124, 132-133] The wavenumbers from POH we discovered here are slightly higher than in the literature due to the higher dehydration temperature (600 ^{o}C) in this study. The X-ray diffraction pattern is presented in **Figure S2.2** which is identical to previous literature.[124]

Modulation experiments with ethanol

We first introduce the starting reactant, ethanol, to the system to understand the formation of reaction intermediates. Before starting the modulation experiment, HAP was treated under pure Ar flow and heated to 330 °C, followed by periodic switching between ethanol and pure Ar. The reaction downstream is monitored by mass spectrometry. The chosen m/z values correspond to unique mass fragments of each intermediate and product. We would also like to point out that some m/z signals are scaled for better reading (**Figure 2.1a**). When ethanol is introduced into the system, the signals from the reaction intermediates and product such as acetaldehyde (m/z = 44), crotyl alcohol (m/z = 57), and *n*-butanol (m/z = 56) can be observed. During ethanol coupling, 1,3-butadiene (m/z = 54) occurs as the side product obtained *via* the dehydration of crotyl alcohol by Lewis acid site on HAP.[127] Only trace amounts of butanal (m/z = 72) and crotonaldehyde (m/z = 70) are observed, implying that hydrogenation of the carbonyl group on both species occurs rapidly.

In the first half period of the experiment, the surface is covered by ethanol as indicated by the features at 3666, 2972, 2933 and 2903 cm^{-1} for υ(O-H), $\upsilon(CH_3$, asymmetric), $\upsilon(CH_2)$, and $\upsilon(CH_3$, symmetric), respectively (**Figure 2.1b**). This

observation corroborates the conclusion of a previous study that shows high ethanol coverage on HAP comparing to MgO at reaction temperature by using steady-state isotopic kinetic transient analysis (SSITKA).[122] Aside from the intense ethanol signals in the IR spectra, a small band at 1758 cm^{-1} indicates the formation of acetaldehyde, an intermediate in ethanol coupling following the Guerbet pathway. In contrast, a band at 1577 cm^{-1} corresponds to aromatic coke acting as spectator species that does not respond to the modulation, showing the capability of modulation excitation to discriminate active and spectator species. Moreover, to the best of our knowledge, acetaldehyde has not been directly observed before in ethanol coupling using *in-situ* spectroscopy. The intensity of columnar hydroxyl group (OH^-) at 3572 cm^{-1} on HAP[133-134] (**Figure S2.2**) decreases during the reaction (**Figure 2.1b**) suggesting an interaction of ethanol with the OH^-. The importance of the columnar hydroxyl group is supported by a previous kinetic study which shows that HAP ($Ca_{10}(PO_4)_6(OH)_2$) with OH^- is more selective to *n*-butanol than beta-tricalcium phosphate (β-$Ca_3(PO_4)_2$) and fluoride-substituted phosphate ($Ca_{10}(PO_4)_6F_2$),[135] since the OH^- group could be responsible for base-catalyzed aldol condensation.

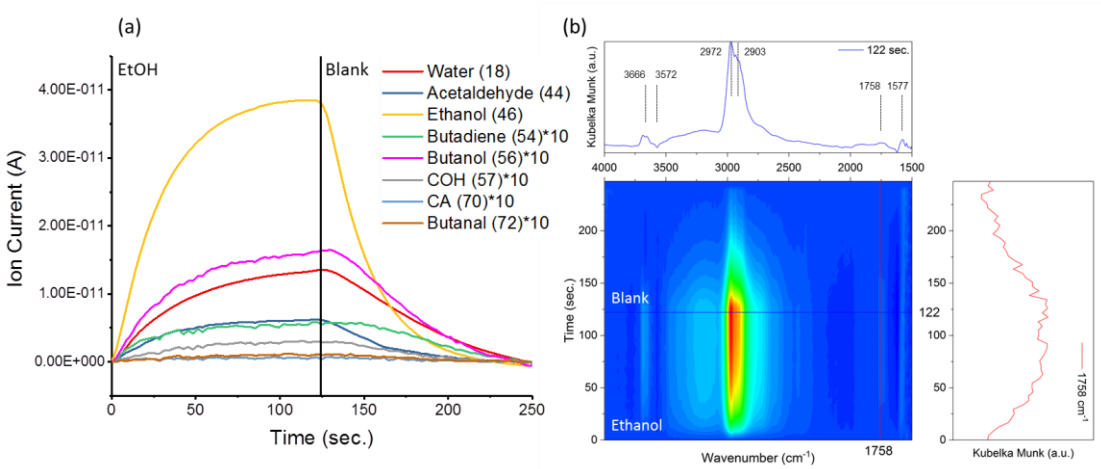

Figure 2.1. Modulation experiment between ethanol (5.0%) in Ar and pure Ar (20 mL min^{-1}) over 5 mg hydroxyapatite (HAP) at 330 ^{o}C, the total flow rate for both channel are 20 mL min^{-1} which Ar behaves as balance gas (a) selected m/z signals from mass spectrometry response (b) Time-domain DRIFT spectra and the line at 122 sec. indicates gas channels switch.

Modulation experiment with ethanol/acetaldehyde and ethanol

To investigate the aldol condensation reaction, we added acetaldehyde to the reagent stream while keeping the ethanol concentration constant at 2.5%. The HAP surface was first saturated with 2.5% ethanol in Ar and the background was taken before starting periodic modulation in which the first half period was ethanol/acetaldehyde with 3:1 molar ratio and ethanol was maintained at 2.5% in the feed. After averaging and operating phase sensitive detection (PSD) for five periods of MS responses and DRIFT spectra, the changing signals are attributed to the perturbation by acetaldehyde. The response MS signals show an enhancement for the aldol condensation product, crotonaldehyde (m/z = 70) (**Figure 2.2a**). The result is in line with previous observations that the rate of C-C bond formation increases linearly with co-fed acetaldehyde.[123] In addition to the increase of crotonaldehyde, other intermediates and side products including butanal (m/z = 72), crotyl alcohol (m/z = 57) and 1,3-butadiene (m/z = 54) are observed. The final product, *n*-butanol (m/z = 56), appears with 17 seconds time-delay in

the gas phase compared to acetaldehyde and other intermediates, suggesting that desorption of product may be slow over hydroxyapatite.

The time-domain infrared spectra show a negative peak at 2980 cm^{-1} indicating partial desorption and/or reaction of surface-bound ethanol. The other significant peaks in the C-H region at 2736, 3026, and 2960 cm^{-1} correspond to acetaldehyde, crotyl alcohol, and *n*-butanol, respectively, showing a sequential time-delay in each species, which is in line with the proposed Guerbet pathway (**Figure 2.2b**). Notably, the co-fed acetaldehyde (2736 cm^{-1}) can be first seen at 8 sec. and the consecutive intermediate crotyl alcohol (3026 cm^{-1}) appears at 25 sec. suggesting aldol condensation and direct hydrogen transfer from ethanol *via* Meerwein-Ponndorf-Verley (MPV) pathway proceed rapidly. The strong signal at 1761-1720 cm^{-1} is due to υ(C=O) from gas phase acetaldehyde. The emergence of a feature at 1645 cm^{-1} corresponding to υ(C=C) from the aldol product, crotonaldehyde, shows a time-delay compared to υ(C=O) from acetaldehyde. The features from the other intermediate butanal are barely observed in the IR spectrum, which could be attributed to the fast desorption and/or reaction, or they are hindered by peaks from acetaldehyde, as there is a notable amount of crotonaldehyde (m/z = 70) and butanal (m/z = 72) in the MS response (**Figure 2.2a**). The decreasing signal of columnar hydroxyl group at 3572 cm^{-1} indicates that the OH^- group may behave as basic site to abstract α-hydrogen on acetaldehyde to form the enolate for aldol condensation.

By using phase-sensitive detection (PSD), phase-domain IR spectra show three distinct species in the C-H region: acetaldehyde with a phase delay of 10^o (or 7 s) at 2736 cm^{-1}, crotyl alcohol with a phase delay of 40^o (or 28 s) at 3026 cm^{-1}, and *n*-butanol with a phase delay of 70^o (or 49 s) at 2960 cm^{-1} (**Figure 2.3**). We emphasize that the inherent dead volume of the DRIFTS cell increases the apparent phase delay by ~10^o

and that phase delays of various species should therefore only be used relative to one another. The observed consecutive reaction intermediates and product agree with the generally accepted hypothesis that ethanol coupling to *n*-butanol on HAP at 330 ^{o}C proceeds *via* the Guerbet pathway.

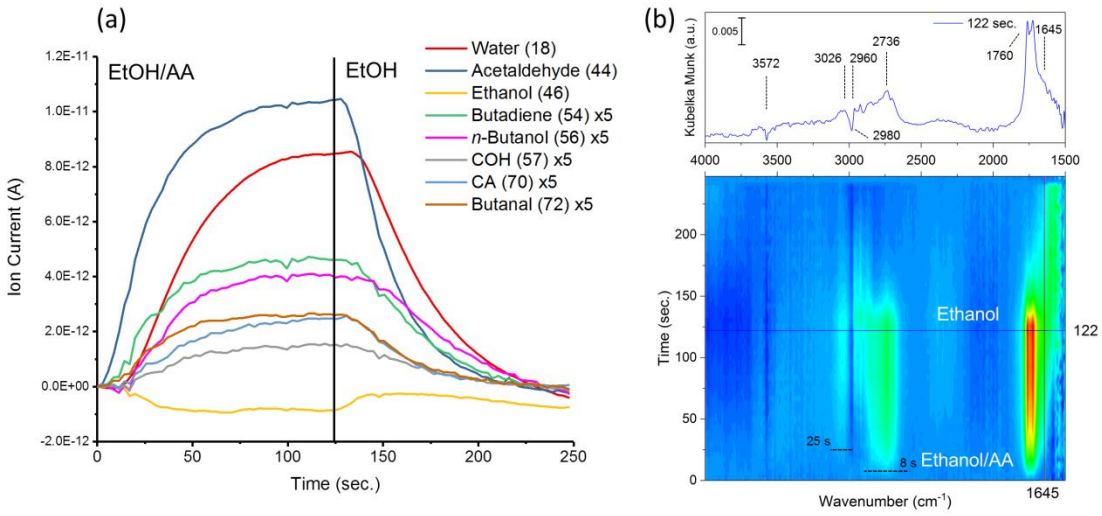

Figure 2.2. Modulation experiment between ethanol (2.5%)/AA with 3:1 molar mixture in Ar as carrier gas and ethanol in Ar over 5 mg hydroxyapatite (HAP) at 330 ^{o}C, the total flow rate for both channel are 20 mL min^{-1} which Ar behaves as balance gas. (a) selected m/z signals from mass spectrometry response (b) Time-domain DRIFT spectra and the line at 122 sec. indicates gas channels switch.

Modulation experiment with ethanol/crotonaldehyde and ethanol

To study the role of crotonaldehyde and hydrogenation products such as crotyl alcohol, butanal, and *n*-butanol, we co-fed crotonaldehyde with ethanol as described previously for acetaldehyde. In the experiment shown in **Figure 2.4a**, HAP was first equilibrated in ethanol feed, followed by periodically switching to a 3:1 molar ratio ethanol/crotonaldehyde flow. In the gas phase, acetaldehyde (m/z = 44) increases dramatically when crotonaldehyde is co-fed. Crotyl alcohol (m/z = 57), butanal (m/z = 72) and *n*-butanol (m/z = 56) are enhanced as well. The increased production of

acetaldehyde in the beginning of first half period indicates that direct hydrogen transfer from ethanol to crotonaldehyde occurs rapidly. An undesired side product, 1,3-butadiene (m/z = 54) also increases with co-fed crotonaldehyde, suggesting dehydration of crotyl alcohol may compete with the further hydrogenation step. Moreover, *n*-butanol (m/z = 56) and water (m/z = 18) appear with 11 seconds time-delay in the MS response, implying slow desorption from the HAP surface.

A similar result can also be seen in the time-domain IR spectra, (**Figure 2.4b**) where υ(C=O) from acetaldehyde emerges as a side band at 1758 cm^{-1} at the beginning, along with the υ(C-H) for crotyl alcohol at 3026 cm^{-1} with co-fed crotonaldehyde, indicating MPV hydrogen transfer is fast. More importantly, the *n*-butanol signal at 2960 cm^{-1} persists into the second half period when crotonaldehyde is removed from the feed, which is in line with MS response that the desorption rate of *n*-butanol is slow. In the phase-domain IR spectra, the co-fed crotonaldehyde can be observed at 2730 and 2815 cm^{-1} with 10^{o} (7 s) phase delay, while crotyl alcohol appears at 3026 cm^{-1} with 40^{o} (28 s) phase delay. The final product, *n*-butanol, can be seen at 2960 cm^{-1} with 70^{o} (49 s) phase delay (**Figure S2.7**).

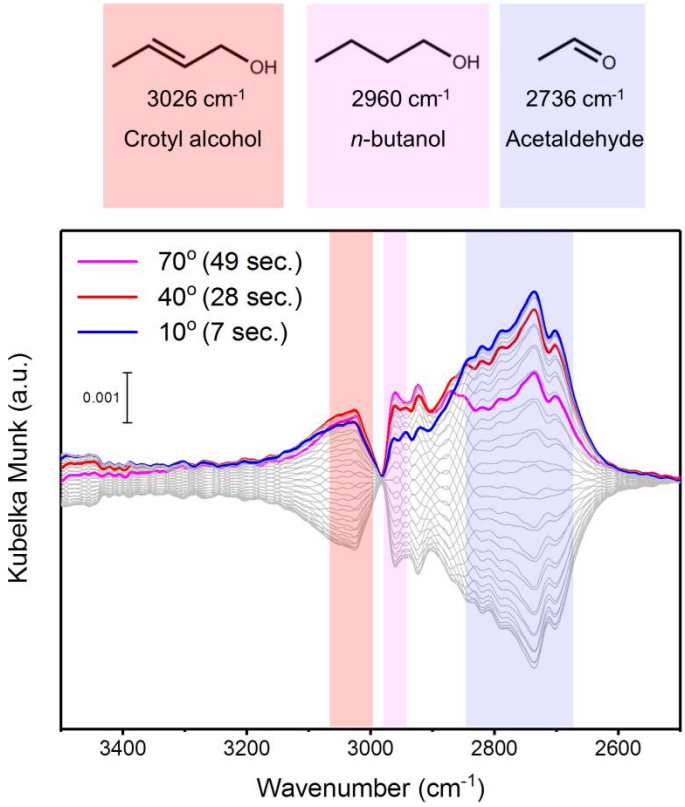

Figure 2.3. Phase-sensitive detection (PSD) DRIFT spectra in C-H region with modulation experiment between ethanol (2.5%)/AA with 3:1 molar mixture in Ar as carrier gas and ethanol in Ar flow, the total flow rate for both channel are 20 mL min^{-1} which Ar behaves as balance gas. The phase-delay at 10^{o} corresponds to acetaldehyde, 40^{o} correlates to crotyl alcohol, and 70^{o} indicates *n*-butanol. A full period (250 s) is identical to 360^{o}.

This result mirrors the behavior we observed earlier when modulating between ethanol/acetaldehyde and ethanol. The phase-domain IR spectra demonstrate that the aldol condensation product subsequently undergoes hydrogenation to form *n*-butanol. Although several studies show that the C=O on crotonaldehyde will be hydrogenated by MPV direct hydrogen transfer from ethanol to form crotyl alcohol, the mechanism of the second hydrogenation step is still not well understood. Indeed, the hydrogenation can occur either to the C=C bond of crotyl alcohol through a surface-mediated pathway[123] or it can occur at the C=O bond of butanal, which is isomerized from crotyl alcohol, through the MPV direct hydrogen transfer from ethanol to obtain *n*-butanol[124-125] (**Scheme 2.1**). In

a subsequent ME experiment, we perturbed the system with crotyl alcohol and butanal in order to obtain insights into this second hydrogenation step.

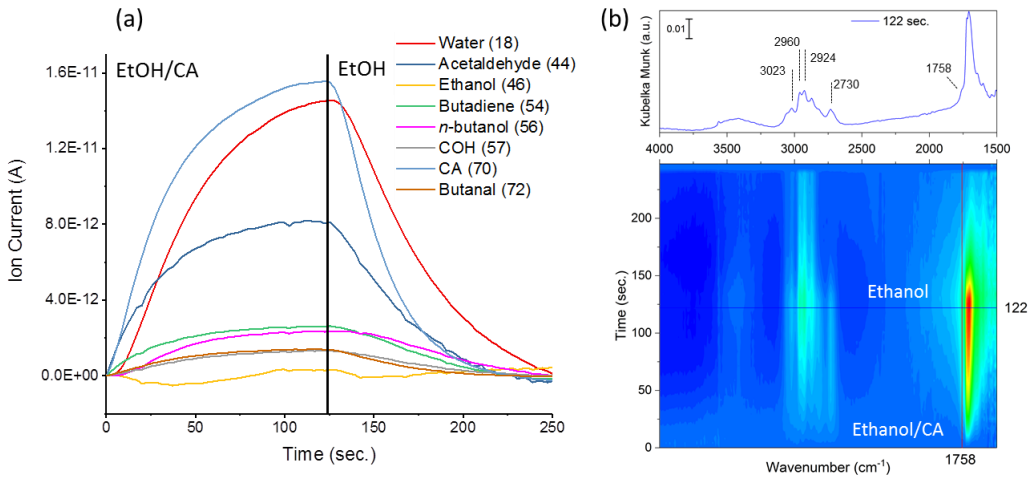

Figure 2.4. Modulation experiment between ethanol (2.5%)/CA with 3:1 molar mixture in Ar as carrier gas and ethanol in Ar over 5 mg hydroxyapatite (HAP) at 330 ^{o}C, the total flow rate for both channel are 20 mL min^{-1} which Ar behaves as balance gas. (a) selected m/z signals from mass spectrometry response (b) Time-domain DRIFT spectra and the line at 122 sec. indicates gas channels switch.

Modulation experiment with ethanol/crotyl alcohol and ethanol

When crotyl alcohol is co-fed into the system during ethanol coupling, the dehydration side products, 1,3-butadiene (m/z = 54) and water (m/z = 18), increase directly in MS response. On the other hand, the desired product, *n*-butanol (m/z = 56), increases slightly compared to 1,3-butadiene when co-feeding crotyl alcohol (m/z = 57) into the system (**Figure S2.8a**). The enhancement of 1,3-butadiene could be due to the moderate Lewis acidic site on HAP[126-127] which favors the dehydration pathway under crotyl alcohol co-feed condition. Interestingly, while 1,3-butadiene seems to increase with crotyl alcohol addition, the final product, *n*-butanol, does not increase substantially. This difference in response suggests that, *n*-butanol could predominately come from MPV

direct hydrogenation of C=O on butanal, obtained from crotyl alcohol isomerization; hydrogenation on C=C of crotyl alcohol through surface mediated hydrogen seems unlikely.

In the time-domain IR spectra (**Figure S2.8b**), crotyl alcohol becomes the dominant surface species on HAP with several significant features at 3026, 2923, 2879, 1676 cm^{-1}, in-line with the MS response that the increased ethanol in the first half period is due to competitive adsorption with crotyl alcohol (*viz,* ethanol desorbs from HAP surface because of the addition of crotyl alcohol). The competitive adsorption can explain the inhibition of direct hydrogen transfer due to a lower abundance of ethanol on the HAP surface, therefore enhancing the dehydration on Lewis acidic sites. The evidence for 1,3-butadiene from dehydration of crotyl alcohol can also be observed at 1802 and 1817 cm^{-1}. As a result, ethanol coupling over HAP at high crotyl alcohol concentration tends to undergo the dehydration pathway due to Lewis acidity on HAP[135] and competitive adsorption with ethanol.

Modulation experiment with ethanol/butanal and ethanol

When co-feeding butanal during ethanol coupling over HAP, the MS responses show that *n*-butanol (m/z = 56) increases dramatically as a main product and the ethanol (m/z = 46) signal decreases in the first half period, indicating that direct hydrogen transfer from ethanol to butanal occurs rapidly (**Figure 2.5a**). The result implies that *n*-butanol stems from butanal as the last reactive intermediate by direct hydrogen transfer. The sacrificial ethanol will then dehydrogenate to acetaldehyde and subsequently undergo self-aldol condensation to crotonaldehyde which can be further hydrogenated by direct hydrogen transfer to finish the autocatalytic cycle. This finding supports a previous study which stated that acetaldehyde is generated mainly from direct hydrogen transfer and

ethanol is mainly a hydrogen source for direct hydrogen transfer.[125] Furthermore, there is no significant increase in crotonaldehyde (m/z = 70), rendering further support for the fast hydrogenation of C=O to crotyl alcohol (m/z = 57) which we can clearly observe in MS response.

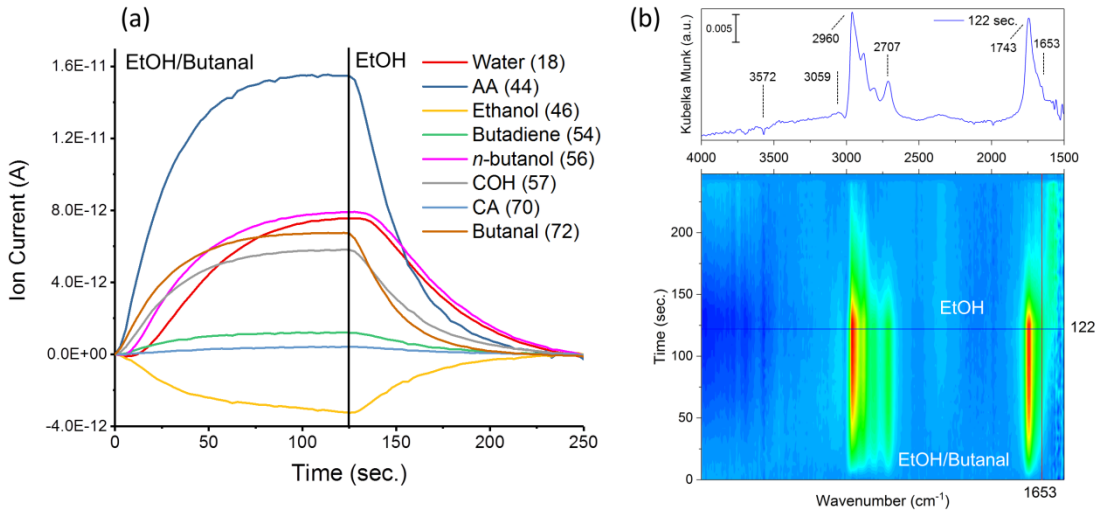

Figure 2.5. Modulation experiment between ethanol (2.5%)/butanal with 3:1 molar mixture in Ar as carrier gas and ethanol in Ar over 5 mg hydroxyapatite (HAP) at 330 ^{o}C, the total flow rate for both channel are 20 mL min^{-1} which Ar behaves as balance gas. (a) selected m/z signals from mass spectrometry response (b) Time-domain DRIFT spectra and the line at 122 sec. indicates gas channels switch.

In the time-domain IR spectra, the peaks at 2960 cm^{-1} correspond to υ(C-H) from *n*-butanol which remains on the surface into the second half period compared to butanal at 2707 and 1743 cm^{-1} (υ(C-H) and υ(C=O), respectively) (**Figure 2.5b**). The slow desorption of *n*-butanol can also be observed in the MS response, where *n*-butanol (m/z = 56) shows a time-delay of 6 seconds relative to the introduction of butanal. Although there is only a trace amount of crotonaldehyde observed in MS response, the evidence of υ(C=C) in crotonaldehyde surface species from self-aldol condensation of acetaldehyde coming from direct hydrogen transfer can also be found at 1653 cm^{-1}.

Interestingly, a peak appears at 3059 cm^{-1} during the butanal co-feed experiment with a 25 seconds time-delay compared to the signal from butanal. This vibrational feature is too high with a frequency for υ(=C-H) in crotyl alcohol, but similar to the terminal alkene $\upsilon(=CH_2)$ signal in 1-butene.[136] Thus, the emergence of the peak at 3059 cm^{-1} could correspond to 3-buten-1-ol having terminal alkene feature from crotyl alcohol isomerization (**Scheme 2.2**). Indeed, the dehydration of 3-buten-1-ol is the side product, 1,3-butadiene, which we also observed in the ethanol to *n*-butanol reaction. The formation of 3-buten-1-ol shows that isomerization can occur on the HAP surface. However, the other isomer, 1-buten-1-ol, cannot be found in the IR spectra. The possible reason is that the less stable isomer, 1-buten-1-ol, will most likely undergo fast tautomerization to butanal. In other words, the rate of tautormerization of 1-buten-1-ol is a fast step compared to the dehydration of 3-buten-1-ol which can explain the absent of spectroscopic evidence for 1-buten-1-ol. Although it has been suggested that the isomerization can occur on basic sites or Ca-O sites on HAP surface,[124] there has been no spectroscopic support for the hypothesis. Here, we first provide an evidence for the isomerization on HAP surface with the IR peak at 3059 cm^{-1} for a terminal alkene $\upsilon(=CH_2)$ which is attributed to 3-buten-1-ol, an isomer from crotyl alcohol. Furthermore, because of the poor dehydrogenation ability of HAP,[125] the main source of acetaldehyde may come from direct hydrogen transfer (**Scheme 2.1**); thus, the second hydrogenation most likely proceeds *via* the MPV direct hydrogenation pathway. Besides dehydrogenation of ethanol to obtain the very first acetaldehyde to proceed the reaction, the trace amount of dissolved O_2 in ethanol may also cause oxidation of ethanol to acetaldehyde, since there are barely redox properties on HAP compared to transition metal catalysts.

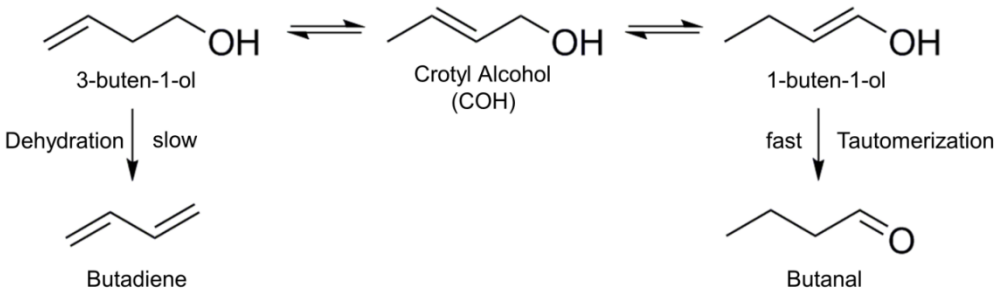

Scheme 2.2. Isomerization pathway for crotyl alcohol to butanal and dehydration to 1,3-butadiene.

Modulation experiment with crotonaldehyde and ethanol

To better understand the hydrogenation process, we first saturated the HAP surface and reached steady state in an ethanol feed and subsequently switched to crotonaldehyde feed without ethanol. Before switching to the crotonaldehyde flow, ethanol is the predominant surface species on HAP. After switching to crotonaldehyde flow, acetaldehyde and C_4 intermediates such as crotyl alcohol and butanal increase immediately as well as *n*-butanol, indicating that direct hydrogen transfer from ethanol occurs rapidly (**Figure 2.6a**). More importantly, once the adsorbed ethanol on HAP surface is fully consumed by direct hydrogen transfer, the reaction stops at crotyl alcohol and butanal. The final hydrogenation products, *n*-butanol and acetaldehyde stop producing at 30 seconds after switching to the crotonaldehyde feed. Crotyl alcohol formation also reaches its maximum around 40 seconds because of a lack of surface ethanol to hydrogenate crotonaldehyde. It is worth noting that after consuming surface ethanol species, butanal increases slightly until the end of the first half period, while crotyl alcohol slightly decreases at the same time. This finding also indicates that isomerization from crotyl alcohol to butanal takes place on HAP surface.

In the time-domain IR spectra, the negative peaks at 2977 and 2903 cm^{-1} correspond to surface ethanol consumption which corroborates the finding that ethanol

mostly behaves as a hydrogen donor (**Figure 2.6b**). The features from crotonaldehyde at 2815, 2730, 1720, 1697, 1643 cm^{-1} gradually dominate the HAP surface, indicating the reaction stops without adding ethanol. While the bands at 1720 and 1643 cm^{-1} correspond to υ(C=O) and υ(C=C), respectively, from gas phase crotonaldehyde, the emergence of 1697 cm^{-1} could be adsorption of carbonyl group on acid site such as Ca^{2+} or POH. Notably, a band emerges at 3059 cm^{-1} which is similar to the feature in butanal co-feed IR spectra above (**Figure 2.5b**), suggesting a terminal alkene-like species which could form from crotyl alcohol isomerization. This inference is supported by the MS responses, as butanal increases while crotyl alcohol decreases once the sacrificial ethanol is consumed. The decreased peaks at 3572 and 3674 cm^{-1} correspond to OH^- and POH on HAP which are likely responsible for direct hydrogen transfer and isomerization. The same decreasing IR peaks for OH^- and POH can also be found in the butanal co-feed experiment (**Figure 2.5b**).

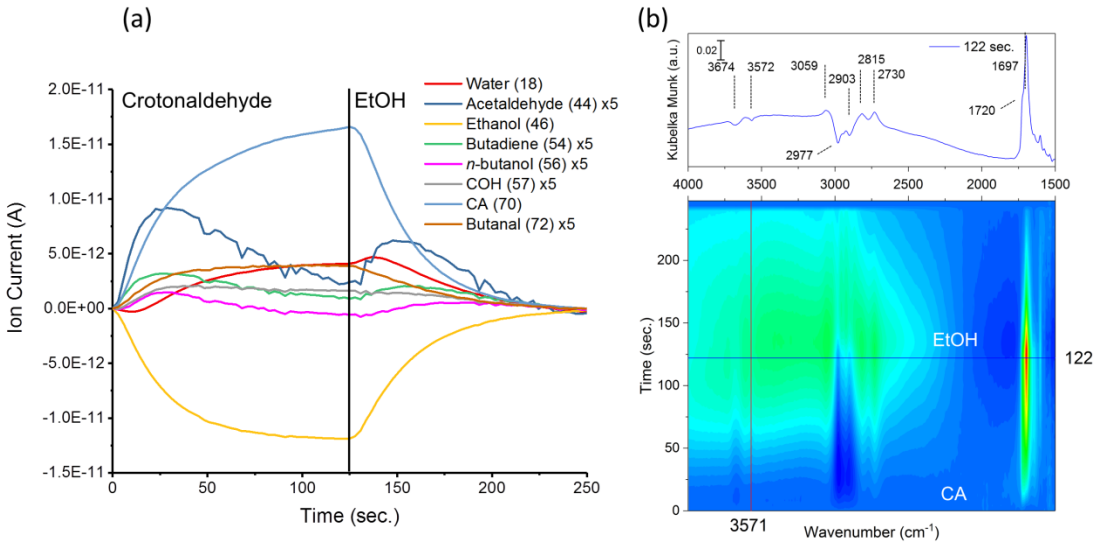

Figure 2.6. Modulation experiment between CA (0.8%) and ethanol (2.5%) in Ar as carrier gas over 5 mg hydroxyapatite (HAP) at 330 ^oC, the total flow rate for both channel are 20 mL min^{-1} which Ar behaves as balance gas. (a) selected m/z signals from mass spectrometry response (b) Time-domain DRIFT spectra and the line at 122 sec. indicates gas channels switch.

The possible acid and base sites on HAP have been characterized by using pyridine, CO_2, acetylene, and glycine as probe molecules.[126-127] The proposed acid sites are Ca^{2+} and protonated phosphate groups, POH, while the columnar OH^- group is the most significant basic site on the HAP surface. Therefore, Ca^{2+}/OH^- and POH/OH^- acid-base pairs are potential active sites for ethanol coupling over HAP surface. The significant decreased IR band at 3572 cm^{-1} corresponding to OH^- group on HAP surface in acetaldehyde co-feed experiment, indicates that OH^- is one of the active sites for base-catalyzed aldol condensation (**Figure 2.2b**). The importance of OH^- for C-C coupling is further supported by the increased selectivity towards *n*-butanol for HAP compared to calcium phosphate ($Ca_3(PO_4)_2$) without OH^- group.[135] Since we do not observe a significant signal corresponding to the POH group in acetaldehyde co-feed IR spectra, Ca^{2+}/OH^- may likely act as acid-base pair for aldol condensation over HAP. When co-feeding butanal and modulating between crotonaldehyde and ethanol, (**Figure 2.5b** and **Figure 2.6b**) there is a decrease in the POH/OH^- acid-base pair signal. This suggests that POH/OH^- is the active site for Meerwein-Ponndorf-Verley (MPV) direct hydrogen transfer. (**Scheme 2.3**) The findings corroborate the work by Osman *et al*. where they found no production of *n*-butanol if the POH site has been poisoned.[128]

The isomerization of crotyl alcohol to 1-butene-1-ol can occur on both acid and base site, since Bronsted acid site such as POH can protonate to C=C and subsequently, the adjacent carbon releases a proton to form a new C=C bond to finish isomerization.[136] The basic OH^- site can also isomerize crotyl alcohol to form 1-butene-1-ol which is a facile reaction over metal oxide catalysts like MgO and CaO.[124, 137] In the experiment where we feed crotonaldehyde over an ethanol-saturated system, a decreased IR peak of POH at 3674 cm^{-1} may indicate deprotonation of POH group and a decrease peak at 3572 cm^{-1} suggests the abstraction of hydrogen by the OH^- group to eliminate the

columnar hydroxyl group signal (**Figure 2.6b**). Therefore, both POH and OH^- sites are possible to catalyze crotyl alcohol isomerization and the isomer, 1-butene-1-ol, will subsequently tautomerize to butanal and be hydrogenated *via* direct hydrogen transfer to *n*-butanol.

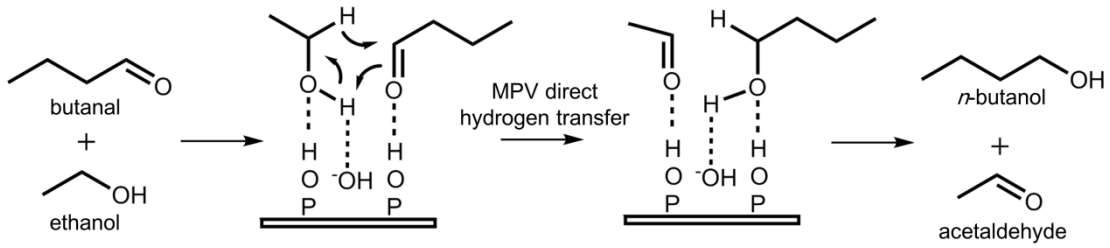

Scheme 2.3. Meerwin-Ponndorf-Verley (MPV) direct hydrogen transfer on POH/OH^- acid-base pair.

2.3 Conclusion

In this study, the mechanism for ethanol coupling to *n*-butanol over HAP is investigated using *operando* DRIFTS-MS with modulation excitation (ME) and phase sensitive detection (PSD). The enhanced signal-to-noise ratio allows us to observe the IR features from intermediates and help to elucidate the mechanism. MS results and the phase-domain spectra show the consecutive formation of reaction intermediates, supporting the Guerbet pathway as the overall mechanism for ethanol coupling over HAP. The phase-domain IR spectra from acetaldehyde co-feed experiments demonstrate consecutive reaction intermediates during ethanol coupling. The first hydrogenation step in which crotonaldehyde converts to crotyl alcohol is attributed to direct hydrogen transfer from ethanol by the result of crotonaldehyde co-feed experiment. From the result of modulating between crotonaldehyde and ethanol experiment, the emergence of the peak at 3059 cm^{-1} corresponds to terminal-like alkene $\upsilon(=CH_2)$ indicating the appearance of 3-butene-1-ol, the isomer of crotyl alcohol. This finding implies that crotyl alcohol

undergoes isomerization and tautomerization to butanal over the HAP surface and the second hydrogenation subsequently occurs on butanal by direct hydrogen transfer to produce *n*-butanol.

We also show that the Ca^{2+}/OH^- acid-base pair is mainly responsible for aldol condensation based on acetaldehyde co-feed experiment. In addition, direct hydrogen transfer occurs on POH/OH^- acid-base pair, since hydrogen donor, ethanol, can be stabilized on HAP surface on both sites based on ethanol adsorption IR spectrum and *operando* DRIFT spectra. Finally, the active site for isomerization can be either POH or OH^-, because both sites show interaction in modulation DRIFT spectra between crotonaldehyde and ethanol. The competitive adsorption between ethanol and crotyl alcohol suggests that isomerization may be critical for the overall performance, since direct hydrogen transfer occurs rapidly. This puts forward the hypothesis that eliminating the Lewis acid site could avoid the undesired dehydration side-reaction, while increasing the POH and OH^- site density could enhance the isomerization.

2.4 Experimental Details

Hydroxyapatite ($Ca_{10}(PO_4)_6(OH)_2$, HAP) was purchased from Sigma-Aldrich and was calcined at 600 ^oC with 5 ^oC/min ramp rate for 2 hours under dry air before operating ethanol coupling reaction. Ethanol was dehydrated by molecule sieves (3 Å) before using to eliminate the interference in IR spectra.

The modulation excitation DRIFTS-MS setup allows for the introduction and vaporization of liquid substrates, and switching between two different flows, effectively modulating the concentration of reactants during experiment. In short, argon was used as carrier gas and connected to two different mass flow controllers to generate two independent feed. Besides of Ar as carrier gas, Ar is also a balance gas to maintain total

flow rate at 20 mL min^{-1}.Two syringe pumps were used to introduce liquids that are evaporated in a heated spiral before reaching an electronically controlled two-position-four-way valve. Depending on the position of this valve, either flow A or B enters into the DRIFTS accessory. The catalyst, HAP, is filled in ta ceramic cup in DRIFTS cell with approx. 5 mg. Finally, the gas-phase composition is monitored with an online mass spectrometer. By periodically switching between flow A and B, the influence of either component on the reaction can be analyzed in a transient manner. A single period of the complete modulation is 250 seconds in this study, unless further mentioned. The detail for MES-DRIFTS-MS setup can be found in previous study.[87, 129]

All IR measurements are collected by a Bruker Vertex 70 spectrometer with mercury cadmium telluride (MCT) detector. Each spectrum is obtained from 64 scans with 8 cm^{-1} resolution and 4 seconds as temporal resolution in modulation experiment. The DRIFTS accessory was purchased from PIKE Technologies (DiffusIR) and approximately 5 mg HAP can be loaded in the ceramic crucible. The m/z responses are obtained from ThermoStar mass spectrometer, Pfeiffer Vacuum, attached on the outlet of DRIFTS accessory. The phase sensitive detection (PSD) transforms the DRIFT spectra from time-domain to phase domain by using the equations as follow:

$$A_k\left(\varphi_k^{PSD}\right) = \frac{2}{T}\int_0^T A(t)\sin\left(k\omega t + \varphi_k^{PSD}\right)dt \qquad (2.1)$$

Where T is the length of a period, ω is the stimulation frequency, ϕ_k is the phase delay, k is the demodulation index (k = 1 in the study), A(t) is the active species response in the time-domain, and A_k is the response in the phase-domain. The transformation to the phase-domain leads to a dependence of the vibrational signals on the phase angle ϕ instead of the time. For example, 250 sec period can be converted to 360^o. The analysis of the spectra was processed using MATLAB codes.

Chapter 3: Quantification of Exchanged Copper Species in Cu-Chabazite Zeolite Using Cryogenic Probe Infrared Spectroscopy

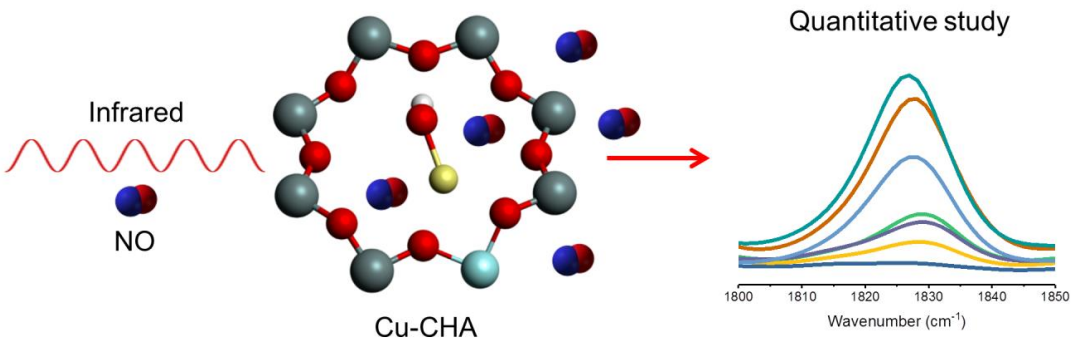

This chapter was collaborated with BASF to develop a facile methodology for identifying and quantifying the exchanged copper species in Cu-CHA. We successfully established a low temperature NO-IR technique to not only applicable to powder Cu-CHA samples, but also industrially relevant honeycomb Cu-CHA samples. This work was submitted for publication.

3.1 Introduction

NO_x (NO, NO_2) emissions from lean-burning and diesel engines are known to cause health problems, as well as acid rain.[138-139] Current vehicle technologies use selective catalytic reduction (SCR) with ammonia or urea to decompose NO_x into N_2 and water.[140-141]

Small pore copper ion-exchanged chabazite zeolites (Cu-CHA) have been industrially implemented because of their reliable activity in the removal of nitric oxide (NO) *via* ammonia selective catalytic reduction (NH_3-SCR).[142-143] The generally accepted active sites are Cu ions (both Cu^{2+}, Cu^{+}) located at the exchange sites in the CHA framework (created upon substitution of Al^{3+} for Si^{4+} in the SiO_2 matrix), as opposed to extra framework CuO_x species.[144-150] To understand the structure-reactivity relations and

to further characterize the nature of copper speciation, several spectroscopic techniques have been utilized such as X-ray absorption spectroscopy (XAS),[146, 151-153] X-ray emission spectroscopy (XES),[146, 151] UV-vis spectroscopy,[154-155] diffuse reflectance Infrared spectroscopy (DRIFTS),[156-157] Raman spectroscopy,[155, 158] and electron paramagnetic resonance (EPR).[159-160] Two Cu species have been proposed to exist after oxidative pretreatment: $Z_2Cu(II)$ and $Z_1Cu(II)OH$ (**Scheme 3.1**).[161] Due to varying Al^{3+} distributions in the zeolite framework, paired and isolated Al can both occur in the double six ring (d6r) of CHA (see **Scheme 3.1**). $Z_2Cu(II)$ can be found at d6r of CHA with paired Al configuration, while $Z_1Cu(II)OH$ is formed in d6r and 8-rings (8r) with isolated Al species. In addition to the Al distribution, the silica-to-alumina ratio (SAR) and Cu-loading in the CHA framework also affect the population of $Z_2Cu(II)$ and $Z_1Cu(II)OH$. The Al distribution in CHA is controlled by different Si/Al ratio and synthesis procedures, it has been observed that CHA with low SAR can have more paired Al sites than isolated Al sites. In contrast, CHA with high SAR showed mainly isolated Al sites.[162] For example, Cu-CHA with a SAR = 35 was observed to have a majority of isolated Al-configuration in the zeolite rings, resulting in a lower concentration of $Z_2Cu(II)$ as compared to Cu-CHA with SAR = 6. More importantly – based on previous experimental and computational results – $Z_2Cu(II)$ has been found to be more energetically favorable than $Z_1Cu(II)OH$, implying that the formation of $Z_2Cu(II)$ will occur first when increasing the Cu-loading.[152]

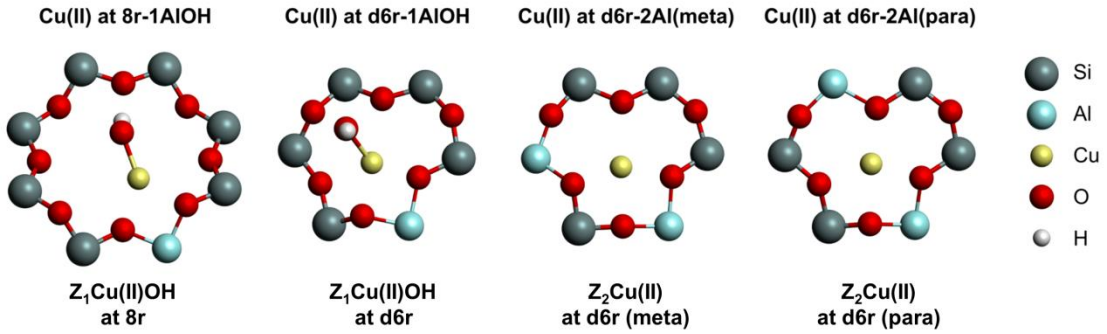

Scheme 3.1. Possible Cu species ($Z_1Cu(II)OH$, $Z_2Cu(II)$) in Cu-CHA with different Al distribution.

Although the possible Cu species in Cu-CHA have been identified, connecting their structure with deNO_x reactivity remains elusive because it requires precise determination of the amount of exchanged Cu in CHA. While inductively coupled plasma optical emission spectroscopy (ICP-OES) can determine the bulk Cu amount in CHA, it cannot distinguish between exchanged Cu species in the CHA framework and the surface CuO_x species that is out of the framework. The ability to differentiate between exchanged and non-exchanged Cu is especially important for industrially relevant high Cu-loading samples because of abundant non-exchanged CuO_x.[163-164] In fact, multiple steps of exchange procedure were used to minimize the formation of non-exchanged CuO_x. In contrast, one-step ion exchange is more common in industry, resulting in the formation of CuO_x. Therefore, a convenient method for identifying and quantifying Cu^+ and Cu^{2+} in Cu-CHA is needed. Recently, NO + NH_3 temperature programmed reaction (NO + NH_3 TPR) has been applied to quantify reducible exchanged Cu in CHA by measuring the consumption of NO and production of N_2.[165] Similarly, hydrogen temperature programmed reduction (H_2-TPR) has also been performed to assess the ratio of $Z_2Cu(II)$ and $Z_1Cu(II)OH$, which have different reduction temperatures.[156, 166-167] However, the TPR methods cannot provide a comprehensive analysis of the Cu speciation in Cu-CHA because it only shows $Z_2Cu(II)$ and $Z_1Cu(II)OH$ species. Other Cu species, such as Cu dimers, have also been suggested to exist.[154, 158, 168-173] Thus, a methodology that would quantify all Cu species would be beneficial for the derivation of structure-deNO_x reactivity relationship.

In-situ IR spectroscopy, with an appropriate probe molecule, is a widely applied approach to investigate the nature of a catalyst's active sites. Nitric oxide (NO) is reported to serve as a useful probe molecule for discerning the oxidation state of Cu cations in zeolites.[45, 78, 174] The formation of Cu^+-NO and Cu^{2+}-NO mononitrosyl species

show distinct peaks in an FT-IR spectrum (*i.e.* at 1826 and 1887-1970 cm^{-1}, respectively), allowing discrimination between the +1 and +2 oxidation states of the copper cations. However, the challenge of the NO-IR method is that already at ambient conditions, NO will disproportionate or reduce to N_2O by Cu ion in Cu-CHA.[79] The reaction of NO prevents proper quantification and interferes with the Cu^{+}-NO and Cu^{2+}-NO signals. Hence, low temperatures (-160 ^{o}C) are necessary to suppress this undesirable side reaction.[78] With low temperature NO-IR detection, the quantities and types of different Cu species can be identified across various Cu-loadings in Cu-CHA. When a reactive and desired Cu-exchanged CHA zeolite is discovered, the NO adsorption FT-IR method could be used to quickly assess the copper species distribution in the CHA framework and, thus, enhance the development of future catalysts through the correlation of copper speciation with catalytic activity. This methodology will also quantify the exchanged copper species, excluding non-exchanged copper species. In addition, the results from an NO-IR fingerprint study on Cu-exchanged CHA zeolites can be extended to other transition metal-exchanged zeolite catalysts as demonstrated herein.

3.2 Results and Discussion

Exchanged Cu ion signals from T-O-T framework vibrational IR spectra

Both paired Al and isolated Al can occur in the d6r in CHA. Under oxidative pretreatment conditions, the Cu ion located at a paired Al site is denoted as $Z_2Cu(II)$ and Cu ion at an isolated Al site is denoted as $Z_1Cu(II)OH$ **(Scheme 3.1)**. Based on the literature, FT-IR spectroscopy can differentiate between these two Cu species. The $Z_2Cu(II)$ species exhibits a feature at 900 cm^{-1}, which is associated with a perturbed T-O-T zeolite framework vibration, and $Z_1Cu(II)OH$ shows other perturbed T-O-T IR feature at 945 cm^{-1}.[156, 175] According to Di Iorio *et al.*, the Al distribution in CHA can be modified by

the ratio of the structure directing agent, *viz.* trimethyladamantylammonium hydroxide (TMAdaOH), to Na^+ during the CHA synthesis.[176] Thus, in order to assess the nature of the Cu-CHA perturbed T-O-T framework vibration, two parent CHA zeolites of different Al-configurations with a similar SAR were analyzed to differentiate between $Z_2Cu(II)$ and $Z_1Cu(II)OH$. CHA(20) (SAR = 20) features mainly paired Al sites, whereas CHA(23) (SAR = 23) consists mainly of isolated Al configurations. Cu-CHA with different Cu-loadings were synthesized by aqueous phase ion exchange[143] and the amount of Cu-loading was measured by ICP-OES. To mimic the typical oxidative condition used in activation of Cu-CHA,[151] Cu-CHA samples were treated under dry air at 400 ^oC for 30 minutes prior to collecting the IR spectra. In the two sets of Cu-CHA samples, the $Z_2Cu(II)$ perturbed T-O-T vibration was observed at 892 cm^{-1}, but the signal of $Z_1Cu(II)OH$ perturbed T-O-T framework at 945 cm^{-1} overlaps with strong Si-O stretching modes **(Figure 3.1)**. The $Z_2Cu(II)$ signal at 892 cm^{-1} was slightly lower in wavenumber than previously reported (900 cm^{-1}),[156] likely due to the difference in the operating temperature (400 ^oC *vs.* room temperature). In line with the high abundance of paired Al sites, the IR feature at 892 cm^{-1} – attributed to $Z_2Cu(II)$ – is more pronounced in Cu-CHA(20) than in Cu-CHA(23).

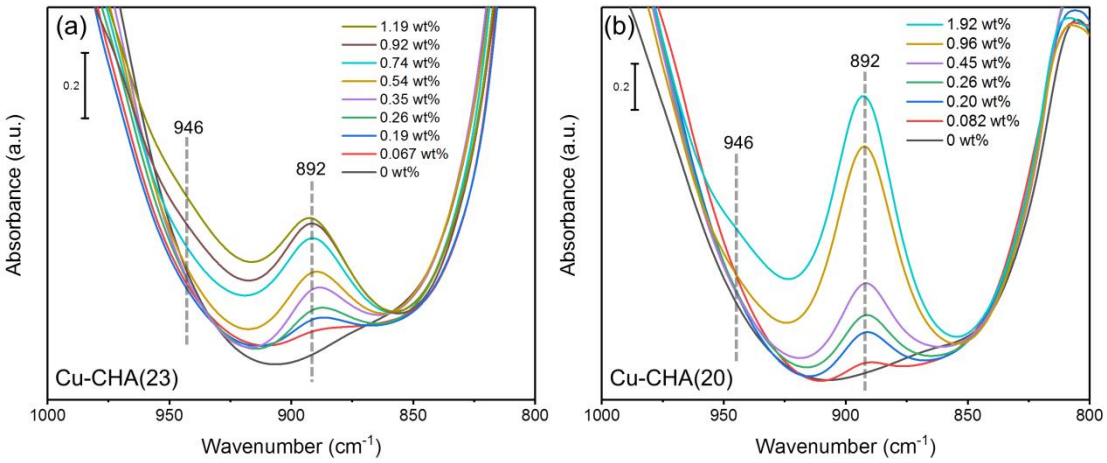

Figure 3.1. Transmission IR spectra of (a) Cu-CHA (SAR = 23, mostly isolated Al) and (b) Cu-CHA (SAR = 20, mostly paired Al) with various Cu-loading at 400 ^{o}C after flowing 40 mL min^{-1} dry air for 30 min.

To quantitatively investigate the connection between Cu speciation and Cu-loading on Cu-CHA, the $Z_2Cu(II)$ perturbed T-O-T feature at 892 cm^{-1} was integrated. Below a Cu-loading of 0.2 wt%, both sets of Cu-CHA show the same trend of $Z_2Cu(II)$ (**Figure 3.2**). The observation is in line with previous DFT calculations that $Z_2Cu(II)$ species are energetically favored for paired Al sites.[152] At Cu-loadings > 0.2 wt%, the quantity of $Z_2Cu(II)$ species plateaus for Cu-CHA(23), while the amount of $Z_2Cu(II)$ species continues to increase for Cu-CHA(20) up to 1.92 wt% Cu-loading. These observations agree with previous claims that the paired Al site will be saturated with Cu prior to filling of isolated Al sites.[152, 177] The Si-O stretching band strongly interferes with the $Z_1Cu(II)OH$ perturbed T-O-T framework vibration at 946 cm^{-1}, resulting in the appearance of a slight shoulder in higher Cu-loading Cu-CHA samples. Unfortunately, the interference makes the quantification of $Z_1Cu(II)OH$ species more challenging. Therefore, transmission IR spectra for Cu-CHA can only be applied for the quantification of $Z_2Cu(II)$ species based on perturbed T-O-T framework vibration at 892 cm^{-1}. Assuming that the sole species in < 0.2 wt% Cu-CHA(20) is $Z_2Cu(II)$ (IR band for $Z_1Cu(II)OH$ only emerges at loadings > 0.4

wt%), a calibration curve for $Z_2Cu(II)$ can be obtained and used for the quantification of $Z_2Cu(II)$ species (**Figure 3.2**).

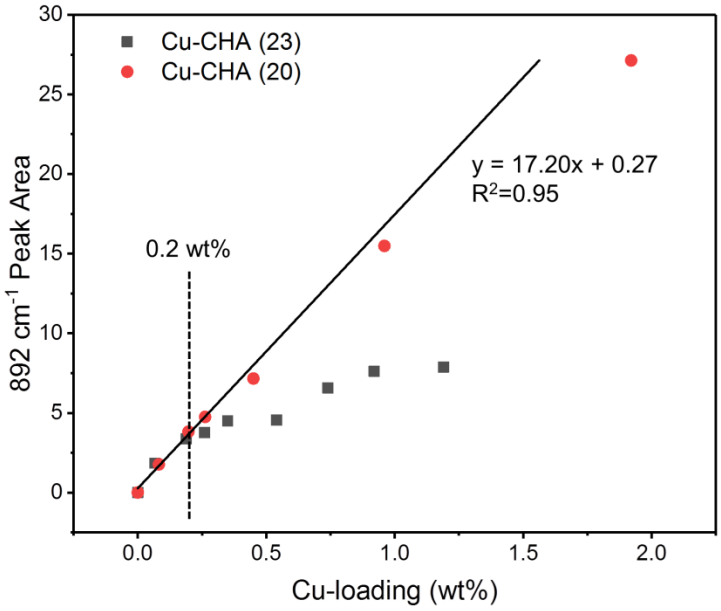

Figure 3.2. $Z_2Cu(II)$ perturbed T-O-T framework vibration IR peak area as a function of the corresponding Cu-loading. The calibration curve was fitted based on the Cu-CHA with Cu-loading below 0.2 wt%. Peak areas were normalized by the Si-O peak overtone from 1931 to 1768 cm^{-1} for each Cu-CHA IR spectrum at 400 ^{o}C under oxidative pretreatment.

Nitric oxide (NO) as a probe for Cu species in Cu-CHA

In addition to collecting the IR spectra of Cu-CHA under dry air to investigate Cu speciation, the use of probe molecules such as NO could help differentiate between Cu species. NO as a probe molecule shows enhanced sensitivity to Cu ions due to the extra electron in the $2\pi^*$ orbital. The extra electron in the $2\pi^*$ orbital of NO can be back donated to Cu^{2+} 3d orbital ; in contrast, Cu^{+} ions do not encounter the back donation from NO. This leads to notable vibrational changes when NO adsorbs on Cu^{2+} and Cu^{+}, which appear at 1850-1970 and 1809 cm^{-1}, respectively.[79] Although NO adsorption on Cu-CHA has been mentioned elsewhere,[78-79, 160, 178] identification and quantification of different Cu

species in Cu-CHA by IR spectroscopy has been limited due to the low stability of adsorbed NO on exchanged Cu species at room temperature and ambient pressure, which results in its decomposition to N_2O as well as the formation of NO^+ that could change the copper speciation.[174] This stability issue at ambient conditions makes the application of NO probes for Cu quantification challenging. Therefore, we investigated NO adsorption at cryogenic temperatures to avoid the undesired N_2O and NO^+ formation.

FT-IR NO adsorption was conducted at -160 ^oC on Cu-CHA by flowing 1000 ppm NO/N_2 for 30 minutes. N_2O formation from NO decomposition was not observed (**Figure S3.1**). NO adsorption shows IR peaks for symmetric and asymmetric stretching of the $Cu^+(NO)_2$ dinitrosyl species at 1826 and 1726 cm^{-1}, respectively.[78] A sharp peak at 1785 cm^{-1} emerges between the $Cu^+(NO)_2$ IR signals and is attributed to liquefied NO at -160 ^oC. The peak at 1785 cm^{-1} – as well as gas phase NO features at 1872 and 1850 cm^{-1} – was observed in the reference NO adsorption spectra on the parent CHA samples at the same conditions (**Figure S3.2**). The IR feature in the 1887 - 1915 cm^{-1} range can be attributed to $Cu^{2+}(NO)$ complexes from $Z_1Cu(II)OH$.[79]

NO adsorption IR spectra on Cu-CHA(20) and Cu-CHA(23) with Cu-loading ranging from 0 to 1.19 wt % were collected at -160 ^oC after flowing 1000 ppm NO/N_2 for 30 minutes (**Figure 3.3**). We note that the Cu-CHA samples were pretreated at 400 ^oC under dry air for 30 minutes before cooling down to -160 ^oC and initiating the NO adsorption IR experiments. The signal at 1887 cm^{-1} grew in intensity with increasing Cu-loading for both Cu-CHA types and was attributed to Cu(II)OH species.[79] In Cu-CHA(23), a side band emerged at 1904 cm^{-1} on 0.19 wt% Cu-CHA spectra and gradually shifted to 1909 cm^{-1} on 1.19 wt% Cu-CHA spectra (**Figure 3.3a**). The IR features appearing between 1887 and 1909 cm^{-1} provide insight into Cu(II)OH in different environments, but the specific IR assignments for Cu(II)OH in d6r and 8r remain unknown.[79, 154, 179] The

evidence for NO adsorbed on $Z_2Cu(II)$ appearing at 1956 cm^{-1} is qualitatively insignificant, indicating only a minor presence of $Z_2Cu(II)$ species.[79] A peak at 1826 cm^{-1} appears for copper loading ≥ 0.54 wt% Cu-CHA, attributed to a $Cu^+(NO)_2$ species. Although Cu-CHA is expected to contain mostly Cu^{2+} after air pretreatment, the presence of Cu^+ species has been attributed to the auto-reduction of Cu^{2+} while dehydration under high temperatures.[78, 180]

Cu-CHA(20) NO adsorption IR spectra exhibited more NO adsorption IR peaks than Cu-CHA(23) (**Figure 3.3b**). Other than the Cu(II)OH IR peaks at 1887 and 1902 cm^{-1}, a side band appears at 1915 cm^{-1}. The signal at 1915 cm^{-1} may be attributed to a $Z_1Cu(II)OH$ species or a pair of proximal Cu(II)OH species in adjacent d6r and 8r.[181-183] With increased Cu-loading larger than 0.45 wt%, a feature at 1936 cm^{-1} appeared, which may be attributed to Cu dimer species.[181] Indeed, due to the paired Al configuration in Cu-CHA(20), Cu-oxo dimers formation from the dehydration of two Cu(II)OH species in the same 8r cages is more facile than the dehydration from isolated Al Cu-CHA. This is evidenced by the lack of a 1936 cm^{-1} IR peak in the Cu-CHA(23) NO adsorption spectra (**Figure 3.3a**). Notably, this is the first Cu-CHA experimental study to report an IR peak assignment for a Cu dimer species at 1936 cm^{-1}. Yet, there are still debates for the occurrence of Cu-oxo or/and Cu-hydoxyl dimers.[154, 170-173] Based on our NO-IR results, the IR feature at 1936 cm^{-1} was attributed to Cu dimer including the possibility of Cu-oxo or/and Cu-hydoxyl dimers. Similar to Cu-CHA(23), the IR peak for Cu^+ from auto-reduction and $Z_2Cu(II)$ were also observed at 1826 and 1956 cm^{-1}, respectively.

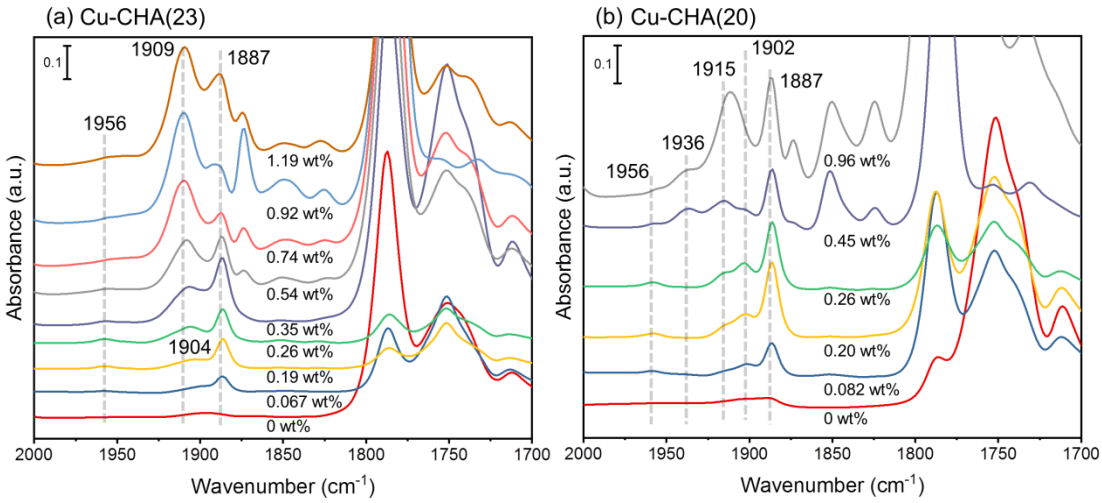

Figure 3.3. NO adsorption IR spectra of (a) Cu-CHA (SAR = 23) and (b) Cu-CHA (SAR = 20) at -160 ^{o}C with various Cu-loadings and were pretreated at 400 ^{o}C under dry air for 30 min with 1000 ppm NO/N_2 at 40 mL min^{-1}.

Quantitative analysis of Cu species by NO-IR

The integration of IR peaks for NO adsorbed on Cu^{+} and Cu^{2+} is used to quantitatively determine the amount of exchanged Cu in the CHA framework. The band for $Cu^{+}(NO)_2$ symmetric stretching at 1826 cm^{-1} represents the concentration of Cu^{+} species, while the asymmetric stretching band at 1726 cm^{-1} is not considered due to interference from the overlapping liquefied NO signal. The entire band for the $Cu^{2+}(NO)$ complexes was deconvoluted to several Cu^{2+} contributions: 1887, 1901, 1914, 1936, and 1956 cm^{-1} (**Figure S3.3-S3.4**). The assumption we made here is that the extinction coefficient for those NO adsorbed Cu^{2+} IR features are the same. Hence, the quantification results from every $Cu^{2+}(NO)$ IR peaks show that Cu-CHA(23) and Cu-CHA(20) share the same linear relation between the $Cu^{2+}(NO)$ IR peak area and Cu-loading, indicating that low temperature NO adsorption IR spectroscopy is a useful method for convenient Cu^{2+} quantification (**Figure 3.4a**). However, when the Cu-loading was larger than 0.40 wt%, the $Cu^{+}(NO)_2$ IR peak at 1826 cm^{-1} emerged, breaking the

linear correlation of Cu^{2+} to Cu-loading (**Figure 3.3**). In addition, $Cu^{2+}(NO)$ and $Cu^{+}(NO)_2$ do not have the same extinction coefficient; therefore, only Cu-CHA samples with Cu-loading below 0.40 wt% are used to derive the Cu^{2+} calibration curve from the oxidative pretreated Cu-CHA samples. The IR feature for non-exchanged copper species, *viz.* CuO_x,[184-185] was at 1874 cm^{-1} in Cu-CHA(23) and appeared for Cu-loadings ≥ 0.92 wt%, in agreement with the nonlinear correlation of $Cu^{2+}(NO)$ at high Cu weight loadings.

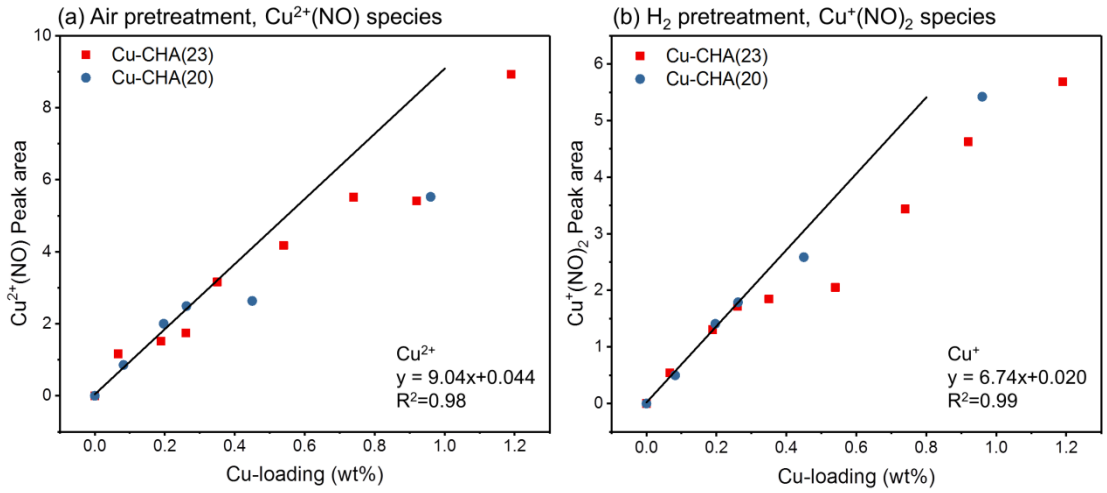

Figure 3.4. The correlation between (a) $Cu^{2+}(NO)$ (b) $Cu^{+}(NO)_2$ and various Cu-loadings on Cu-CHA(20) and Cu-CHA(23) at -160 ^{o}C. Peak areas were normalized by the Si-O peak overtone from 1931 to 1768 cm^{-1} for each Cu-CHA IR spectrum at 400 ^{o}C under oxidative or reductive pretreatment.

Since the auto-reduction of Cu^{2+} to Cu^{+} was difficult to avoid under oxidative pretreatment – especially at high Cu-loadings[78, 180] – an additional calibration curve for Cu^{+} species was required. H_2 reduction pretreatment was utilized to differentiate between the Cu^{2+} and Cu^{+} species in NO adsorption IR spectra. Previous studies have shown that the exchanged Cu^{2+} ion in CHA cages can be reduced at different temperatures. For example, the $Z_1Cu(II)OH$ species is reduced to Cu^{+} between 205 and 220 ^{o}C, the $Z_2Cu(II)$ is reduced to Cu^{+} between 300 and 350 ^{o}C,[165-167] and the non-exchanged Cu species (CuO_x) is reduced to Cu(0) below 200 ^{o}C.[186] Because of the stability of exchanged

copper species in CHA, exchanged Cu^+ is not reduced to Cu(0) until a temperature > 450 ^oC.[166] Thus, we used a H_2 pretreatment at 400 ^oC to ensure that all the exchanged Cu species were reduced to Cu^+ ions in order to establish the calibration curve for Cu^+ species from NO-IR.

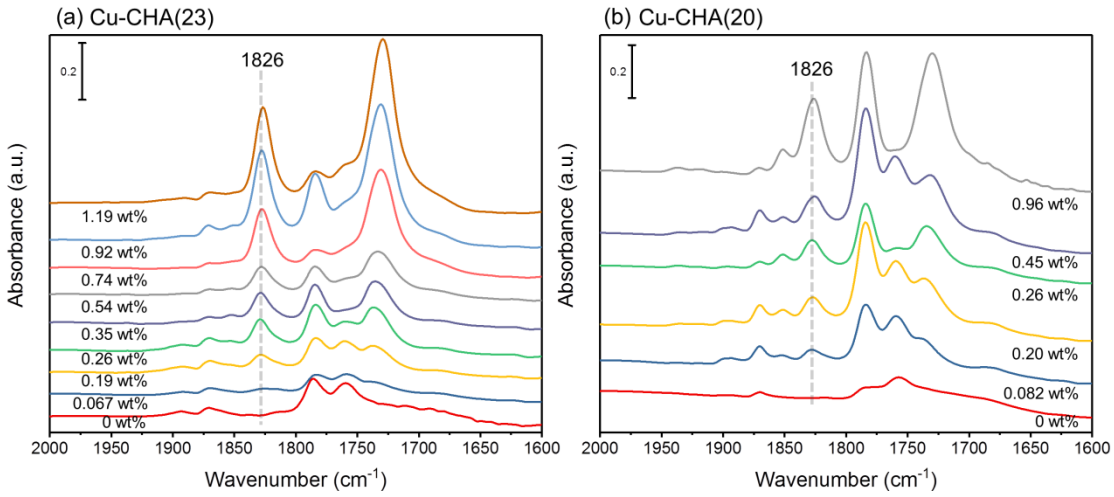

Figure 3.5. NO adsorption IR spectra of (a) Cu-CHA (SAR=23) and (b) Cu-CHA (SAR=20) at -160 ^oC with various Cu-loadings and were pretreated at 400 ^oC under 4% H_2/N_2 for 30 min with 1000 ppm NO/N_2 at 40 mL min^{-1}.

Compared to the oxidative pretreatment, the reductive pretreatment exhibited fewer IR peaks for NO adsorption (**Figure 3.5**). The main $Cu^+(NO)_2$ IR features appeared at 1826 and 1726 cm^{-1} for symmetric and asymmetric stretching, respectively. The gas phase NO, liquefied NO, and NO adsorbed on Brønsted acid sites were also observed at 1850, 1785, and 1892 cm^{-1}, respectively, which are consistent with previous literature findings and NO-IR spectra of the parent CHA.[79] For the quantification of Cu^+ species, the peak area for $Cu^+(NO)_2$ symmetric stretching at 1826 cm^{-1} was used, since the peak at 1726 cm^{-1} overlapped with IR features in the parent CHA. The results showed a linear correlation between $Cu^+(NO)_2$ and Cu-loading in each set of Cu-CHA (**Figure 3.4b**). The deviation from the linear correlation occurred above 0.40 wt% Cu and was attributed to the existence of a small amount of non-exchanged Cu species, CuO_x, on CHA. The non-

exchanged Cu species was detected in the NO-IR at 1874 cm^{-1} in samples with a Cu-loading above 0.40 wt% in the oxidative pretreatment NO-IR spectrum (**Figure 3.3**). Therefore, only Cu-CHA samples with Cu-loading below 0.40 wt% were used to create the calibration curve for Cu^{+} and Cu^{2+} species (**Figure 3.4, Figure S3.7**).

Application of Cu^{2+} and Cu^{+} calibration curves to high Cu-loading Cu-CHA samples

High Cu-loading samples – 2.96 to 3.99 wt% – were tested to examine the validity of the Cu^{+} and Cu^{2+} calibration curves. The powder Cu-CHA samples were pelletized into a wafer and pretreated at 400 ^{o}C under dry air or 4% H_2/N_2 for 30 minutes prior to NO adsorption IR measurements conducted at -160 ^{o}C. The NO-IR spectra of oxidatively pretreated Cu-CHA (**Figure 3.6a**) showed significant IR peaks for the $Cu^{2+}(NO)$ and $Cu^{+}(NO)_2$ species. The IR peaks were deconvoluted to 1887, 1911, 1936, and 1956 cm^{-1}, which were attributed to $Cu^{2+}(NO)$ species (**Figure S3.8**). Additionally, gas phase NO features appeared at 1872 and 1850 cm^{-1}. The IR peak at 1826 cm^{-1} was attributed to $Cu^{+}(NO)_2$ species formed from auto-reduction. The IR peak area for $Cu^{2+}(NO)$ at 1887, 1911, 1936 and 1956 cm^{-1} were summed and applied to the Cu^{2+} calibration curve. Here, we assumed that the extinction coefficients were the same for all $Cu^{2+}(NO)$ species used in the determination of the calibration curve. In addition, $Cu^{+}(NO)_2$ species were also integrated and applied for Cu^{+} calibration curve to estimate the amount of exchanged Cu in CHA. **Figure 3.6b** shows NO-IR of reduced powder Cu-CHA samples. Compared to the air pretreatment, only $Cu^{+}(NO)_2$ species appeared at 1826 cm^{-1}, which simplified the quantification.

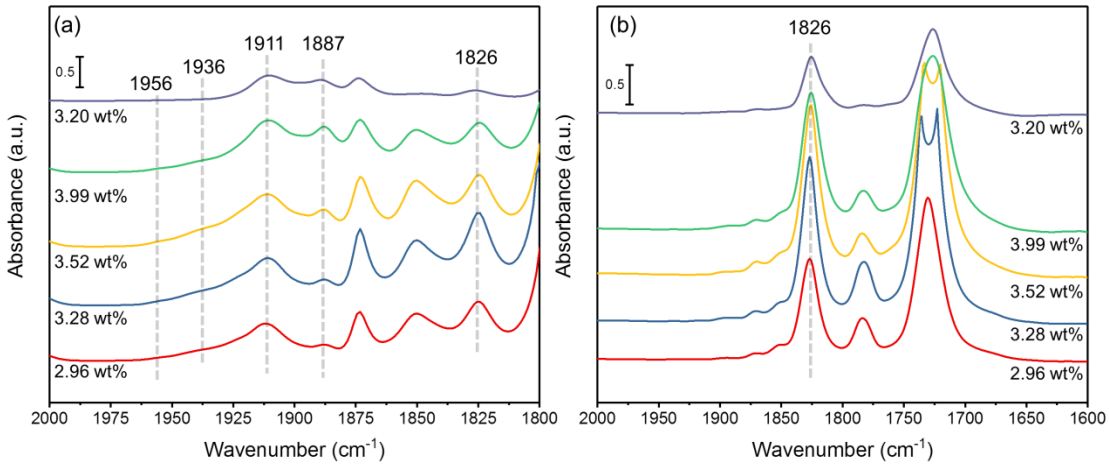

Figure 3.6. NO adsorption IR spectra of Cu-CHA samples pretreated at 400 ^{o}C under (a) dry air and (b) 4% H_2/N_2 for 30 min at 40 mL min^{-1}. The split or inverse peak shape at 1726 cm^{-1} in (b) is due to the saturation of MCT detector

The total Cu-loading was measured by ICP-OES, and compared with the results obtained by NO-IR (only detecting exchanged Cu), in **Table** 3.**1**. The quantity of exchanged Cu species in each sample, independent of pretreatment, were very similar (discrepancy < 5%). The small discrepancy proved that the calibration curves from low Cu-loading Cu-CHA can be applied to estimating high Cu-loading Cu-CHA samples, as well as Cu-CHA with different SAR. In addition, the amount of non-exchanged Cu, obtained from the difference between ICP and NO-IR value, was less than 0.3 wt%. The quantity of non-exchanged Cu indicates that CuO_x was difficult to avoid in the aqueous phase ion exchanged synthetic method for high Cu-loading Cu-CHA. Additionally, the result for Cu-CHA (SAR = 22) with 3.20 wt% indicates that the sample contains more CuO_x species, because the discrepancy between the ICP and NO-IR values is 1.03 and 0.69 wt% with dry air and H_2 pretreatment, respectively.

Table 3.1. The amount of Cu species obtained from ICP-OES, NO-IR, H_2-TPR

Cu-CHA SAR	ICP Cu wt%	IR (Air) wt%	IR (H_2) wt%	Calculated H_2 (mL/g)	H_2-TPR (mL/g)
16	2.96	2.82	2.72	3.96	4.15
16	3.28	3.19	3.12	4.06	4.50
19	3.52	3.34	3.42	4.98	4.49
19	3.99	3.67	3.53	6.13	5.13
22	3.20	2.17	2.51	3.33	3.41

We further validate our results with hydrogen temperature-programmed reduction (H_2-TPR) which was used for investigating exchanged Cu species in Cu-CHA.[165-167] Based on previous reports,[165-166] the reduction of $Z_1Cu(II)OH$ to Cu^+ occurred at 200 ^oC and $Z_2Cu(II)$ to Cu^+ reduced at 300 ^oC. The increased reduction temperature for $Z_2Cu(II)$ was attributed to a more stable species. In contrast, the non-exchanged Cu species (CuO_x) reduced to Cu(0) below 200 ^oC under hydrogen gas. For the H_2-TPR of high Cu-loading Cu-CHA samples, two reduction peaks were observed at 210 ^oC and 320 ^oC, corresponding to the reduction of $Z_1Cu(II)OH$ and $Z_2Cu(II)$ species, respectively, to Cu^+ (**Figure S3.10**). Therefore, we estimated the H_2 consumption from the oxidative pretreatment NO-IR results. The reduction of $Z_1Cu(II)OH$ and $Z_2Cu(II)$ required half the amount of H_2, while CuO_x takes a full equivalent of H_2 to reduce to Cu(0). The amount of exchanged Cu was obtained from NO-IR results, and CuO_x wt% was obtained from the difference between ICP and NO-IR results. Cu-CHA samples were first treated at 400 ^oC under dry air for 30 minutes before conducting the H_2-TPR. Thus, the predicted H_2 consumption volume was based on NO-IR results from dry air pretreatment. The differences between NO-IR and H_2-TPR results in all samples are within 5%, which demonstrates the reliability of the NO-IR methodology to quantify exchanged Cu species

in Cu-CHA. The advantage of the NO-IR method over H_2-TPR is that it both determines the amount of exchanged Cu species and identifies the different Cu speciation, such as $Z_1Cu(II)OH$, $Z_2Cu(II)$ and Cu dimers, in the parent CHA with different SARs and Al distributions. The information of Cu speciation in Cu-CHA can be correlated to deNO_x-SCR or methane to methanol reactivity, which enables future catalyst development.

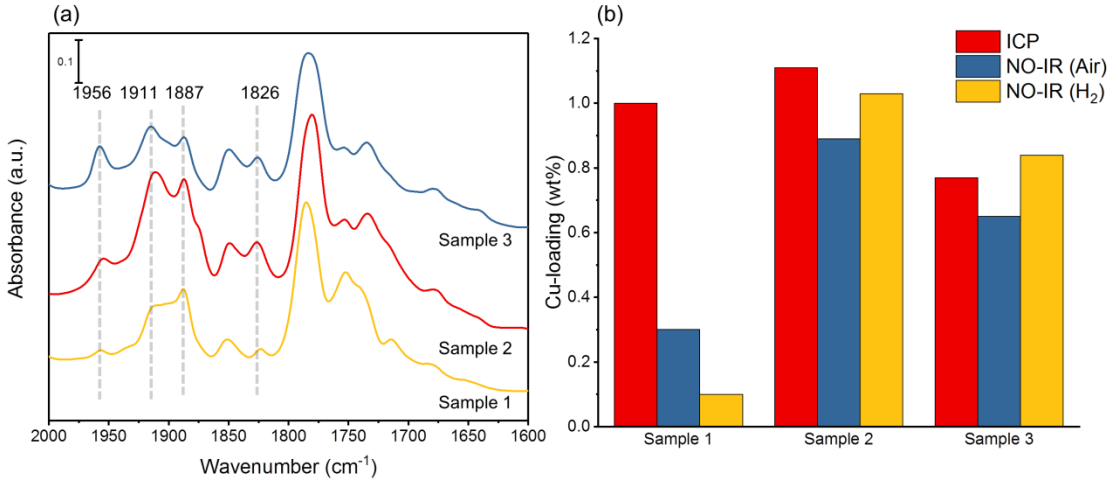

Figure 3.7. (a) NO adsorption IR spectra of Cu-CHA honeycomb samples at -160 ^oC after pretreated at 400 ^oC under dry air for 30 min with 1000 ppm NO/N^2 at 40 mL min^{-1}. (b) The amount of exchanged Cu species derived from ICP-OES, NO adsorption IR at -160 ^oC

After validating the NO-IR results with H_2-TPR method for high Cu-loading Cu-CHA samples, we applied the NO-IR technique to Cu-CHA coated honeycomb samples commercially used for the treatment of diesel engine exhaust. The Cu-CHA honeycomb washcoat samples were crushed and ground into powder prior to pressing into an IR wafer and ICP measurement. The NO adsorption IR spectra for Cu-CHA honeycomb samples at -160 ^oC showed distinct IR peaks for $Cu^{2+}(NO)$ species (1887, 1911, 1956 cm^{-1}) and $Cu^{+}(NO)_2$ species (1826 cm^{-1}) (**Figure 3.7a**). The NO adsorption IR spectra were deconvoluted (**Figure S3.11**) and the IR peaks corresponds to exchanged Cu species were calculated by using calibration curves (**Figure 3.4**). Similarly, the NO adsorption IR spectra of the Cu-CHA honeycomb samples with reductive pretreatment

were also performed and deconvoluted (**Figure S3.12**). The estimated amount of exchanged Cu species for the tested Cu-CHA honeycomb samples were obtained from NO-IR and compared to the ICP results (**Figure 3.7b**). We noted that sample 1 was heavily aged at 800 ^{o}C for 16 hours under oxidative condition with moisture, while sample 2 was aged at 600 ^{o}C for 50 hours under oxidative condition with moisture. Additionally, sample 3 was a fresh Cu-CHA honeycomb sample. The amount of exchanged Cu obtained from NO-IR of sample 2 and 3 showed reasonable results compared to Cu wt% from ICP, whereas the discrepancy of NO-IR and ICP Cu wt% values were the amount of non-exchanged Cu species. However, the amount of exchanged Cu species derived from NO-IR of sample 2 and 3 with reductive pretreatment showed slightly higher values, 0.14 and 0.20 wt%, respectively, than NO-IR with dry air pretreatment. Furthermore, the NO-IR result after reductive pretreatment in sample 3 was even higher than the ICP value which was abnormal. Indeed, the quality of IR peak fitting of NO-IR with reductive pretreatment was not performed well compared to NO-IR with dry air pretreatment and it may be attributed to the unevenness of the baseline (**Figure S3.12**). Therefore, the estimated exchanged Cu wt% from NO-IR with dry air pretreatment would be more reliable in wash-coated samples. In addition, the estimated exchanged Cu wt% from NO-IR of sample 1 showed much less exchanged Cu species indicating that there was more non-exchanged Cu species (CuO_x) appearance on Cu-CHA. Since sample 1 was heavily aged at 800 ^{o}C for 16 hours before measurement, NO-IR results actually matched that exchanged Cu species can migrate out of the framework as CuO_x at 800 ^{o}C. Although NO-IR with reductive pretreatment showed inconsistent values compared to ICP results in Cu-CHA honeycomb samples, the estimated exchanged Cu wt% from NO-IR with dry air pretreatment appeared to be the better method for quantifying exchanged Cu species in Cu-CHA honeycombs.

3.3 Conclusion

In this work, we established a facile way to determine the quantity of Cu species and the different Cu speciation in Cu-CHA, as compared to the conventional ICP-OES method that does not differentiate between exchanged and non-exchanged Cu species. We also demonstrated that $Z_2Cu(II)$ species can be quantified using the perturbed T-O-T vibration at 892 cm^{-1}. Two Cu-CHA catalysts were tested, one consisting of mostly isolated Al sites while the other consisting of mostly paired Al sites in the CHA cages. A linear correlation between the $Z_2Cu(II)$ species and the Cu-loading was observed when the Cu-loading was below 0.3 wt%, which is consistent with previous reports showing that the Cu ion located at paired Al sites is more favorable than isolated Al sites. The NO adsorption IR experiments were performed at cryogenic temperatures (-160 ^oC) to eliminate the decomposition of NO to N_2O over Cu-CHA. The IR features of $Cu^+(NO)_2$ and $Cu^{2+}(NO)$ at 1826 and 1887-1956 cm^{-1} were evaluated for Cu-CHA catalysts with Cu-loadings of less than 0.40 wt% to obtain calibration curves for Cu^+ and Cu^{2+} ions. Various peaks were assigned for $Cu^{2+}(NO)$ at 1887, 1902, 1909, 1914, 1936, and 1956 cm^{-1}, which corresponded to Cu^{2+} ions in different CHA cage environments. Based on our experimental results and previous literature, the peaks from 1887 to 1915 cm^{-1} were attributed to $Z_1Cu(II)OH$ species in d6r and 8r and NO adsorption on $Z_2Cu(II)$ sites appeared at 1956 cm^{-1}. In addition, the IR peak at 1936 cm^{-1} only appeared in the IR spectra of Cu-CHA(20) samples that consisted mostly of paired Al configurations. The 1936 cm^{-1} IR feature was predicted to correspond to Cu dimers, such as Cu-oxo species - a result that is first reported here.

The calibration curves for Cu^+ and Cu^{2+} ions were established from NO-IR by using both reductive and oxidative pretreatment. Then, the calibration curves were applied for high Cu-loading Cu-CHA samples to investigate the amount of exchanged Cu species in

Cu-CHA. In addition, H_2-TPR was performed as a complementary technique to verify the consistency and accuracy of NO-IR method for exchanged Cu quantification. The estimated Cu^+ and Cu^{2+} amount from NO-IR and H_2-TPR results were consistent indicating that the NO-IR methodology is a promising way to determine the amount of exchanged Cu species in Cu-CHA. NO-IR can access the nature of the Cu speciation such as $Z_2Cu(II)$, $Z_1Cu(II)OH$, and Cu dimers. The information of Cu speciation in Cu-CHA can then be correlated with the deNO_x-SCR reactivity to accelerate catalyst development. Lastly, we applied NO-IR method to coated Cu-CHA honeycomb samples and demonstrated the success for facile quantification of exchanged Cu species even in different type of samples.

3.4 Experimental details

Cu-CHA synthesis

Two sets of Cu-CHA samples were synthesized for spectroscopic measurements. The first set of Cu-CHA (SAR=23, parent CHA provided by BASF) samples with predominantly isolated Al sites contains Cu-loadings of 0.067-1.19 wt%. The second set of Cu-CHA (SAR=20, parent CHA provided by BASF) samples with mostly paired Al sites contains Cu-loadings of 0.082-0.96 wt%. The exact Cu-loading in the CHA samples was measured by inductively coupled plasma optical emission spectroscopy (ICP-OES) analysis.

To prepare the Cu-CHA samples, 150 mg of parent CHA powder is well-dispersed in 10 mL of $Cu(NO_3)_2$ solution (18.2 MΩ water) at concentrations of 0.5-20 mM, stirred at 300 rpm for 4 hours at room temperature, and maintained at a pH of 4.8-5.0 by dropwise addition of 0.1 M $NH_4OH_{(aq)}$. The various Cu-CHA samples are then centrifuged and washed 3 times with DI water to remove excess Cu ions on the samples. To achieve

higher Cu-loadings, the samples already treated in a 20 mM Cu^{2+} solution are dispersed again in 20 mM $Cu(NO_3)_2$ solutions, repeating the same procedure to increase the ion exchange level. The washed Cu-CHA samples are dried in an oven at 110 ^oC for 24 hours. The dry Cu-CHA samples are then calcined in a muffle furnace under air flow at 500 ^oC for 4 hours with a ramp rate of 1 ^oC/min.

NO adsorption FT-IR spectroscopy

For FT-IR analysis, 5 mg Cu-CHA sample is pressed into a self-supported thin wafer that is placed in a homemade in-situ transmission IR flow cell which can be heated to 400 ^oC and cooled to -170 ^oC. The Cu-CHA honeycomb samples were taken from a small portion of the washcoat and ground to fine powder prior to IR pellet preparation. All FT-IR measurements were performed in a Bruker Vertex 70 spectrometer equipped with a liquid nitrogen cooled Mercury-Cadmium-Telluride (MCT) detector. Typically, 128 scans with a resolution of 4 cm^{-1} were averaged to give one spectrum. Prior to a low temperature NO adsorption measurement, the cell is heated at 5 ^oC/min to 400 ^oC and held for 30 min under 40 mL/min dry air or 4 % H_2/N_2 to have oxidative and reductive pretreatments. After oxidative pretreatment, the cell is cooled down to 200 ^oC with flowing dry air to avoid auto-reduction, and then evacuated by a turbo pump (pressure < $1x10^{-5}$ Torr). In contrast, after the reductive pretreatment, the cell is then evacuated by a turbo pump (pressure < $1x10^{-5}$ Torr) at 400 ^oC. To begin low temperature NO adsorption, the cell is first cooled to room temperature before it is further cooled to -160 ^oC by liquid nitrogen.

A background FT-IR spectrum is collected at -160 ^oC under vacuum before feeding NO. 1000 ppm NO diluted in N_2 is then fed into the cell for 40 min, and the spectra – referred to as NO adsorption FT-IR spectra – are collected at 1 min intervals. All

adsorption FT-IR spectra are collected under low temperature (-160 ^{o}C) conditions maintained by constantly adding liquid nitrogen to the transmission IR cell. To compare and quantify the Cu^{+} and Cu^{2+} IR band integrals in different Cu-CHA, all IR spectra are first normalized by using Si-O overtone with the area, 6.588, from 1931 to 1768 cm^{-1} for each Cu-CHA IR spectrum at 400 ^{o}C under oxidative or reductive pretreatment before cooling down and feeding NO to serve as an internal standard.

H_2 Temperature-Programmed Reduction (H_2-TPR)

Hydrogen temperature programmed reduction (H_2-TPR) is performed in Micromeritics Autochem II. Cu-CHA samples were first oxidized by flowing 50 mL/min dry air with 5 ^{o}C/min to 400 ^{o}C. After holding at 400 ^{o}C with dry air for 30 min, Cu-CHA samples were cool down to room temperature prior to H_2-TPR. Cu-CHA samples with oxidative pretreatment are then reduced by flowing 50 mL/min 10% H_2/Ar with 5^{o}C/min to 400 ^{o}C and the H_2 consumption was monitored by a TCD detector.

Chapter 4: Low Temperature NO and CO-IR Methodology for Identifying and Quantifying Exchanged Metal Ion in Cu-ZSM-5 and Fe-CHA

This work is the extension of NO as a probe in low temperature IR methodology mentioned in previous chapter. The identification and quantification of ion-exchanged species in Cu-ZSM-5 and Fe-CHA were investigated by NO and CO-IR. The study pointed out the potential of low temperature technique to characterize other metal ion-exchanged zeolites.

4.1 Introduction

After successfully quantifying and identifying exchanged Cu species in Cu-CHA, we further extend this methodology to another zeolite, Cu-ZSM-5, which has also been studied for the conversion of methane to methanol for decades.[187-191] With the availability of shale gas, methane, has been replacing crude oil as a feedstock for value added chemicals in the United States.[192] Methanol, one of the products derived from methane, serves as an important feedstock for many valuable chemicals such as formaldehyde, dimethyl ether, olefins, and acetic acid.[1, 193] The conventional route for producing methanol is a two-step process: 1) syngas ($CO + H_2$) production from natural gas or coal, 2) syngas conversion to methanol using a Cu-ZnO-Al_2O_3 catalyst. Although the two-step process has been widely applied for methanol production, the direct one-step conversion from methane-to-methanol would be more desired.[194-197]

The ion-exchanged Cu-ZSM-5 shows activity for partial oxidation of methane-to-methanol after activation under O_2 and N_2O condition.[191] In order to establish structure-reactivity correlations and to further characterize the nature of Cu species in Cu-ZSM-5, X-ray absorption spectroscopy (XAS),[198-200] UV-vis spectroscopy,[188, 190] diffused reflectance Infrared spectroscopy (DRIFTS),[201] Raman spectroscopy,[202-204] and electron

paramagnetic resonance (EPR)[205] have been implemented. The possible active sites for methane to methanol are the Cu-oxo species including mono-μ-oxo dicopper, tris-μ-oxo-tricopper, *trans*-μ-1,2-peroxo dicopper, *cis*-μ-1,2-peroxo dicopper, copper hydroxyl, and m-(η^2:η^2)-peroxo dicopper species (**Figure 4.1**).[199] Although there are still some debates about the responsible copper species for methane to methanol, it is almost undeniable that the exchanged copper in Cu-ZSM-5 acts as a crucial role for methane conversion.

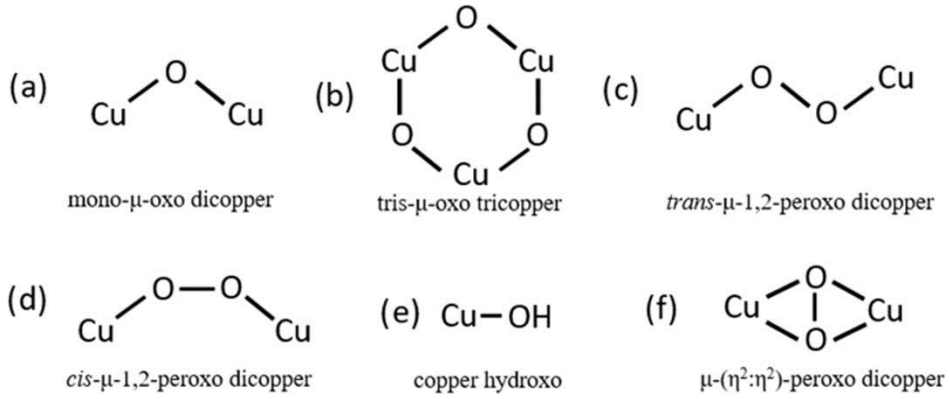

Figure 4.1. The possible structure of copper-oxygen species proposed as active site for methane to methanol in Cu-exchanged zeolites. Adapted from ref 199.

Other than methane to methanol conversion, Cu-ZSM-5 is also an alternative catalyst for the direct conversion of syngas to dimethyl ether.[206] In fact, Cu-ZnO-Al_2O_3/ZSM-5 is being studied as a bifunctional catalyst for the tandem conversion of syngas (**Figure 4.2**).[5-6, 207-208] Syngas is first converted into methanol over Cu/ZnO sites, and then acid sites on ZSM-5 further dehydrate the methanol into dimethyl ether. In this application, Cu(0), reduced from CuO_x on Cu-ZSM-5, behaves as an active site for the syngas to methanol step. However, when impregnating copper into ZSM-5 zeolite, the ion-exchange sites can also accommodate some Cu species and the exchanged copper species which is the unwanted surface site for syngas to methanol is less active than the Cu(0). In order to build the structure-reactivity correlation with Cu-ZSM-5 and syngas conversion, a quantitative method is required to estimate the two types of copper species.

Herein, we expand the application of NO-IR to include quantifying and identifying copper species in Cu-ZSM-5.

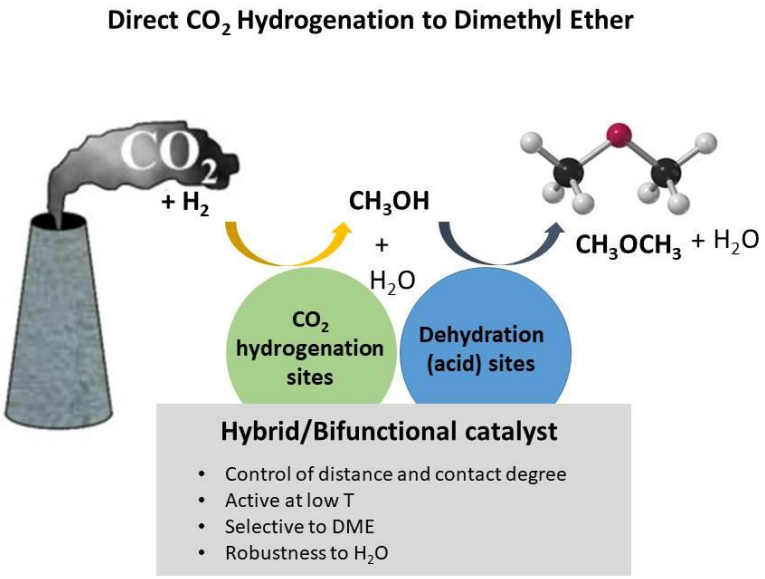

Figure 4.2. Direct synthesis from syngas to dimethyl ether on bifunctional catalyst. Adapted from ref 206.

Cu-CHA is already a successful commercial catalyst for exhaust treatment from lean burn diesel engines, and the catalyst shows a good hydrothermal stability with a full conversion of NO_x (NO, NO_2).[143] Although Cu-CHA appears full conversion for the deNO_x treatment at 400-600 ^oC, there are still some unwanted side products, such as nitrous oxide N_2O (~0.2 %).[209-211] Indeed, N_2O is another greenhouse gas, which shows ~300 times higher impact than CO_2 on global warming. N_2O is also known to deplete the ozone layer in the stratosphere.[212-215] With the increasing emission regulations in the foreseeable future, Fe-CHA has drawn attention in recent years due to its ability to fully convert NO_x to N_2 and H_2O at above 400 ^oC, avoiding the formation of N_2O, despite being less reactive compared to Cu-CHA.[216]

Unlike the synthesis of Cu-exchanged CHA at room temperature and ambient conditions, Fe-CHA synthesis involves an Fe^{2+}/Fe^{3+} ion exchange at 80 ^{o}C under inert conditions. Due to the formation of bulky Fe-containing moieties (FeOOH) or clusters (Fe_2O_3), the Fe species are difficult to diffuse into CHA pores.[217] In addition, by using an Fe^{3+} solution during synthesis, agglomeration typically occurs due to the formation of an iron aqueous complex, $Fe(H_2O)_6^{3+}$, which cannot easily diffuse into zeolite pores, resulting in mainly iron oxide (Fe_2O_3) formation out of the zeolite framework.[218-219] Therefore, in order to avoid the bulky Fe species formation by O_2 and Fe_2O_3 formation during synthesis, the Fe-exchange needs to operate under N_2 and using Fe^{2+} as the precursor.

Compared to the copper speciation in Cu-CHA, there is less literature focusing on the speciation of iron in Fe-CHA due to its inferior deNO_x activity compared to Cu-CHA. From the results of UV-vis and EPR, there are several species in Fe-CHA such as isolated Fe^{3+} ions, dinuclear $[HO—Fe—O—Fe—OH]^{2+}$, and Fe_2O_3 particles.[218, 220-221] Yet, the speciation of those Fe^{3+} species in CHA cages are still unclear at the time. In contrast, Fe^{2+} species has been observed in d6r and 8r of CHA cages by using NO and CO adsorption in IR spectroscopy.[222] A possible reason is that the pretreatment condition heavily impacts the Fe species in Fe-CHA, which is also similar to the case of Cu-CHA. The Fe^{3+} species have been observed without calcination or high temperature treatment (> 350 ^{o}C), while Fe^{2+} species were discovered with either vacuum treatment or air calcination at 400 ^{o}C. Nonetheless, it is still unclear what the mechanism of auto-reduction from Fe^{3+} to Fe^{2+} is at high temperatures. In order to be consistent with the previous FT-IR study, we chose air calcination at 400 ^{o}C as the pretreatment prior to IR spectra collection. Here, we extend the application of NO and CO as probe molecules to identify and quantify Fe species in Fe-CHA using IR spectroscopy.

4.2 Results and Discussion

Extending the NO-IR method to Cu-ZSM-5

We first treated Cu-exchanged ZSM-5 (SAR = 30) with different Cu-loadings at 400^{o}C for 30 minutes under dry air prior to collecting the IR spectra. Similar to the case of Cu-CHA, an IR feature at 924 cm^{-1} emerged due to perturbed T-O-T framework vibration in Cu-ZSM-5 compared to the original framework vibration at 1040 cm^{-1} (**Figure 4.3**). Since the Cu speciation in Cu-ZSM-5 was mostly considered as mono-μ-oxo dicopper species in 10-membered rings (10r),[199] the perturbed framework vibration here can be attributed to Cu dimer species. In addition, the intensity of 924 cm^{-1} peak enhanced with increasing Cu-loading in Cu-ZSM-5. However, the IR peak at 924 cm^{-1} was overlapped by the huge IR contribution from Si-O stretching in ZSM-5. Thus, we did not continue to use the IR spectra at 400 ^{o}C for quantification purposes.

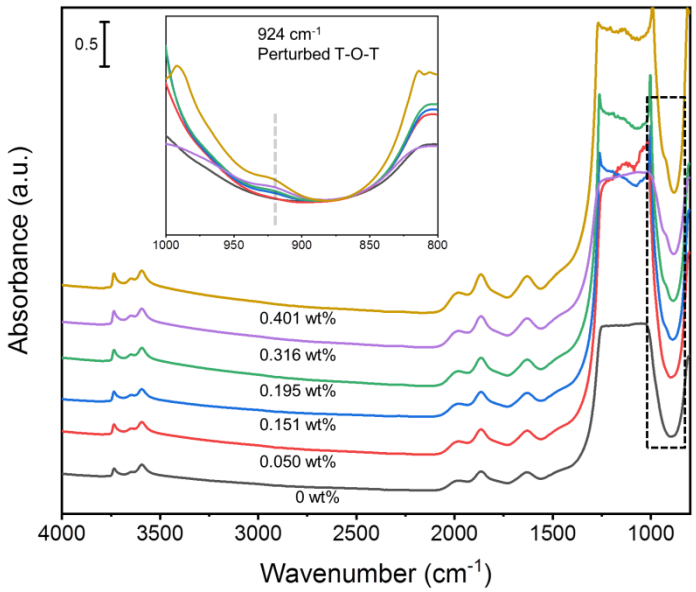

Figure 4.3. Transmission IR spectra of Cu-ZSM-5 (SAR = 30) with various Cu-loadings at 400 ^{o}C after flowing 40 mL min^{-1} dry air for 30 min.

Subsequently, the NO adsorption IR spectra of Cu-ZSM-5 were collected at -160 ^{o}C under 1000 ppm NO/N_2 after an oxidative or reductive pretreatment, and the spectra showed no N_2O or NO^+ formation, which indicates NO is still an appropriate probe molecule for investigating Cu speciation in Cu-ZSM-5 in addition to Cu-CHA (**Figure S4.1**). NO adsorption IR spectra of Cu-ZSM-5 after oxidative pretreatment showed an IR signal at 1914 cm^{-1}, which can be attributed to Cu^{2+}(NO) species (**Figure 4.4a**). In addition, the IR feature of liquefied NO appeared at 1785 cm^{-1}, consistent with the finding in NO adsorption IR spectra of Cu-CHA and NO reference spectra as well as the NO gas phase IR signals at 1856 and 1865 cm^{-1}. The peak intensity at 1914 cm^{-1} grew in intensity with increasing Cu-loading in Cu-ZSM-5. When operating an NO adsorption IR experiment of Cu-ZSM-5 after the reductive pretreatment, both Cu^{2+}(NO) and $Cu^{+}(NO)_2$ emerged at 1914 and 1820 cm^{-1}, respectively (**Figure 4.4b**), indicating Cu^{2+} species is not fully reduced to Cu^+ species by using 4% H_2/N_2 at 400 ^{o}C for 30 min. Thus, we only used the NO adsorption IR spectra after the oxidative pretreatment to quantify Cu^{2+} species in Cu-ZSM-5, because it seems that reductive pretreatment cannot separate Cu^{2+} and Cu^+ species in Cu-ZSM-5. The linear calibration curve for Cu^{2+} species as a function of the Cu loading is shown in **Figure 4.5**. We noticed that the amount of Cu^{2+}(NO) in the Cu-ZSM-5 sample with the largest Cu loading (0.401 wt%) deviated from the calibration curve, which could indicate the appearance of non-exchanged Cu species, CuO_x.

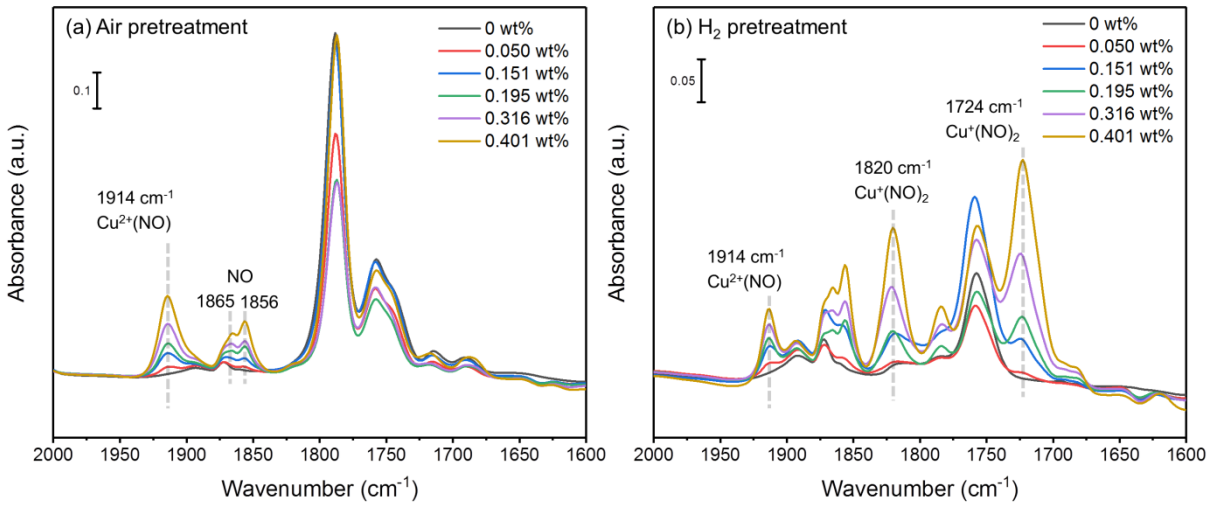

Figure 4.4. NO adsorption IR spectra of Cu-ZSM-5 (SAR = 30) samples pretreated at 400 ^{o}C under (a) air and (b) 4% H_2/N_2 after flowing 1000 ppm NO/N_2 for 30 min at -160 ^{o}C.

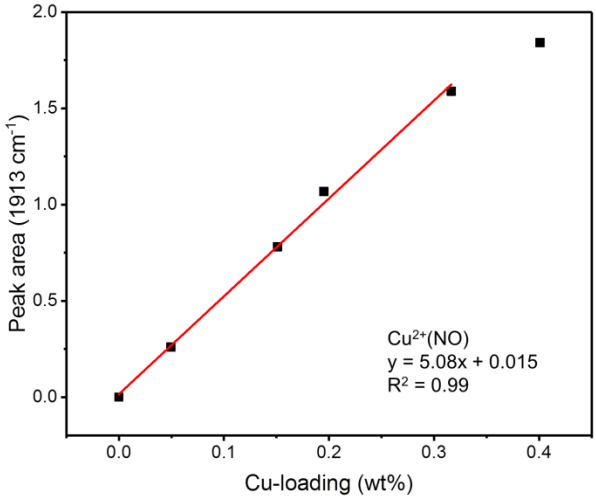

Figure 4.5. Calibration curve for Cu^{2+} species as a function of the Cu loading in Cu-ZSM-5 using NO-IR at -160 ^{o}C.

In the application of Cu-ZSM-5 for syngas conversion to dimethyl ether, the active site for the step of syngas to methanol was proposed to be CuO_x, which is non-exchanged Cu species. We thereby examined a high silica content Cu-ZSM-5 (SAR = 400), which does not contain abundant exchanged Cu species due to the limited number of Brønsted acid sites. The Cu-ZSM-5 samples were prepared using a liquid phase ion exchange procedure to synthesize Cu-ZSM-5 with various Cu-loadings. The NO

adsorption IR spectra of Cu-ZSM-5 (SAR = 400) showed a broad IR band from 1930 to 1855 cm^{-1} (**Figure 4.6a**). Compared to the low SAR Cu-ZSM-5 (SAR = 30) (**Figure 4.4a**), the IR peak for Cu^{2+}(NO) at 1914 cm^{-1} is insignificant and could be buried in the broad band at 1896 cm^{-1} in high SAR Cu-ZSM-5 (SAR = 400). In addition, the deconvoluted NO adsorption IR spectrum of Cu-ZSM-5 (SAR = 400) with 0.549 Cu wt% indicated four main contributions for the broad band (**Figure S4.2**). The IR peak at 1914 cm^{-1} corresponded to Cu^{2+}(NO) species, 1896 cm^{-1} could be attributed to adsorbed NO on CuO_x species, and the contribution of NO gas phase IR signal appeared at 1872 and 1860 cm^{-1}. Because of the limited number of Brønsted acid sites on ZSM-5 with high SAR (SAR = 400), the exchanged Cu species was rare, suggesting that the Cu speciation was mostly non-exchanged CuO_x on Cu-ZSM-5 (SAR = 400). In this case, we can deconvolute the NO adsorption IR spectra of each Cu-ZSM-5 (SAR = 400) with different Cu-loadings and apply the calibration curve of Cu^{2+} that we obtained above to calculate the amount of exchanged Cu species (**Figure 4.5**). Furthermore, the difference between the exchanged Cu species and bulk Cu content could be used to estimate the amount of CuO_x on Cu-ZSM-5 (**Figure 4.6b**). Based on the NO-IR results, the exchange sites in Cu-ZSM-5 (SAR = 400) are restricted, and they can only accommodate 0.04-0.05 wt% of exchanged copper species, because the exchanged copper species seems to plateau around these values despite increasing the Cu loading.

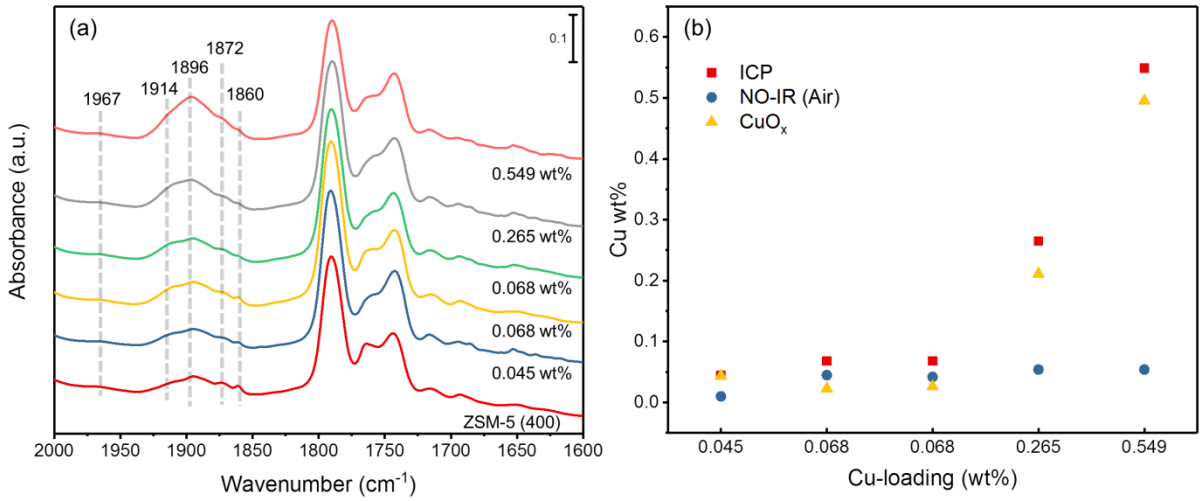

Figure 4.6. (a) NO adsorption IR spectra of Cu-ZSM-5 (SAR = 400) samples pretreated at 400 ^{o}C under dry air after flowing 1000 ppm NO/N_2 for 30 min at -160 ^{o}C. (b) The amount of Cu species derived from ICP-OES and NO-IR.

Extending the NO and CO-IR method to Fe-CHA

We later investigated the Fe-exchanged CHA, which is another active catalyst for deNO$_x$-SCR. The Fe-CHA (SAR = 20) with various Fe-loadings were treated at 400 ^{o}C under dry air to remove the moisture and activate the catalyst prior to IR spectra collection. An IR peak at 901 cm^{-1} similar to the one attributed to the perturbed T-O-T framework vibration of Z_2Cu(II)[156] was observed in every Fe-CHA sample (**Figure 4.7**), implying that Z_2Fe(II) is also the favorable site for Fe ions in low Fe-loadings, which is similar to the copper speciation in Cu-CHA. In addition, the intensity of the Z_2Fe(II) IR feature enhanced with increasing the Fe-loading. However, the Z_2Fe(II) IR peak was overlapped with the intense and broad Si-O IR signal which makes the IR peak integration at 901 cm^{-1} more difficult. In order to further identify and quantify Fe species in Fe-CHA, we extend our low temperature (-160 ^{o}C) NO and CO-IR methodology to investigate Fe-CHA.

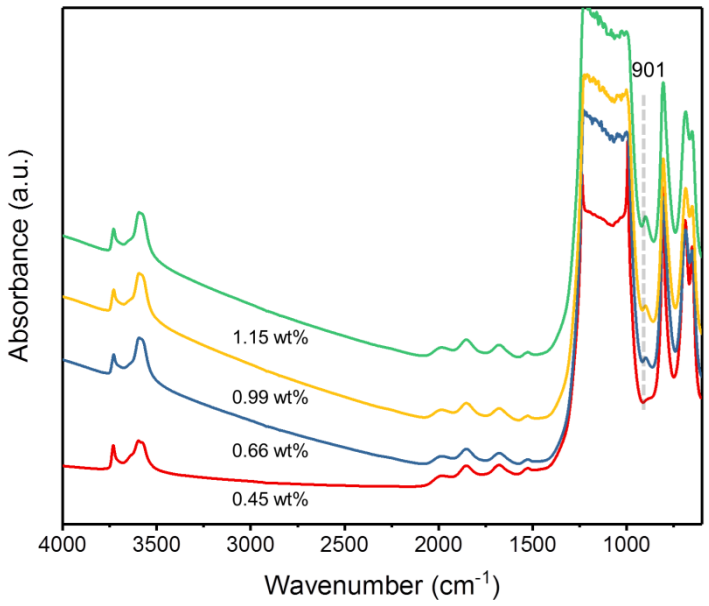

Figure 4.7. Transmission IR spectra of Fe-CHA with various Fe-loadings at 400 ^{o}C after flowing 40 mL min^{-1} dry air for 30 min.

FT-IR NO adsorption was conducted at -160 ^{o}C on Fe-CHA by flowing 1000 ppm NO/N_2 for 50 minutes. The IR peak for Fe^{2+}(NO) appeared at 1897 cm^{-1} in NO-IR spectrum at 20 minutes NO adsorption (**Figure 4.8**).[220, 222] When NO adsorption of Fe-CHA (1.15 wt%, SAR = 20) reached 30 minutes, other IR features such as NO^{+} and $Fe^{2+}(NO)_3$ emerged at 2176 and 1815 cm^{-1}, respectively.[222] After flowing 1000 ppm NO/N_2 for 50 minutes, the IR peak for Fe^{2+}(NO) gradually decreased and the IR signal for $Fe^{2+}(NO)_3$ enhanced at 1920 and 1815 cm^{-1}, indicating that NO can form trimer on Fe^{2+} than monomer at -160 ^{o}C when increasing NO partial pressure. Although the separation of Fe^{2+}(NO) and $Fe^{2+}(NO)_3$ is challenging for quantification purposes, we selected the NO-IR spectrum when the intensity of Fe^{2+}(NO) signal at 1897 cm^{-1} reached its maximum (**Figure 4.9a**). It should be noted that even the chosen NO-IR spectra with the maximum intensity at 1897 cm^{-1} for Fe-CHA already contained some of the IR feature for $Fe^{2+}(NO)_3$ at 1815 cm^{-1}, which made the calculated Fe^{2+}(NO) peak area to Fe-loading off the linearity (**Figure 4.9b**). In addition, based on previous literature, there were two distinct

IR peaks reported for Fe^{2+}(NO) species: Fe^{2+} located at d6r and 8r would show IR peaks at 1884 and 1899 cm^{-1}, respectively.[222] In our case, the deconvoluted NO-IR of Fe-CHA did show both of the 1884 and 1899 cm^{-1} peaks (**Figure S4.3**), indicating that both d6r and 8r accommodate Fe^{2+} species. Although a DFT study predicted the IR peak positions for Fe^{2+}(NO), $Fe^{2+}(NO)_2$, and $Fe^{2+}(NO)_3$, the discrepancy of the IR peak assignments were off by ~50 cm^{-1} compared to our experimental results.[223]

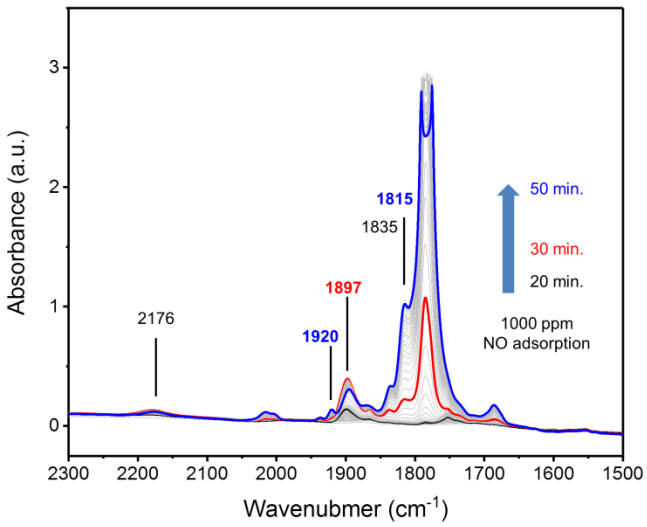

Figure 4.8. Time-resolved NO adsorption IR spectra of Fe-CHA (1.15 wt%, SAR = 20) at -160 ^{o}C after dry air pretreatment at 400 ^{o}C.

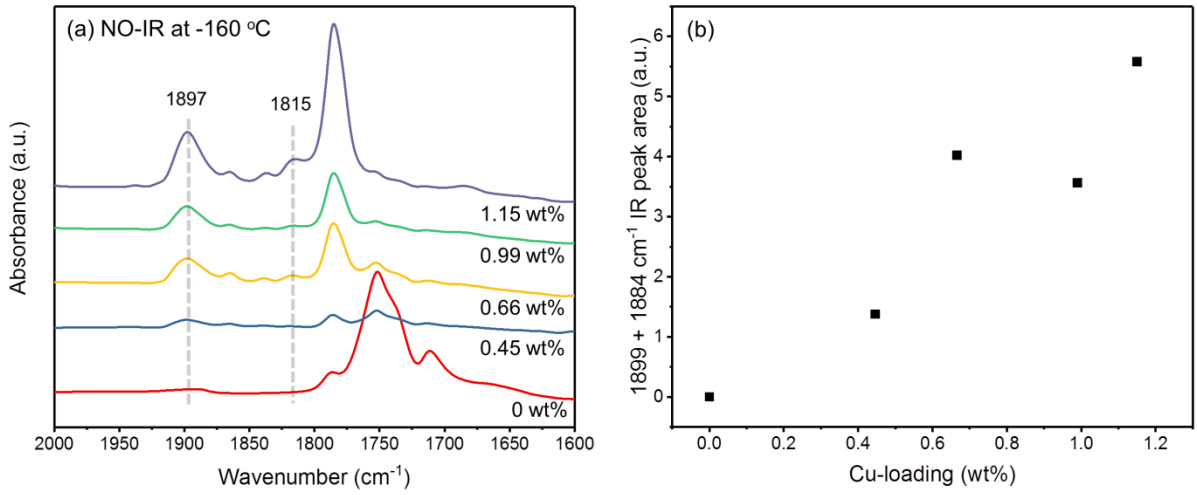

Figure 4.9. (a) NO adsorption IR of Fe-CHA (SAR = 20) with various Fe-loadings at -160 ^{o}C after dry air pretreatment at 400 ^{o}C. (b) Fe^{2+}(NO) IR peak area at 1899 and 1884 cm^{-1} as a function of the corresponding Fe-loading in Fe-CHA.

In order to avoid the NO trimer formation on Fe^{2+} species causing quantification issues, another probe molecule, CO, was applied to detect and quantify Fe^{2+} species in Fe-CHA. In CO-IR adsorption experiments, 5% CO/He was dosed into the IR cell until the pressure was equilibrated at 5 Torr. As shown in **Figure 4.10a**, the first IR peak occurred at 2196 cm^{-1}, which is attributed to Fe^{2+}(CO) species at d6r. Another IR signal appeared later at 2175 cm^{-1}, which correspond to CO adsorbed on Brønsted acid sites (H^{+}(CO)) in Fe-CHA.[222] The IR feature for gas phase CO emerged at 2139 cm^{-1} when the pressure reached 5 Torr.[222] Yet, the IR peak at 2207 cm^{-1} assigned for Fe^{2+}(CO) species at 8r was not discovered in our CO-IR spectra, which contradicts the results from the NO-IR experiments above since we did observe the NO-IR peaks at 1899 and 1884 cm^{-1} corresponding to Fe^{2+} species at 8r and d6r, respectively. It was not clear at the time why there was a difference between NO-IR and CO-IR results for the Fe^{2+} location in CHA. Due to the lack of CO and NO-IR literature on Fe-CHA, there is still room to improve the IR signal assignments for the different Fe^{2+} species. After equilibrating the pressure at 5 Torr of 5% CO/He, the IR cell was then evacuated using a turbo pump until the pressure

reached < $1x10^{-5}$ Torr, throughout which IR spectra were being collected (**Figure 4.10b**). The contribution of gas phase CO IR signal disappeared when evacuating the IR cell for 5 minutes, whereas the intensity of the IR feature for H^+(CO) gradually decreased and finally fully desorbed after evacuating the IR cell for 25 minutes. The CO adsorbed on Fe^{2+} species IR signal at 2196 cm^{-1} stayed even after 30 minutes of evacuation, suggesting CO adsorbed strongly on Fe^{2+} species compared to Brønsted acid sites. However, after all CO desorbed from Brønsted acid sites, the IR peak for Fe^{2+}(CO) at 2196 cm^{-1} started decreasing, showing the importance of performing CO-IR at -160 ^oC to enhance CO chemisorption on Fe-CHA. As a result, the CO-IR spectra for Fe^{2+} quantification purposes were chosen when the intensity of IR signal for Fe^{2+}(CO) still showed its maximum, but the intensity of the IR peak for H^+(CO) reached close to minimum (**Figure 4.11a**). Based on previous CO-IR study, the adsorbed CO on non-exchanged Fe species, FeO_x, showed IR features at 2177, 2148, and 2129 cm^{-1} which were not observed in our CO-IR spectra.[222] Therefore, assuming there were no formation of non-exchanged Fe species, the correlation between the Fe-loading from ICP-OES and the IR peak areas of Fe^{2+}(CO) in Fe-CHA can be further applied for exchanged Fe^{2+} quantification in Fe-CHA (**Figure 4.11b**).

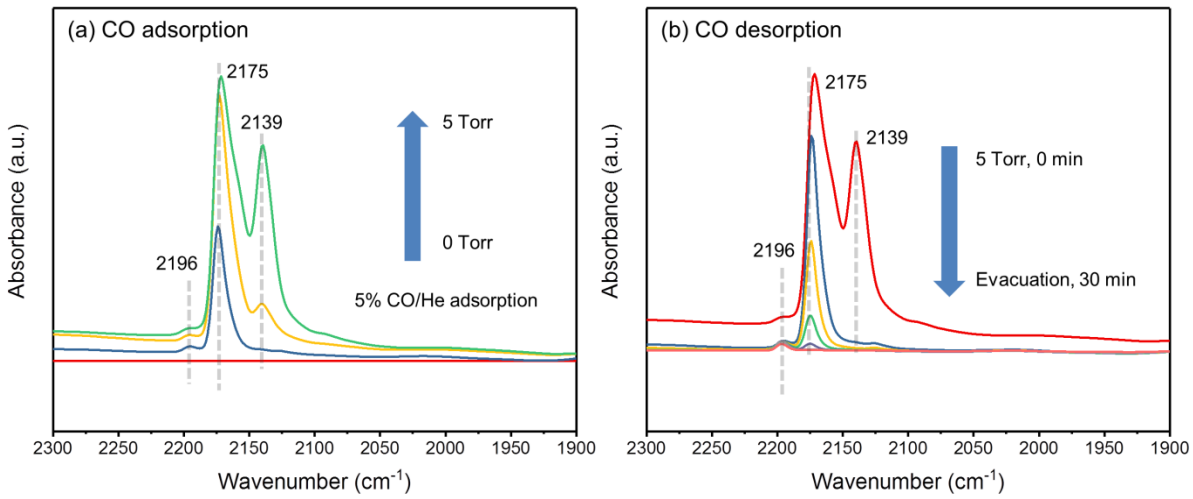

Figure 4.10. Time resolved CO-IR spectra of Fe-CHA (0.99 wt%, SAR = 20) at -160 ^{o}C performing (a) CO adsorption and (b) CO desorption (5 min interval for each spectrum).

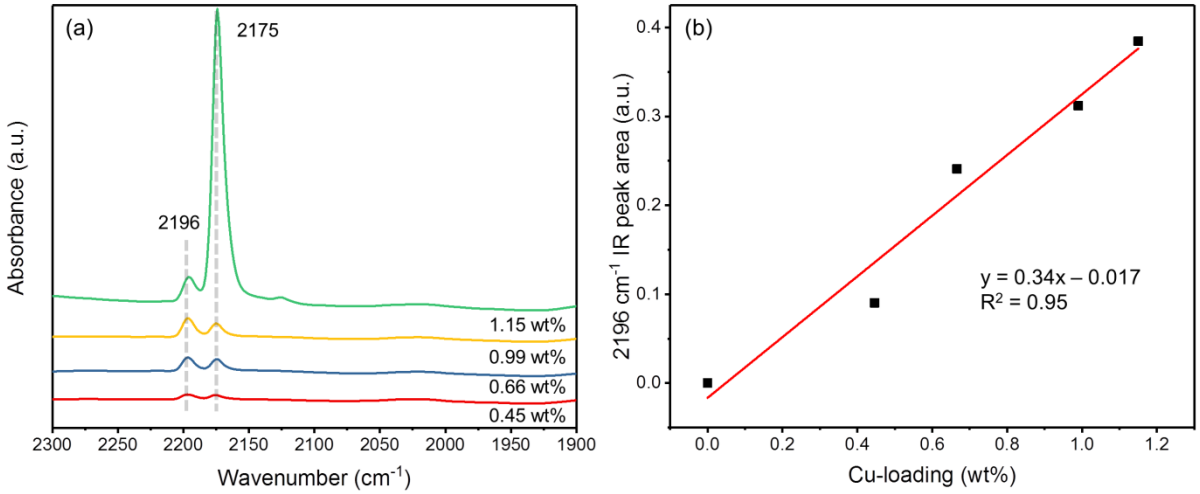

Figure 4.11. (a) CO adsorption IR of Fe-CHA (SAR = 20) with various Fe-loadings at -160 ^{o}C after dry air pretreatment at 400 ^{o}C. (b) Fe^{2+}(CO) IR peak area at 2196 cm^{-1} as a function of the corresponding Fe-loading in Fe-CHA.

4.3 Conclusion

We successfully extended the NO-IR method for the detection and quantification of Cu species to another Cu-zeolite, Cu-ZSM-5. The results showed that NO-IR can be useful not only for estimating the amount of exchanged Cu species, but also the out of

framework Cu species, CuO_x. This technique can benefit catalyst development in both methane to methanol and syngas to dimethyl ether reactions, the active sites of which are exchanged Cu and non-exchanged Cu species, respectively. Not only can the NO-IR be extended to other Cu-zeolites, a different transition metal ion-exchanged CHA, Fe-CHA, was also tested. In the case of Fe-CHA, NO adsorption on Fe^{2+} species at -160 ^oC tends to form NO trimers, causing difficulties to quantify the exchanged Fe species, because $Fe^{2+}(NO)$ and $Fe^{2+}(NO)_3$ coexisted in the IR spectra. By using CO as a probe for Fe-CHA in the IR spectroscopy, $Fe^{2+}(CO)$ and $H^+(CO)$ showed IR peaks at 2196 and 2175 cm^{-1}, respectively. The integrated peak areas of $Fe^{2+}(CO)$ correspond linearly to the Fe-loadings in Fe-CHA, allowing for the establishment of a calibration curve for Fe^{2+} species.

4.4 Experimental Details

Cu-ZSM-5 synthesis

Parent ZSM-5 (SAR = 30) zeolite was purchased from Zeolyst. To synthesize the Cu-ZSM-5 samples, 150 mg of parent ZSM-5 powder is well-dispersed in 10 mL of $Cu(NO_3)_2$ solution (18.2 MΩ water) at concentrations of 0.5-20 mM, stirred at 300 rpm for 4 hours at room temperature, and maintained at a pH of 4.8-5.0 by dropwise addition of 0.1 M $NH_4OH_{(aq)}$. The various Cu-ZSM-5 samples are then centrifuged and washed 3 times with DI water to remove excess Cu ions on the samples. The washed Cu-ZSM-5 samples are dried in an oven at 110 ^oC for 24 hours. The dry Cu-ZSM-5 samples are then calcined in a muffle furnace under air flow at 500 ^oC for 4 hours with a ramp rate of 1 ^oC/min. The exact Cu-loading in the Cu-ZSM-5 samples was measured by inductively coupled plasma optical emission spectroscopy (ICP-OES) analysis.

Fe-CHA synthesis

Parent CHA (SAR = 20) zeolite was provided by BASF. To synthesize the Fe-CHA samples, 200 mg of parent CHA powder is well-dispersed in 20 mL 18.2 MΩ water, adjusted at a pH of 3.0 by dropwise addition of 0.1 M $HNO_{3(aq)}$,and stirred at 300 rpm to 80 ^{o}C under N_2 condition. After the solution reached 80 ^{o}C, the desired amount of $Fe(SO_4)\cdot 7H_2O$ was added into well-dispersed CHA solution and stirred at 300 rpm, 80 ^{o}C for 1 hour under N_2 condition. The various Fe-CHA samples are then centrifuged and washed 3 times with DI water to remove excess Fe ions on the samples. The washed Fe-CHA samples are dried in an oven at 120 ^{o}C for 24 hours. The dry Fe-CHA samples are then calcined in a muffle furnace under air flow at 550 ^{o}C for 5 hours with a ramp rate of 2 ^{o}C/min. The exact Fe-loading in the CHA samples was measured by inductively coupled plasma optical emission spectroscopy (ICP-OES) analysis.

NO adsorption FT-IR spectroscopy

For FT-IR analysis, 5 mg Cu-ZSM-5 or Fe-CHA sample is pressed into a self-supported thin wafer that is placed in a homemade *in-situ* transmission IR flow cell which can be heated to 400 ^{o}C and cooled to -170 ^{o}C. All FT-IR measurements were performed in a Bruker Vertex 70 spectrometer equipped with a liquid nitrogen cooled Mercury-Cadmium-Telluride (MCT) detector. Typically, 128 scans with a resolution of 4 cm^{-1} were averaged to give one spectrum. Prior to a low temperature NO adsorption measurement, the cell is heated at 5 ^{o}C/min to 400 ^{o}C and held for 30 min under 40 mL/min dry air or 4 % H_2/N_2 to have oxidative and reductive pretreatments. After oxidative pretreatment, the cell is cooled down to 200 ^{o}C with flowing dry air to avoid auto-reduction, and then evacuated by a turbo pump (pressure < $1x10^{-5}$ Torr). In contrast, after the reductive pretreatment, the cell is then evacuated by a turbo pump (pressure < $1x10^{-5}$ Torr) at 400

^{o}C. To begin low temperature NO adsorption, the cell is first cooled to room temperature before it is further cooled to -160 ^{o}C by liquid nitrogen.

A background FT-IR spectrum is collected at -160 ^{o}C under vacuum before feeding NO. 1000 ppm NO diluted in N_2 is then fed into the cell for 40 min, and the spectra – referred to as NO adsorption FT-IR spectra – are collected at 1 min intervals. All adsorption FT-IR spectra are collected under low temperature (-160 ^{o}C) conditions maintained by constantly adding liquid nitrogen to the transmission IR cell. To compare and quantify the Cu^{2+} IR band integrals in different Cu-ZSM-5, all IR spectra are first normalized by using Si-O overtone with the area, 8.846, from 1934 to 1734 cm^{-1} for each Cu-ZSM-5 IR spectrum at 400 ^{o}C under oxidative or reductive pretreatment before cooling down and feeding NO to serve as an internal standard, whereas Fe-CHA IR spectra are normalized by Si-O overtone with the area, 6.588, from 1931 to 1768 cm^{-1} as internal standard.

CO adsorption FT-IR spectroscopy

A background FT-IR spectrum of Fe-CHA after dry air pretreatment is collected at -160 ^{o}C under vacuum before CO adsorption. 5% CO/H_2 was then dosed into IR cell and equilibrated at 5 Torr for 5 min or until no change for the CO adsorption IR spectrum. After CO adsorption at 5 Torr, the IR cell was evacuated by a turbo pump until the pressure < $1x10^{-5}$ Torr, while collecting CO desorption IR spectra at 1 min intervals. The internal standard for Fe^{2+} quantification of Fe^{2+}(CO) IR peak was the Si-O overtone from 1931 to 1768 cm^{-1} with the area, 6.588, at 400 ^{o}C under dry air condition.

Chapter 5: Conclusions and Perspectives

5.1 Conclusions

In chapter 2, we showcase that *operando* MES-DRIFTS-MS is a powerful technique to study a catalytic reactions with multiple steps. The hypothesized reaction pathway of ethanol to *n*-butanol via hydroxyapatite (HAP) was evidenced by modulating different reactive intermediates and also showed the reason why hydrogenation on C=C bond to form *n*-butanol is unlikely. The possible active on HAP surface were Ca^{2+}/OH^- and POH/OH^- as acid-base pairs which are responsible for aldol condensation and direct hydrogen transfer, respectively.

In chapter 3, we developed a low temperature IR methodology that can characterize the copper speciation and exchanged copper quantities in a commercial NO_x abatement catalyst, Cu-CHA. By using nitric oxide (NO) as a probe molecule in low temperature (-160 ^oC) IR spectroscopy, the NO adsorbed on different copper species showed distinct IR features for Z_1CuOH, Cu dimers, and Z_2Cu which can establish a structure-reactivity correlation to benefit the catalyst development. In addition, we were able to quantify the exchanged copper species in Cu-CHA *via* low temperature NO-IR, which the information cannot obtain from the conventional elemental analysis, such as ICP-OES. The industrial-relevant washcoat Cu-CHA catalysts were also tested and showed the consistent estimated quantities of exchanged copper species with the low temperature NO-IR technology.

In chapter 4, with the success of the NO-IR method development for Cu-CHA, we further extended the characterized material to Cu-ZSM-5 and Fe-CHA. The outcome of NO-IR for Cu-ZSM-5 showed distinct IR peak for exchanged copper species at 1914 cm^{-1} and the calibration curve for Cu^{2+} species was provided. In the case of Fe-CHA, the NO-

IR was not efficient due to the formation of NO monomer and trimer on copper species, causing complexity in the IR spectra. Carbon monoxide (CO) was then applied as an alternative probe molecule. The results of CO-IR for Fe-CHA showed clearer IR peaks for Fe^{2+}(CO) than in NO-IR and the calibration curved for Fe^{2+} by CO-IR was then established.

5.2 Perspectives

Our achievements in this thesis establish two fundamental toolboxes to study heterogeneous catalysis: *operando* IR spectroscopy to elucidate the reaction profile at the molecular level, and site-sensitive IR spectroscopy to probe the metal sites in industrial-relevant catalysts Building on these toolboxes, we envision four potential research directions. Firstly, the sensitivity of *operando* spectroscopy can be promoted by optimizing the configuration of the DRIFTS cell, making it possible to reveal more molecular information. The main characteristic of the *operando* spectroscopy with modulation excitation is the introduction of a rapid perturbation in the system. A shorter exchange time for concentration modulation during perturbation can allow better control of the modulation excitation. To be more specific, we are aware of delay times at around 25 sec between the *excitation* and the spectra during the modulation excitation. The type of spectral delay can be attributed to the large void space in the DRIFTS cell. In order to enhance the exchange time for concentration modulation, a design for a small dead volume DRIFTS cell is required. Furthermore, the design of the DRIFTS cell can be expanded to hold a high pressure (> 30 bar) and high temperature (> 200 ^{o}C). Optimizing the ambient reaction cell into a high-pressure/high-temperature reaction cell with a reduced dead volume can impact a wide range of heterogeneous catalytic systems.

Secondly, we envision that the optimized toolbox of *operando* IR spectroscopy can reveal reaction profiles that are challenging to study in working conditions, such as CO_2 hydrogenations demand high reaction temperature (> 250 °C) and pressure (> 25 bar).[6] The prototype of the DRIFTS micro-reactor design has been shown the capability for investigating CO oxidation over gold catalyst.[224] With the emergence of the concept of a carbon-neutral environment, CO_2 can be hydrogenated to methanol or olefins as an alternative pathway for important chemical feedstock. However, the thermodynamics of CO_2 hydrogenation favors reverse water gas shift (RWGS) than methanol under ambient pressure. In our preliminary MES-DRIFTS results of CO_2 hydrogenation on a Cu-Ga/SiO_2 catalyst (**Figure S5.1**) at ambient pressure, the reaction tends to mostly undergo RWGS to form CO instead of methoxy species. In addition, the observed formate species at 3003 and 1594 cm^{-1} indicated that some insights of the catalytic reaction can be revealed. With the newly designed high-pressure DRIFTS cell, the newer generation of CO_2 to methanol catalysts can be studied by *operando* DRIFTS-MS. Furthermore, the same DRIFTS cell design can also apply to other characterization techniques such as Raman and UV-vis spectroscopy to add as a complementary method to investigate the catalysts under working conditions.

Besides of heterogeneous catalytic reactions in the gas phase, the liquid phase heterogeneously catalytic reaction is also an important part in industrial processes such as propylene epoxidation. Unlike the catalytic reactions in the gas phase, solvent usually plays a role in liquid phase reactions because of the competitive adsorption with reactants, and this phenomenon is especially more pronounced in the case of (micro-) porous catalysts where the composition inside the pores can be very different from the bulk due to size exclusion and confinement effects.[225] Moreover, such systems are prone to diffusion limitations as the dimensions of the molecules are of the same order-of-

magnitude as the pore size. In that case, it is likely that the solvent also strongly controls the rate of mass-transfer. A notorious example of a microporous catalytic system with pronounced solvent effects that are not well understood is the TS-1 catalyzed epoxidation of propylene with H_2O_2,[226] the so-called HPPO process which was co-developed by BASF and Dow Chemical. For this system, methanol was experimentally found to be the optimal solvent. Interestingly, acetonitrile – a solvent with a very similar dielectric constant – performs significantly worse than methanol. Until today, the H_2O_2/solvent ratio and their influence near the active titanium sites inside the micro-pores are still under debated,[227-229] as well as the influence of competitive adsorption. Given the fact that methanol reacts with the epoxide product in downstream rectification columns, using a less nucleophilic solvent like acetonitrile would offer significant practical advantages, not in the least as also the vaporization enthalpy of acetonitrile is lower than that of methanol and could hence reduce energy consumption in the thermal separation. With the MES-ATR-IR technique, we will be able to discern the solvent effects and the nature of the Ti active site under reaction conditions. The results from MES-ATR-IR provide the potential to differentiate the contribution from bulk and the solvents in the pore as well as the interaction with H_2O_2. In addition, after phase-sensitive detection (PSD), the consecutive signals from intermediates and adsorbed species can be observed to compare with the working hypothesis of TS-1 catalyzed HPPO process.

In chapters 3 and 4, we show that low-temperature NO-IR and CO-IR are powerful tools to investigate and quantify the nature of the copper and iron ion in CHA and ZSM-5 zeolites. However, there is still some unknown speciation of Fe species in Fe-CHA which is a better deNO_x abatement catalyst in N_2O selectivity. The controlled Al distribution Fe-CHA such as mostly paired and isolated Al configuration with similar Si/Al ratio need to be synthesized. By using low-temperature CO-IR, the differences of the CO adsorbed IR

features between mostly paired and isolated Al Fe-CHA could shed light on the speciation of iron ion in the CHA cages. In addition, X-ray photoelectron spectroscopy (XPS) and X-ray diffraction (XRD) can provide insights of the oxidation states of iron or possibly its location in cages and the information for FeO_x species. Ultimately, the low temperature NO and CO-IR can behave as a facile and reliable technique for identifying and quantifying the metal ion in various ion-exchange zeolites.

Appendices

Chapter 2: Insights into Ethanol Coupling over Hydroxyapatite Using Modulation Excitation *Operando* Infrared Spectroscopy

Table S2.1. Chosen m/z signals and some IR vibrational frequencies[a] for the most important chemicals.

Molecule	m/z	υ(C-H) cm^{-1}	υ(C=O) cm^{-1}	υ(C=C) cm^{-1}	υ(O-H) cm^{-1}
Ethanol	46	2977, 2903	-	-	3666
Acetaldehyde	44	2820, 2733, 2705	1758	-	-
Crotonladehyde	70	2995, 2936, 2813, 2730	1720	1645	-
Crotyl alcohol	57	3026, 2939, 2879	-	1676	3661
Butanal	72	2971, 2896, 2807, 2712	1748	-	-
n-butanol	56	2964, 2941, 2890	-	-	3669
1,3-butadiene[b]	54	3111, 3090		1830, 1813	

[a] Gas-phase infrared reference spectra from Figure S2.3

[b] 1,3-butadiene infrared reference spectrum from NIST Chemistry WebBook.

Table S2.2. Chosen m/z signals and some IR vibrational frequencies[c] for the most important chemicals adsorbed HAP.

Molecule	m/z	υ(C-H) cm^{-1}
Ethanol	46	2977, 2933, 2903
Acetaldehyde	44	2975, 2921, 2757
Crotonladehyde	70	3004, 2923, 2855, 2764
Crotyl alcohol	57	2950, 2927, 2894
Butanal	72	2967, 2940, 2879
n-butanol	56	2960, 2940, 2881

[c] Adsorbed intermediate molecules infrared spectra from Figure S2.4

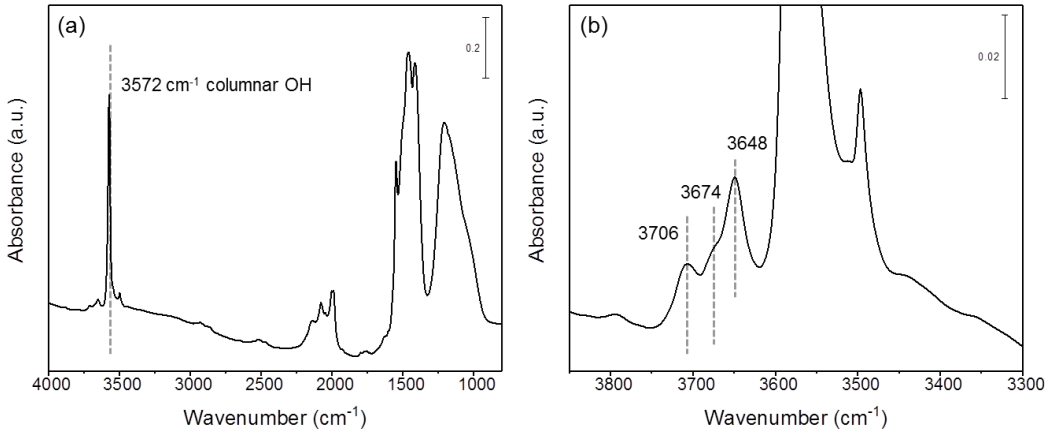

Figure S2.1. Transmission FT-IR spectrum for self-supported wafer for hydroxyapatite (HAP) at room temperature after calcination in 600 ^{o}C for 2 hrs, (a) full range of spectrum, (b) zoom in from (a) for clarity of POH features.

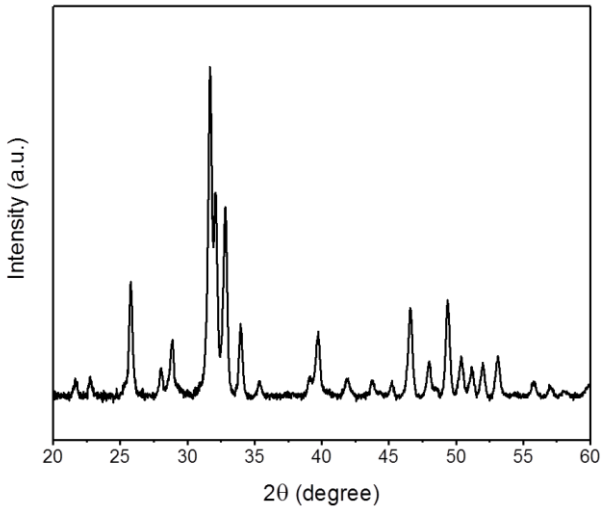

Figure S2.2. X-ray diffraction pattern for hydroxyapatite (HAP) under ambient conditions on a Bruker D8 advance diffractometer with Cu Kα radiation (λ = 1.5406 Å).

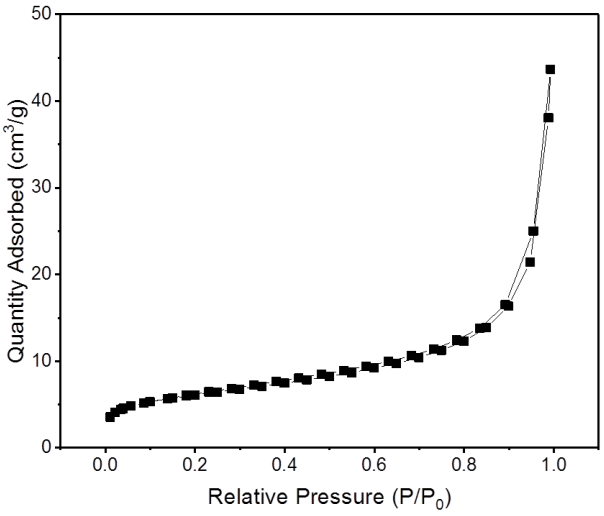

Figure S2.3. N_2 adsorption and desorption isotherm were performed on a Micromeritics 3-flex apparatus. BET surface area: 21 m^2/g

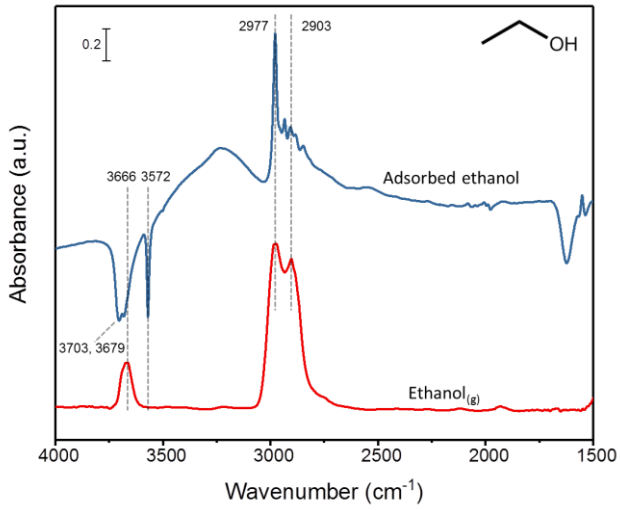

Figure S2.4. Transmission FT-IR spectra for comparison. Hydroxyapatite (HAP) is collected by a self-supported wafer. Gas phase ethanol is record by dosing liquid ethanol into a vacuum transmission cell. Ethanol adsorption IR spectrum is taken after evacuation for the transmission IR cell which doses liquid ethanol into vacuum transmission cell with self-supported HAP wafer and the background of the adsorption spectrum is taken before dosing ethanol. All measurements are operated at room temperature.

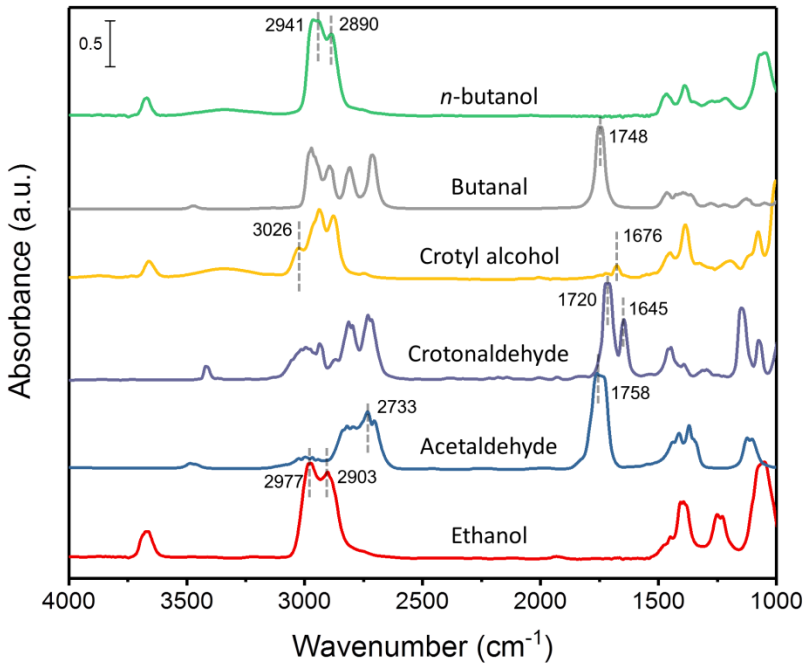

Figure S2.5. Transmission gas phase reference FT-IR spectra for each intermediates, reactant, and product at room temperature. Each gas phase species IR spectrum is collected by dosing liquid chemical into a vacuum transmission cell until the pressure reaches 100 Torr at room temperature.

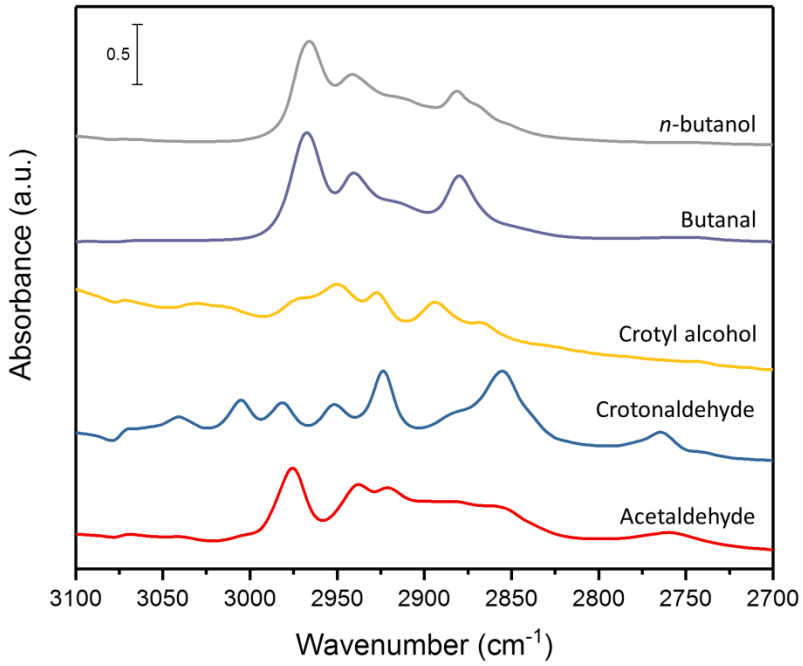

Figure S2.6. Adsorption reference IR spectra are taken after evacuation for the transmission IR cell which doses specific intermediates such as acetaldehyde, crotonaldehyde, crotyl alcohol, butanal and product, n-butanol, into vacuum transmission cell with self-supported HAP wafer and the background of the adsorption spectrum is taken before dosing each species. All measurements are operated at room temperature.

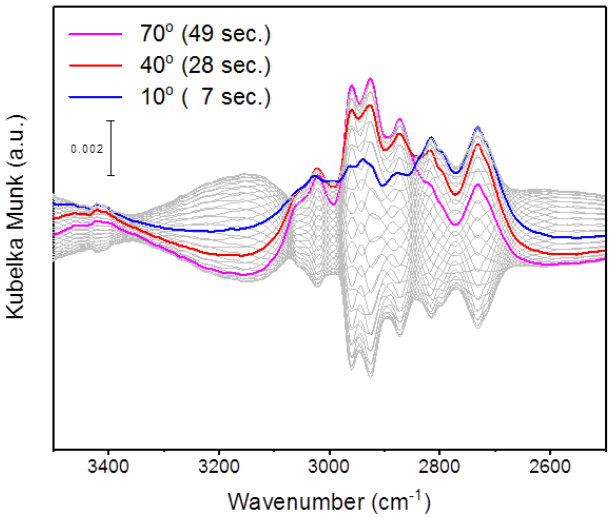

Figure S2.7. Phase-sensitive detection (PSD) DRIFT spectra in C-H region with modulation experiment between ethanol (2.5%)/CA with 3:1 molar mixture in 20 mL min^{-1} Ar as carrier gas and ethanol in Ar flow, the phase-delay at 10^{o} corresponds to acetaldehyde, 40^{o} correlates to crotyl alcohol, and 70^{o} indicates n-butanol

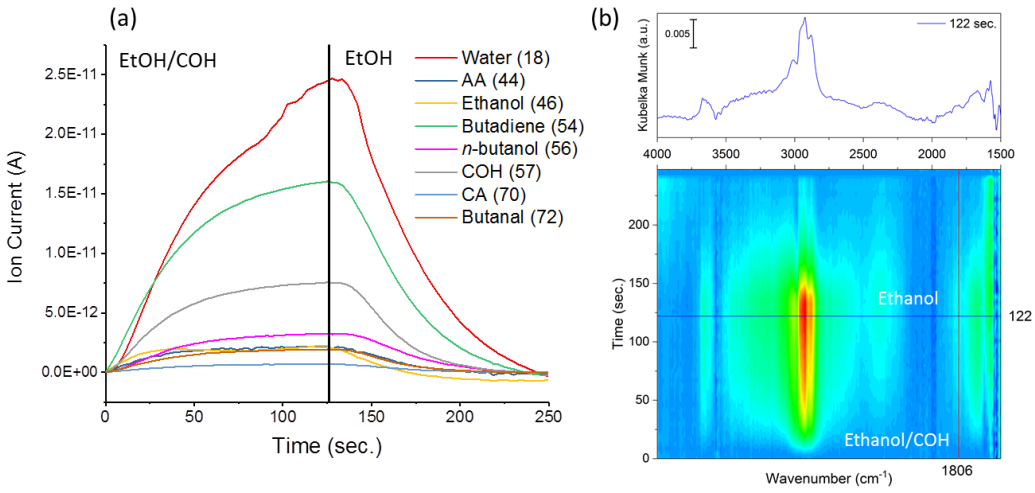

Figure S2.8. Modulation experiment between ethanol (2.5%)/crotyl alcohol with 3:1 molar mixture in 20 mL min^{-1} Ar as carrier gas and ethanol in Ar over 5 mg hydroxyapatite (HAP) at 330 ^{o}C (a) selected m/z signals from mass spectrometry response (b) Time-domain DRIFT spectra and the line at 122 sec. indicates gas channels switch.

Chapter 3: Quantification of Exchanged Copper Species in Cu-Chabazite Zeolite Using Cryogenic Probe Infrared Spectroscopy

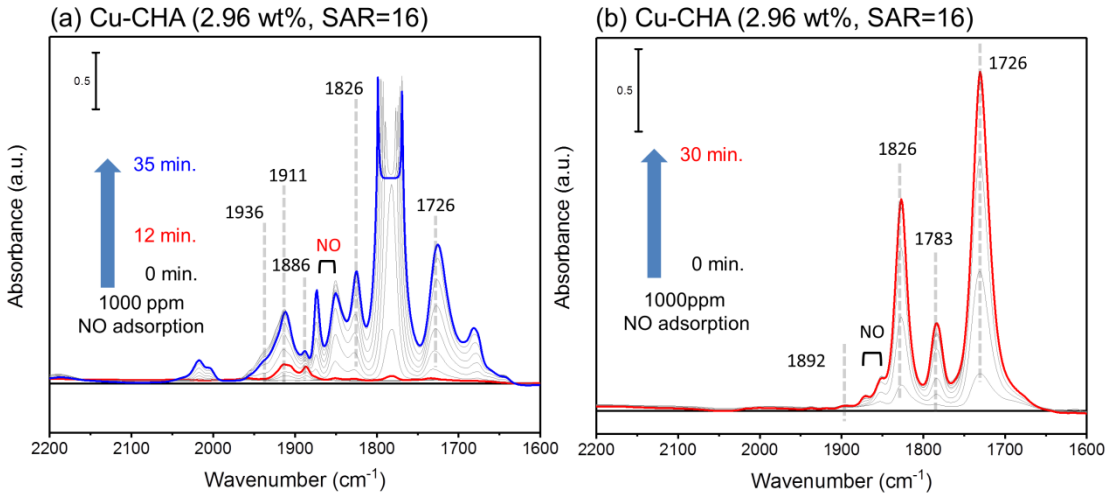

Figure S3.1. Time-resolved 1000 ppm NO/N_2 adsorption IR spectra of Cu-CHA (2.96 wt%, SAR = 16) at -160 ^{o}C and pretreated at 400 ^{o}C with (a) dry air and (b) 4% H_2/N_2 at 40 mL min^{-1}. The split and flat peak shape at 1785 cm^{-1} in (a) is due to the saturation of MCT detector

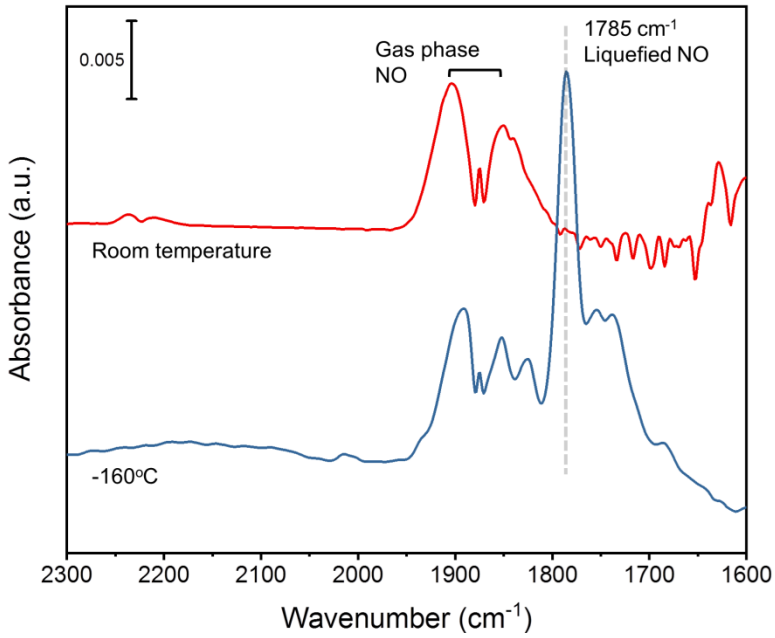

Figure S3.2. Transmission IR spectra of the parent CHA collected at room temperature and -160 ^{o}C while flowing 1000 ppm NO/N_2 at 40 mL min^{-1}.

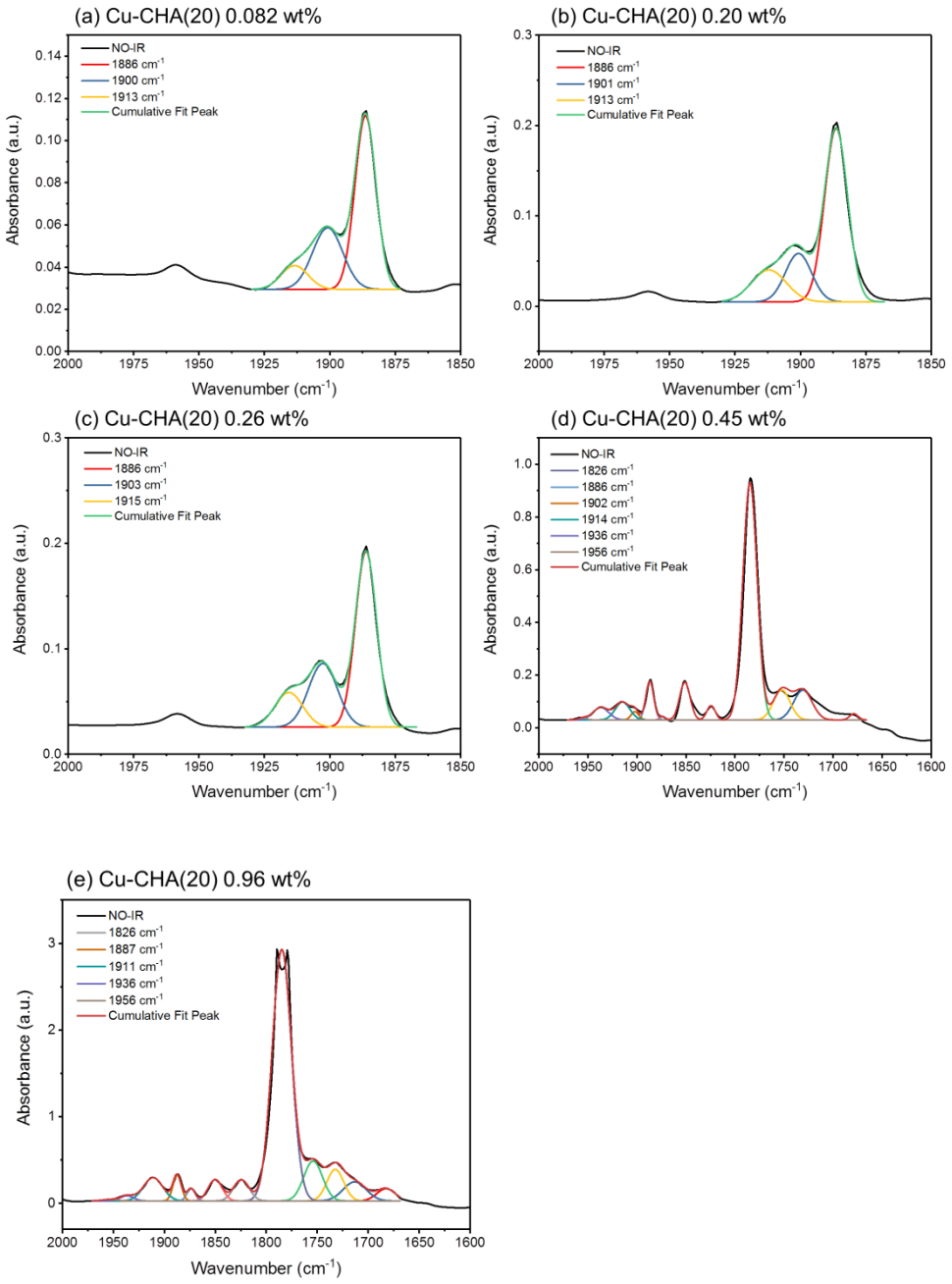

Figure S3.3. Deconvoluted IR peaks for NO adsorption IR spectra of Cu-CHA(20) at -160 ^{o}C after dry air pretreatment at 400 ^{o}C.

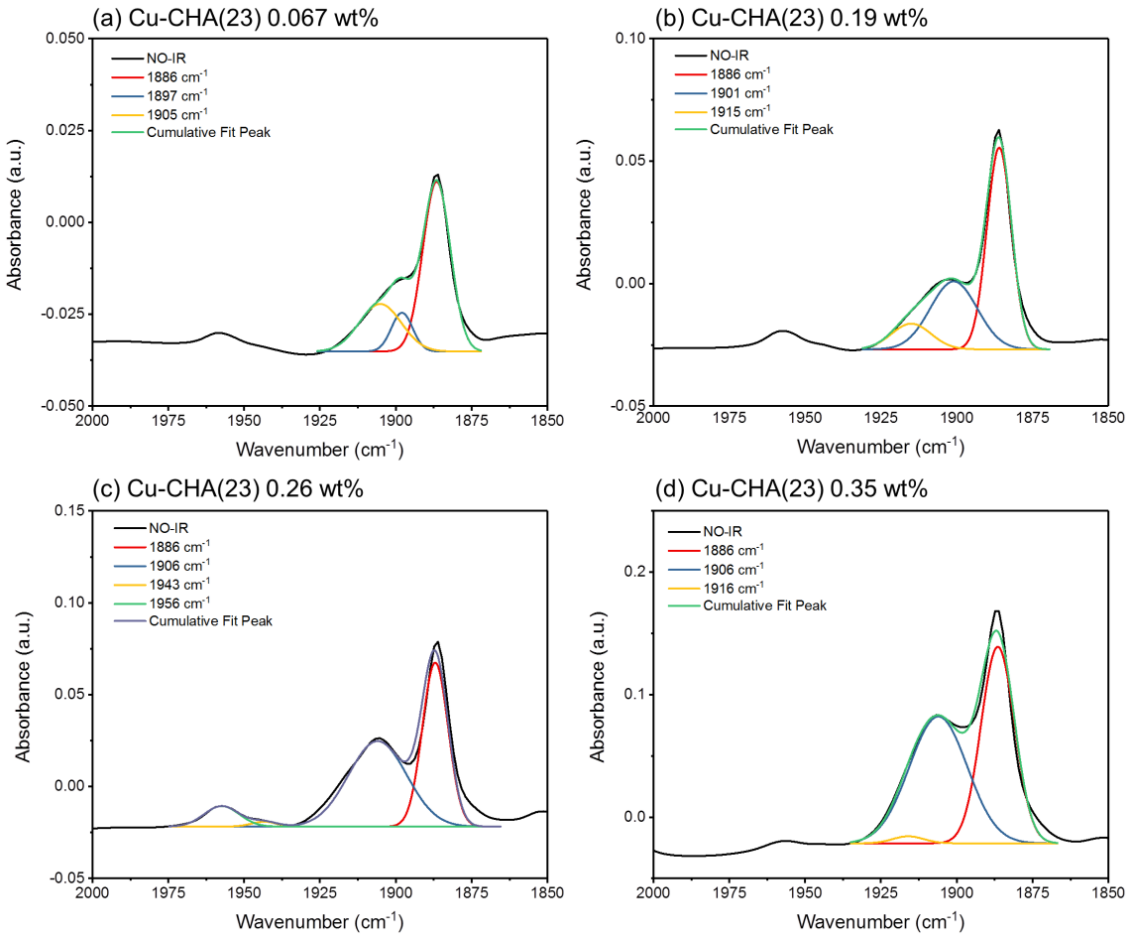

Figure S3.4. Deconvoluted IR peaks for NO adsorption IR spectra of Cu-CHA(23) at -160 ^{o}C after dry air pretreatment at 400 ^{o}C.

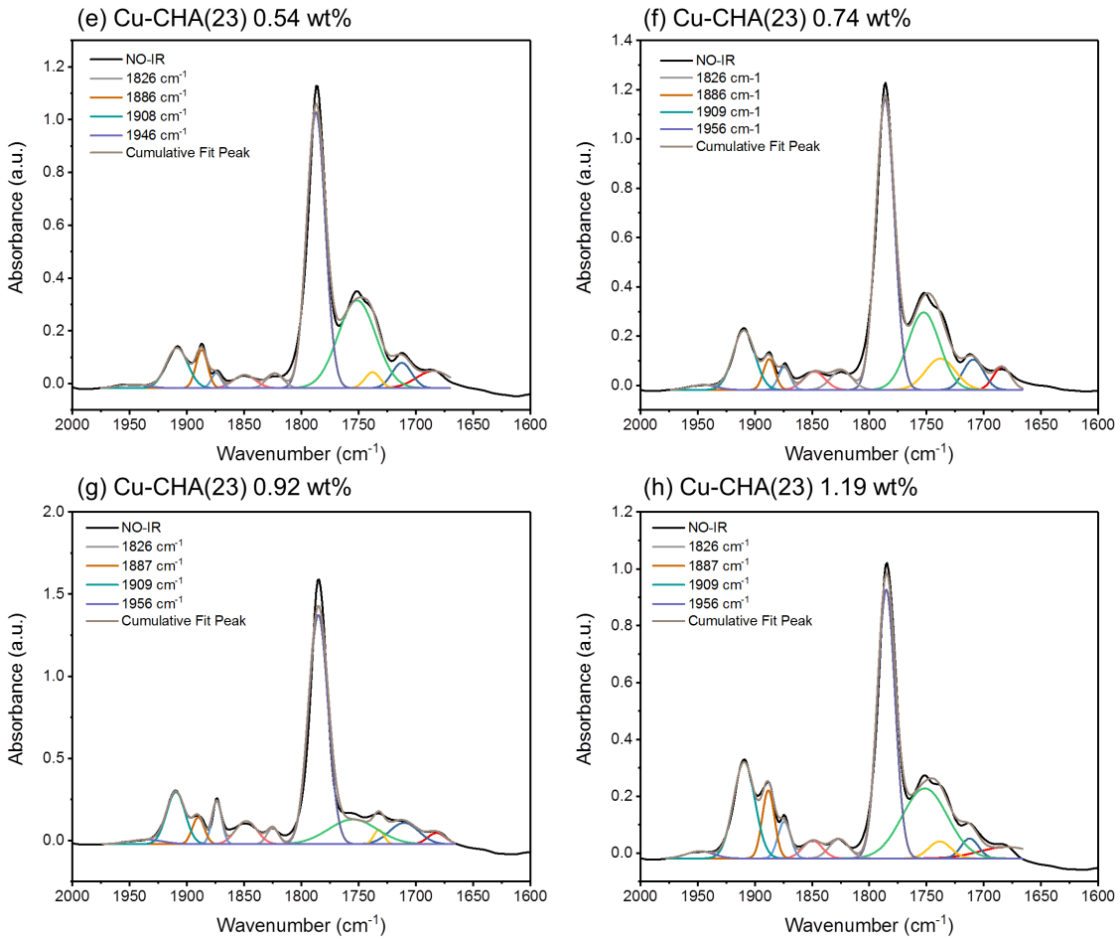

Figure S3.4. Deconvoluted IR peaks for NO adsorption IR spectra of Cu-CHA(23) at -160 ^{o}C after dry air pretreatment at 400 ^{o}C.

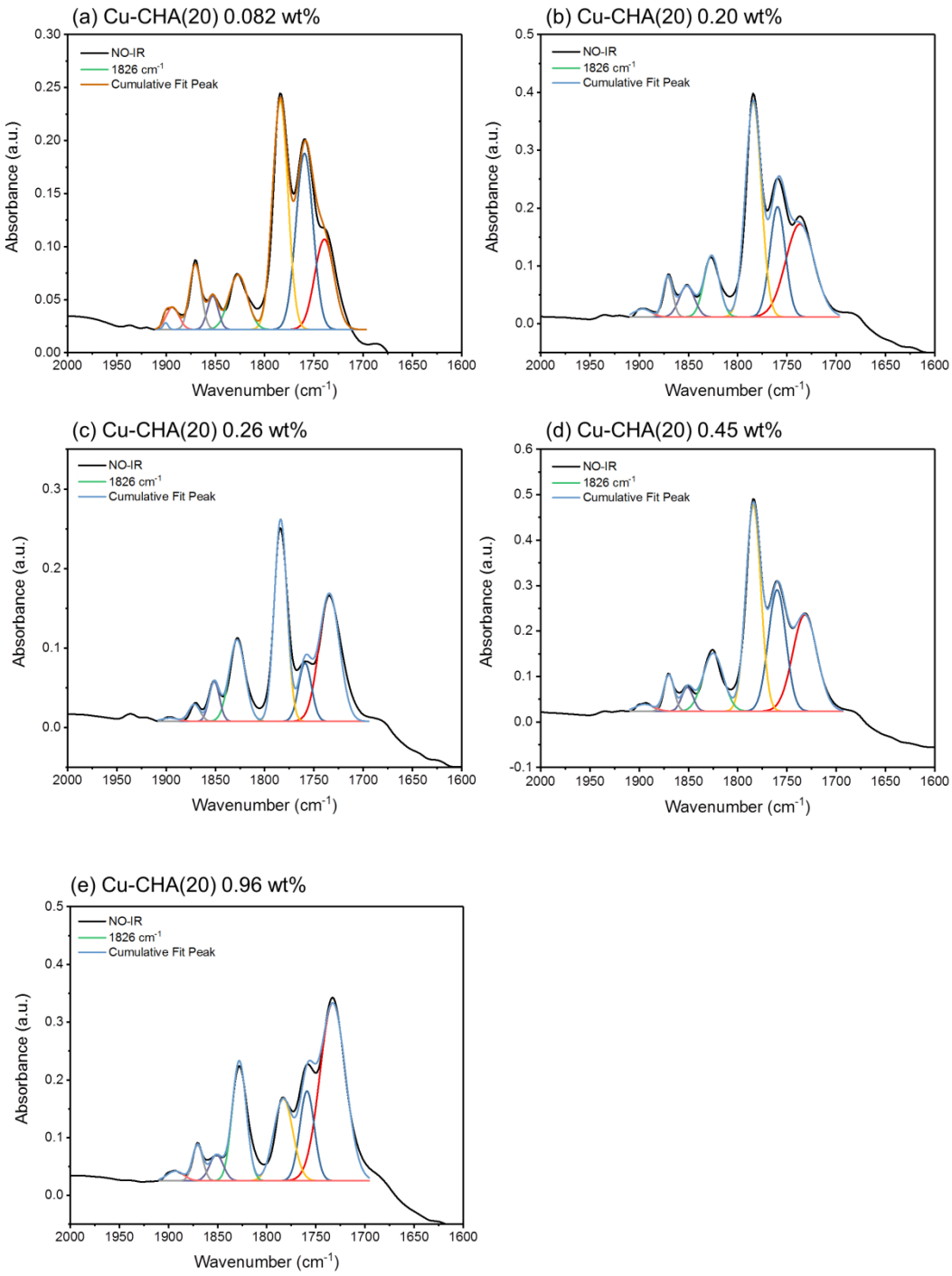

Figure S3.5. Deconvoluted IR peaks for NO adsorption IR spectra of Cu-CHA(20) at -160 ^{o}C after H_2 pretreatment at 400 ^{o}C.

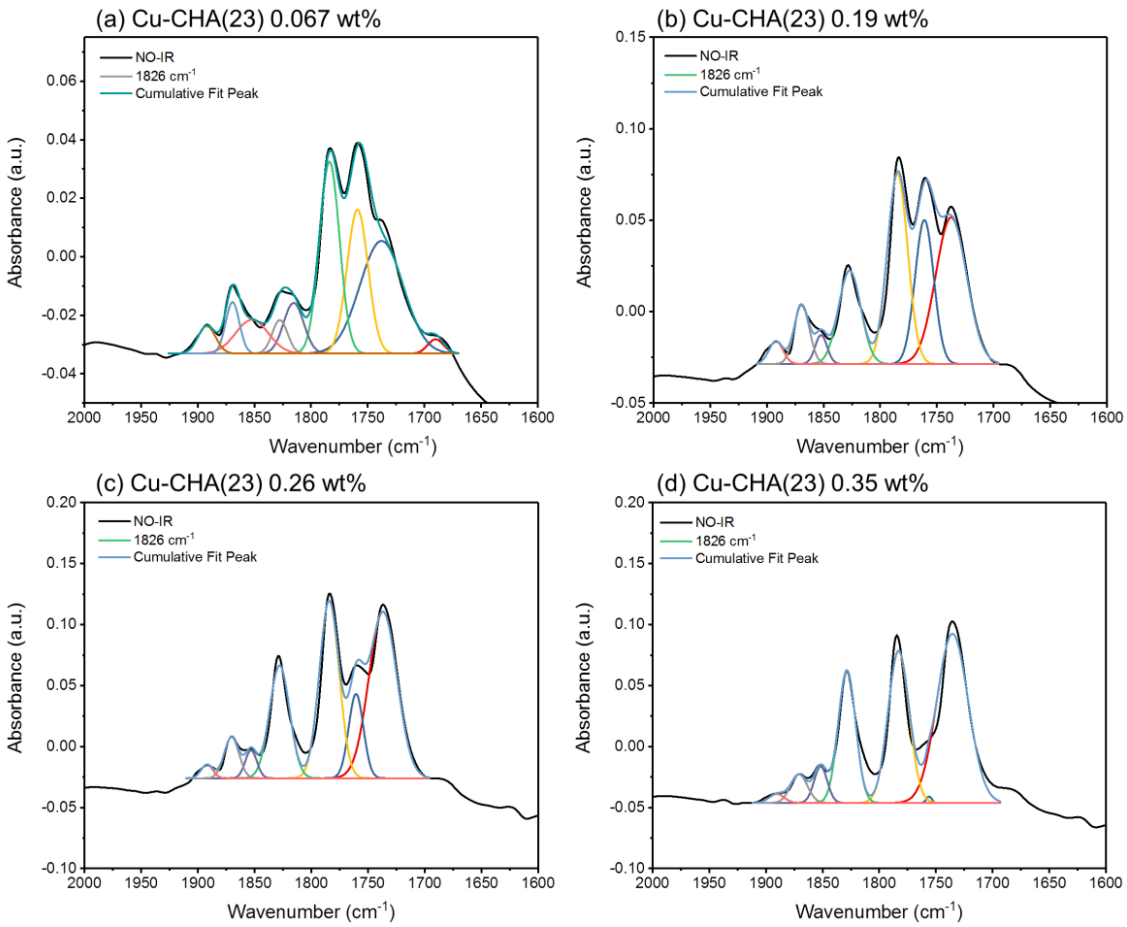

Figure S3.6. Deconvoluted IR peaks for NO adsorption Cu-CHA(23) IR spectra at -160 ^{o}C after H_2 pretreatment at 400 ^{o}C

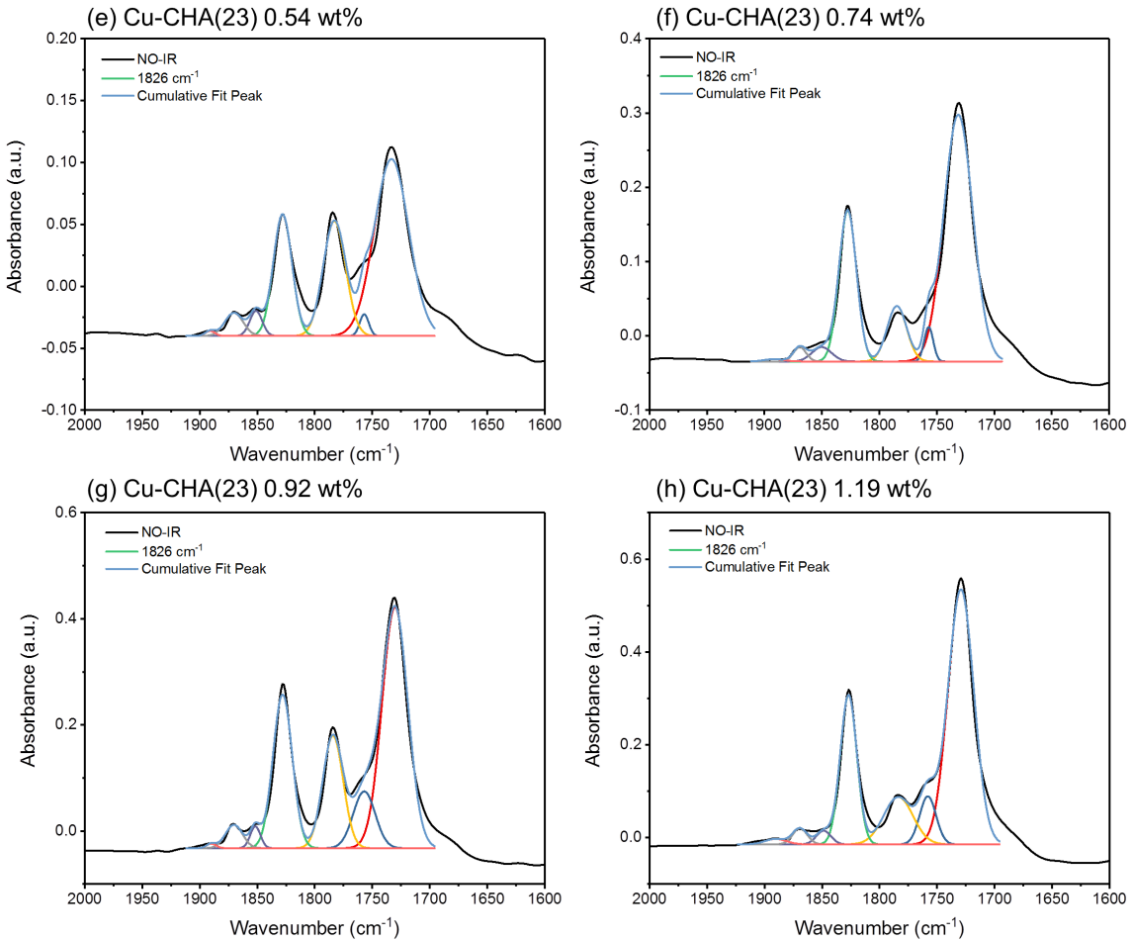

Figure S3.6. Deconvoluted IR peaks for NO adsorption Cu-CHA(23) IR spectra at -160 ^{o}C after H_2 pretreatment at 400 ^{o}C

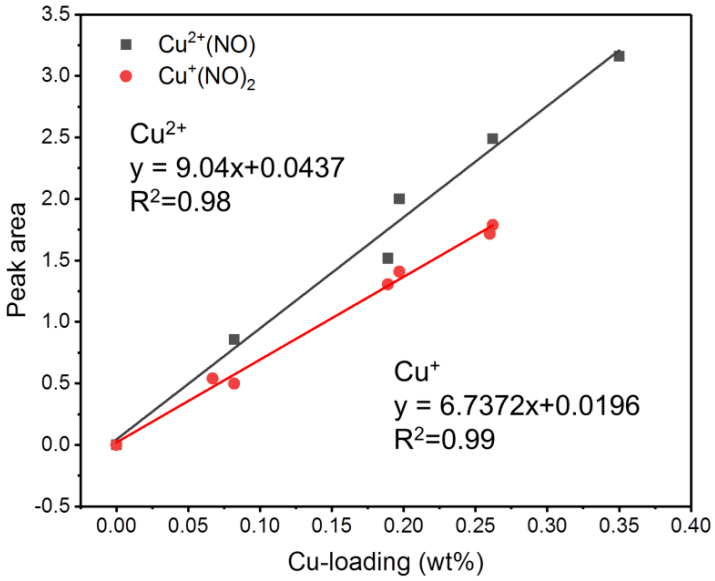

Figure S3.7. Calibration curve for Cu^{2+} and Cu^{+} species from NO-IR at -160 ^{o}C

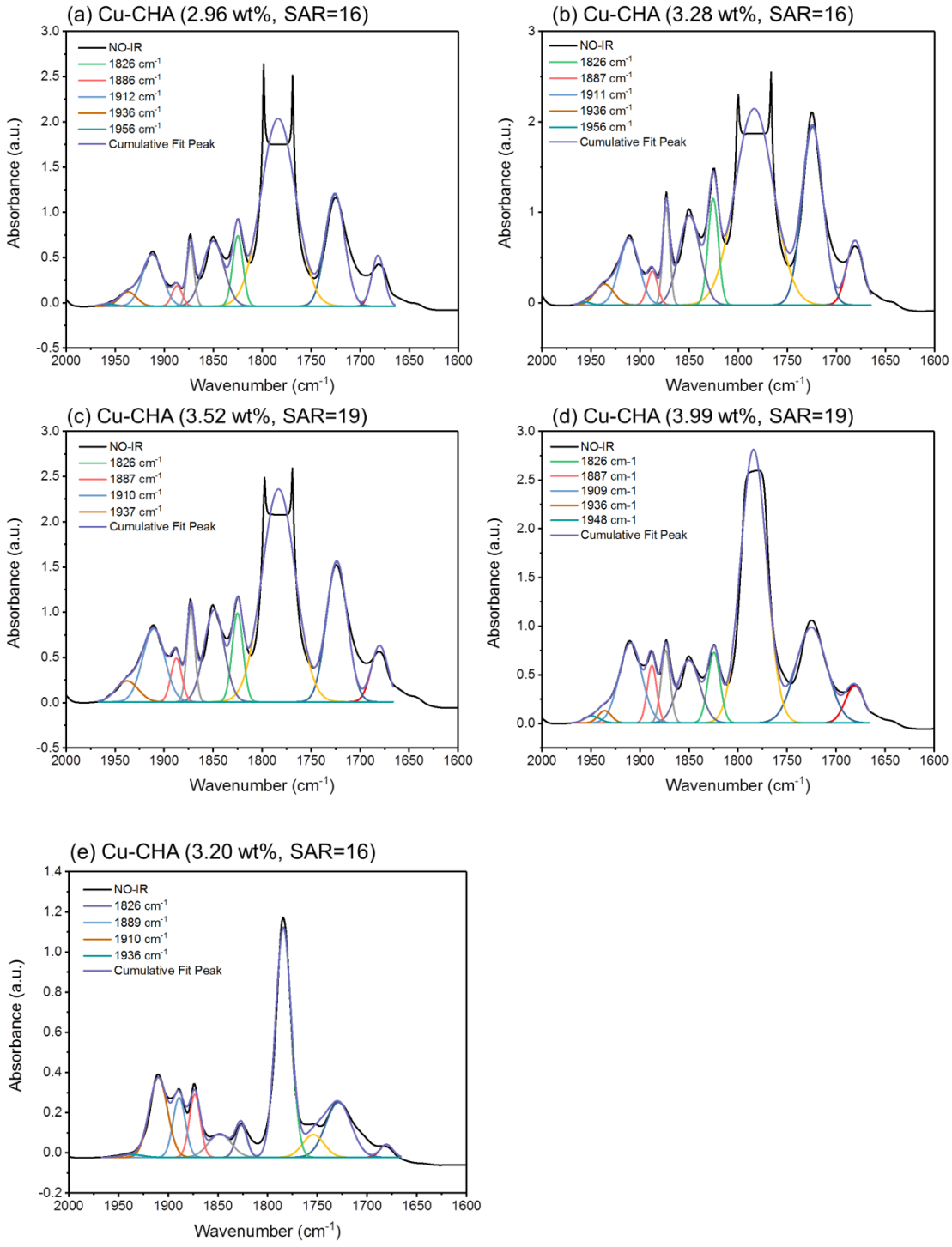

Figure S3.8. Deconvoluted IR peaks for NO adsorption IR spectra of high Cu-loading Cu-CHA samples at -160 ^{o}C by using dry air pretreatment at 400 ^{o}C. The split and flat peak shape at 1785 cm^{-1} is due to the saturation of MCT detector

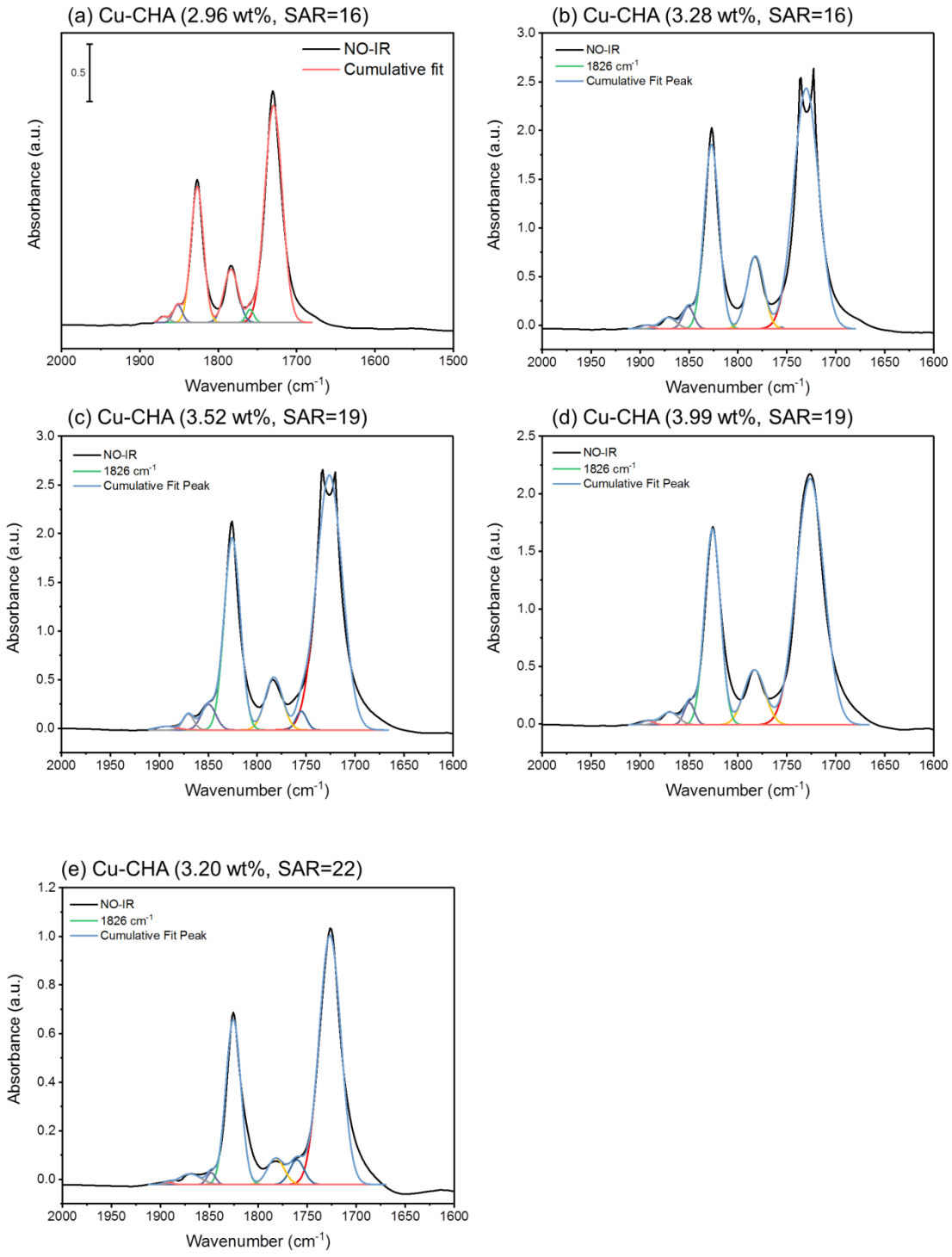

Figure S3.9. Deconvoluted IR peaks for NO adsorption IR spectra of high Cu-loading Cu-CHA samples at -160 ^{o}C by using H_2 pretreatment at 400 ^{o}C. The split and flat peak shape at 1726 cm^{-1} in is due to the saturation of MCT detector

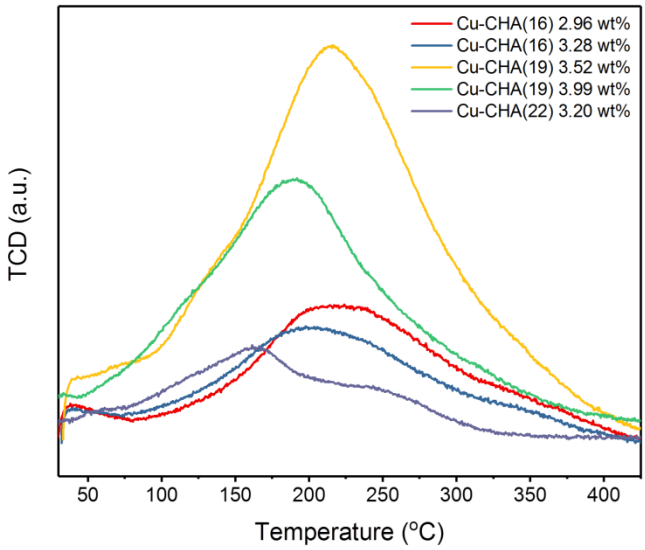

Figure S3.10. Hydrogen temperature-programmed reduction (H_2-TPR) on high Cu-loading Cu-CHA powder samples

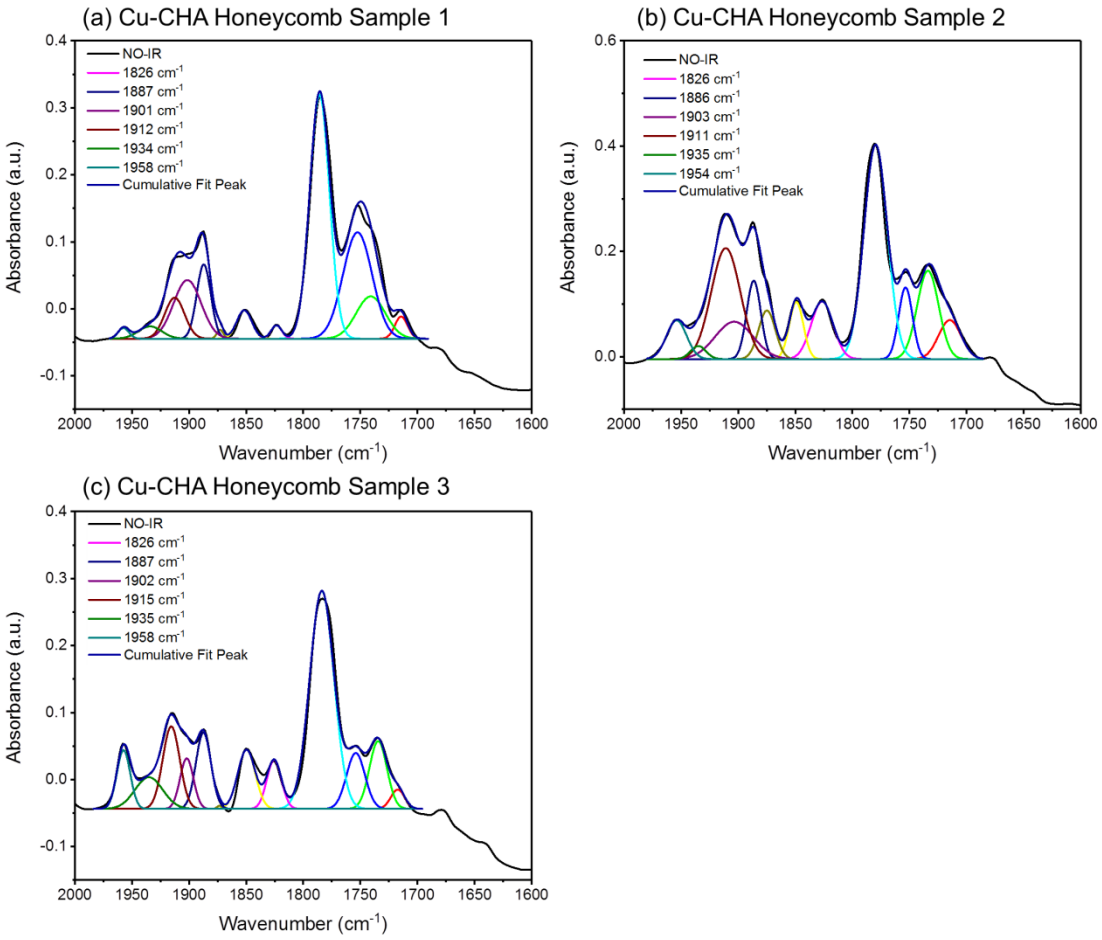

Figure S3.11. Deconvoluted IR peaks for NO adsorption IR spectra of Cu-CHA honeycomb samples at -160 ^{o}C by using dry air pretreatment at 400 ^{o}C.

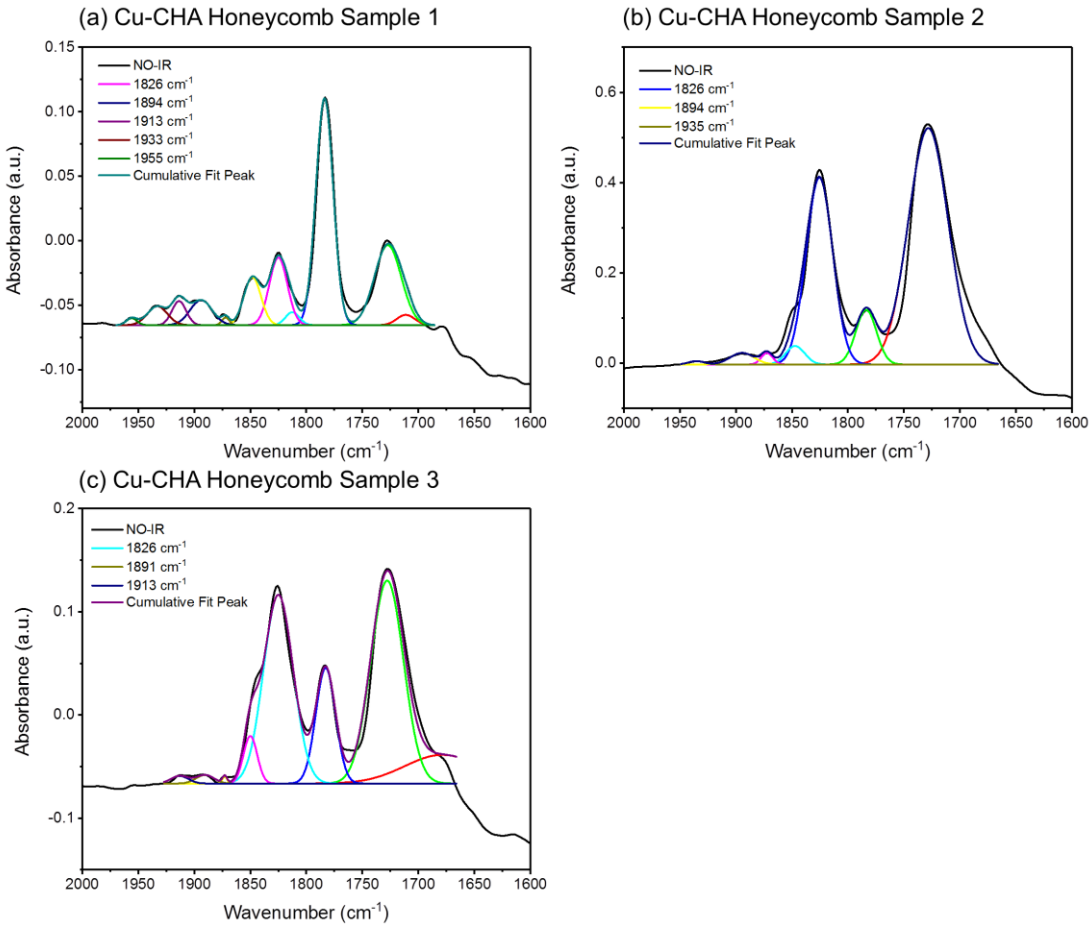

Figure S3.12. Deconvoluted IR peaks for NO adsorption IR spectra of Cu-CHA honeycomb samples at -160 ^{o}C by using H_2 pretreatment at 400 ^{o}C.

Chapter 4: Low Temperature NO and CO-IR Methodology for Identifying and Quantifying Exchanged Metal Ion in Cu-ZSM-5 and Fe-CHA

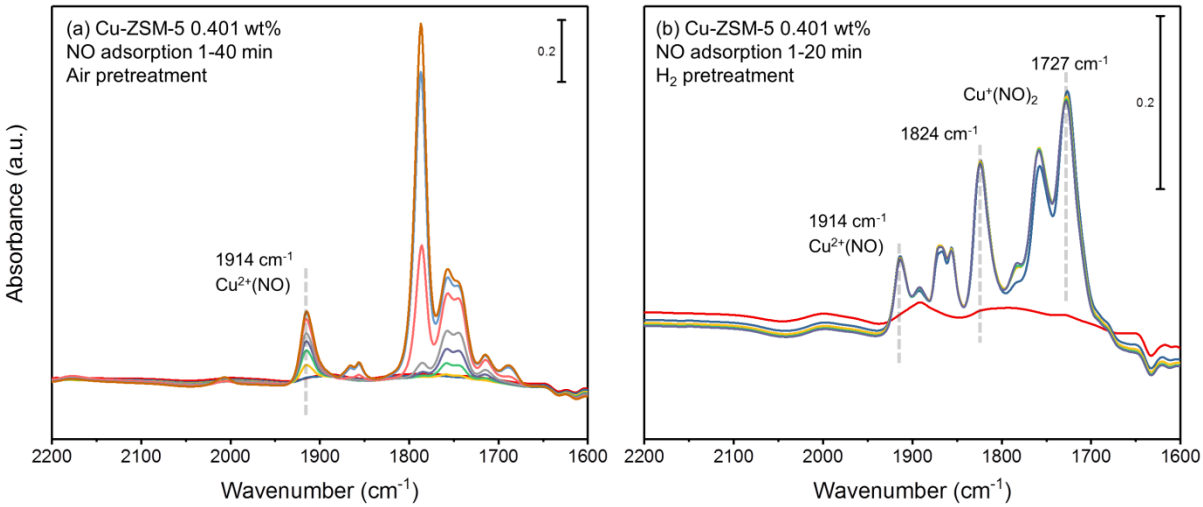

Figure S4.1. Time-resolved 1000 ppm NO/N_2 adsorption IR spectra at -160 ^oC of Cu-ZSM-5 (SAR = 30) with 0.401 wt% Cu-loading pretreated by (a) dry air and (b) 4% H_2/N_2

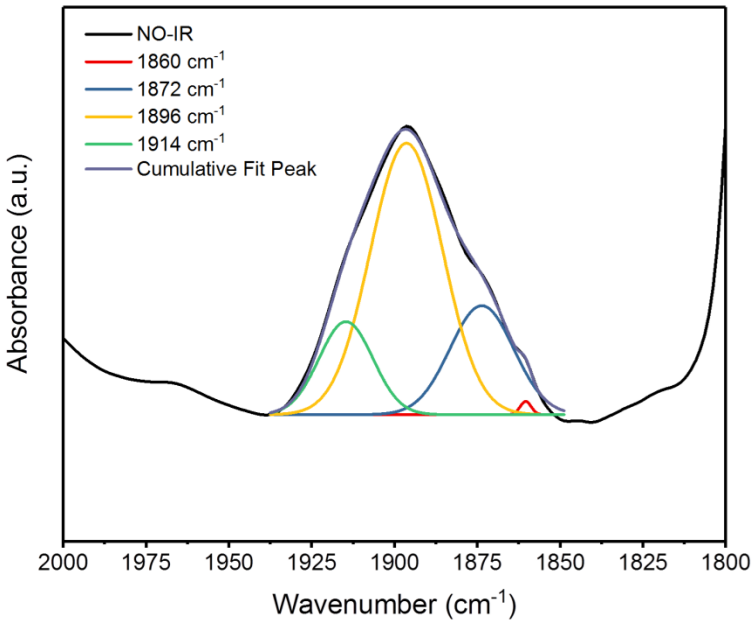

Figure S4.2. Deconvoluted IR peaks for NO adsorption Cu-ZSM-5 (0.549 wt%, SAR = 400) at -160 ^oC after dry air pretreatment

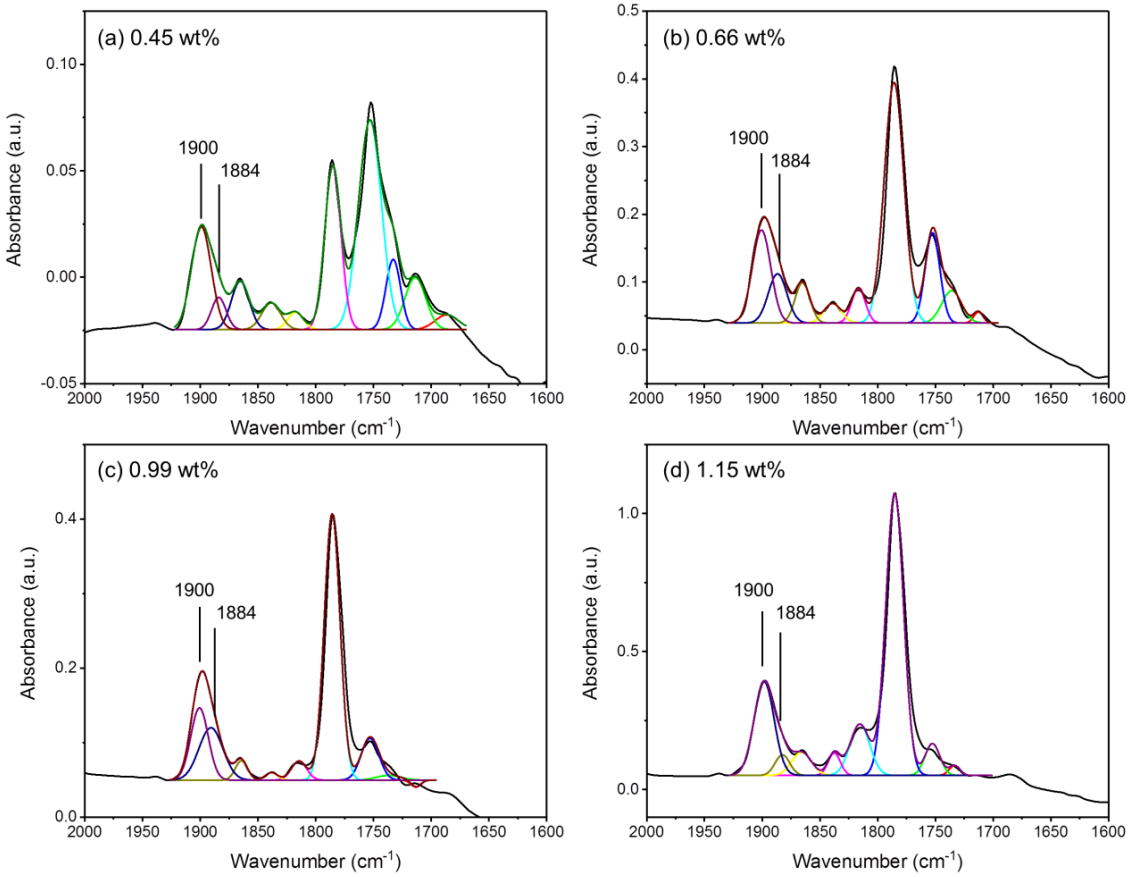

Figure S4.3. Deconvoluted IR peaks for NO-IR of Fe-CHA (SAR = 20) at -160 ^{o}C after dry air pretreatment at 400 ^{o}C

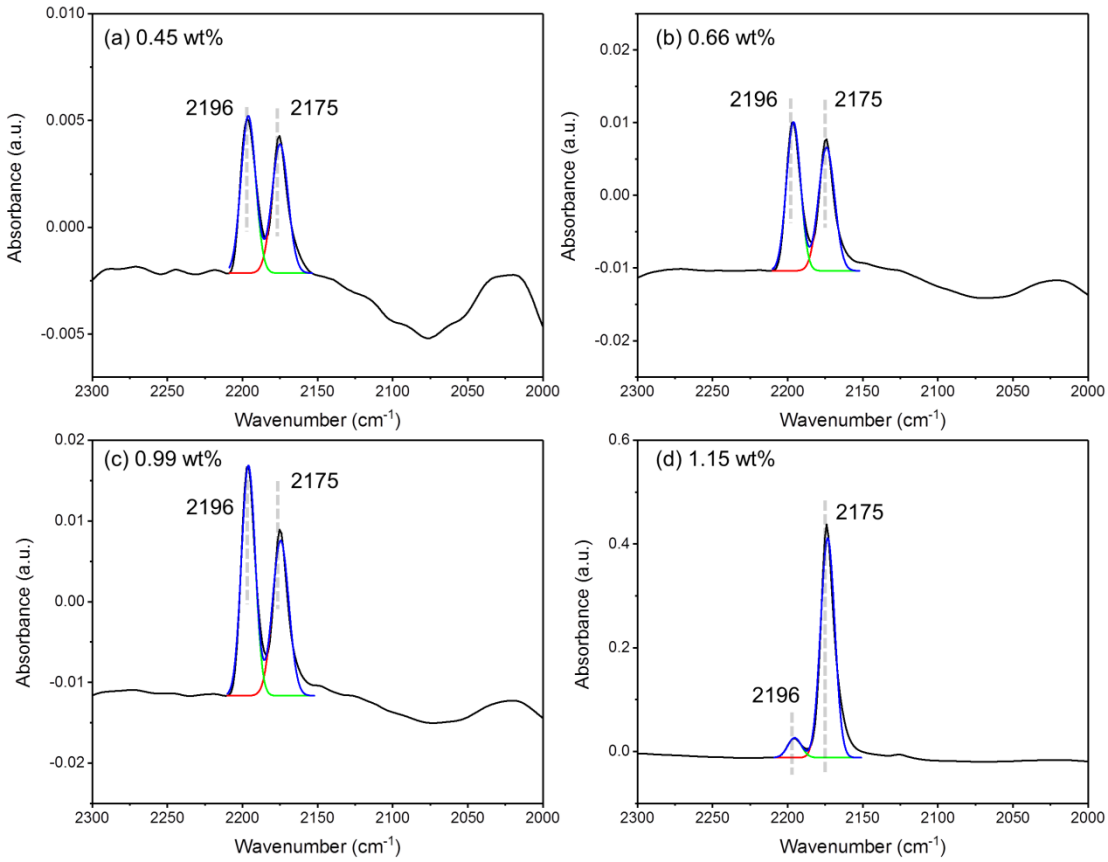

Figure S4.4. Deconvoluted IR peaks for CO-IR of Fe-CHA (SAR = 20) at -160 ^{o}C after dry air pretreatment at 400 ^{o}C

Chapter 5: Conclusions and Perspectives

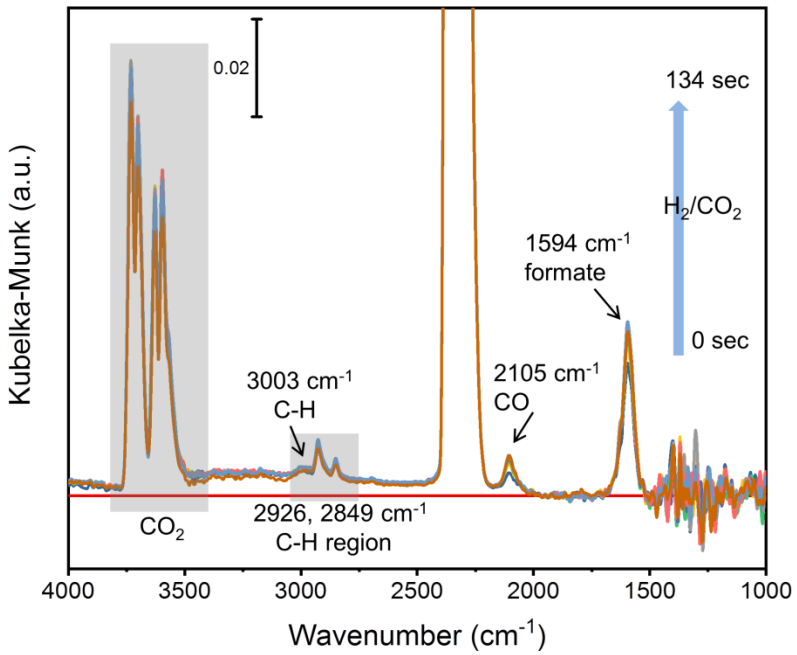

Figure S5.1. Preliminary DRIFTS spectra of CO_2/H_2 (1:3) over 10%Cu-20%Ga/SiO_2 catalyst at 230 ^{o}C

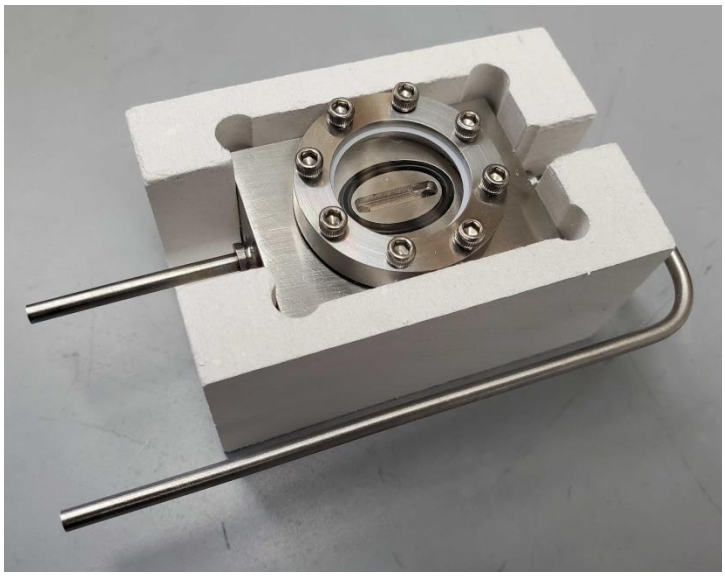

Figure S5.2. Newly designed high pressure *operando* DRIFTS cell with the capability to 300 ^{o}C, 30 bar. Refer to the literature.[224]

List of Doctoral Publications

1. P. Müller, **S.-C. Wang**, S. P. Burt, I. Hermans, Influence of Metal Doping on the Lewis Acid Catalyzed Production of Butadiene from Ethanol Studied by using Modulated Operando Diffuse Reflectance Infrared Fourier Transform Spectroscopy and Mass Spectrometry. *ChemCatChem* **2017**, *9*, 3572.

2. L. Zhang, M. R. Ball, K. R. Rivera-Dones, **S.-C. Wang**, T. F. Kuech, G. W. Huber, I. Hermans, and J. A. Dumesic, Synthesis Gas Conversion Over Molybdenum-Based Catalysts Promoted by Transition Metals. *ACS Catalysis* **2020** *10* (1), 365-374.

3. **S.-C. Wang**, M. C. Cendejas, I. Hermans, Insights into Ethanol Coupling over Hydroxyapatite using Modulation Excitation Operando Infrared Spectroscopy. *ChemCatChem* **2020**, *12*, 4167.

4. K. L. Sánchez-Rivera, P. Zhou, M. S. Kim, L. D. González Chávez, S. Grey, K. Nelson, **S.-C. Wang**, I. Hermans, V. M. Zavala, R. C. Van Lehn, G. W. Huber, Reducing Antisolvent Use in the STRAP Process by Enabling a Temperature-Controlled Polymer Dissolution and Precipitation for the Recycling of Multilayer Plastic Films. *ChemSusChem* **2021**, *14*, 4317.

5. P. A. Cuello-Penaloza, R. G. Dastidar, **S.-C. Wang**, Y. Du, M. P. Lanci, B. Wooler, C. E. Kliewer, I. Hermans, J. A. Dumesic, G. W. Huber, Ethanol to distillate-range molecules using Cu/Mg_xAlO_y catalysts with low Cu loadings. *Appl. Catal. B* **2022**, *304*, 120984.

6. **S.-C. Wang**, A. A. Abdulghani, H. Zhu, A. Moini, I. Petrovic, S. Prasad, I. Hermans, Quantification of Exchanged Copper Species in Cu-Chabazite Zeolite using Cryogenic Probe Infrared Spectroscopy. *Submitted*.

References

1. Olah, G. A., Beyond Oil and Gas: The Methanol Economy. *Angew. Chem. Int. Ed.* **2005,** *44* (18), 2636-2639.
2. de Vries, J. G.; Jackson, S. D., Homogeneous and heterogeneous catalysis in industry. *Catal. Sci. Technol* **2012,** *2* (10), 2009-2009.
3. Hu, X.; Yip, A. C. K., Heterogeneous Catalysis: Enabling a Sustainable Future. *Frontiers in Catalysis* **2021,** *1*.
4. Borisut, P.; Nuchitprasittichai, A., Methanol Production via CO2 Hydrogenation: Sensitivity Analysis and Simulation—Based Optimization. *Frontiers in Energy Research* **2019,** *7*.
5. Liu, M.; Yi, Y.; Wang, L.; Guo, H.; Bogaerts, A., Hydrogenation of Carbon Dioxide to Value-Added Chemicals by Heterogeneous Catalysis and Plasma Catalysis. *Catalysts* **2019,** *9* (3), 275.
6. Álvarez, A.; Bansode, A.; Urakawa, A.; Bavykina, A. V.; Wezendonk, T. A.; Makkee, M.; Gascon, J.; Kapteijn, F., Challenges in the Greener Production of Formates/Formic Acid, Methanol, and DME by Heterogeneously Catalyzed CO2 Hydrogenation Processes. *Chem. Rev.* **2017,** *117* (14), 9804-9838.
7. Ye, R.-P.; Ding, J.; Gong, W.; Argyle, M. D.; Zhong, Q.; Wang, Y.; Russell, C. K.; Xu, Z.; Russell, A. G.; Li, Q.; Fan, M.; Yao, Y.-G., CO2 hydrogenation to high-value products via heterogeneous catalysis. *Nature Communications* **2019,** *10* (1), 5698.
8. Barroso-Martín, I.; Infantes-Molina, A.; Jafarian Fini, F.; Ballesteros-Plata, D.; Rodríguez-Castellón, E.; Moretti, E., Silica-Related Catalysts for CO2 Transformation into Methanol and Dimethyl Ether. *Catalysts* **2020,** *10* (11), 1282.
9. Palmisano, G.; Jitan, S. A.; Garlisi, C., Chapter 2 - Fundamentals of the adsorption process. In *Heterogeneous Catalysis*, Palmisano, G.; Jitan, S. A.; Garlisi, C., Eds. Elsevier: 2022; pp 27-62.
10. Palmisano, G.; Jitan, S. A.; Garlisi, C., Chapter 3 - Adsorption models, surface reaction, and catalyst architectures. In *Heterogeneous Catalysis*, Palmisano, G.; Jitan, S. A.; Garlisi, C., Eds. Elsevier: 2022; pp 63-99.
11. Somorjai, G. A., Active Sites in Heterogeneous Catalysis**This work was supported by the U.S. Energy Research and Development Administration. In *Advances in Catalysis*, Eley, D. D.; Pines, H.; Weisz, P. B., Eds. Academic Press: 1977; Vol. 26, pp 1-68.
12. Somorjai, G. A.; McCrea, K. R.; Zhu, J., Active Sites in Heterogeneous Catalysis: Development of Molecular Concepts and Future Challenges. *Top. Catal.* **2002,** *18* (3), 157-166.
13. Taylor, H. S.; Armstrong, E. F., A theory of the catalytic surface. *Proceedings of the Royal Society of London. Series A, Containing Papers of a Mathematical and Physical Character* **1925,** *108* (745), 105-111.
14. Védrine, J. C., Revisiting active sites in heterogeneous catalysis: Their structure and their dynamic behaviour. *Appl. Catal. A: Gen.* **2014,** *474*, 40-50.

15. Zaera, F., The surface chemistry of heterogeneous catalysis: Mechanisms, selectivity, and active sites. *The Chemical Record* **2005,** *5* (3), 133-144.

16. Fujimoto, K.; Kameyama, M.; Kunugi, T., Hydrogenation of adsorbed carbon monoxide on supported platinum group metals. *J. Catal.* **1980,** *61* (1), 7-14.

17. Vannice, M. A., The catalytic synthesis of hydrocarbons from H2CO mixtures over the group VIII metals: I. The specific activities and product distributions of supported metals. *J. Catal.* **1975,** *37* (3), 449-461.

18. Degnan, T. F.; Chitnis, G. K.; Schipper, P. H., History of ZSM-5 fluid catalytic cracking additive development at Mobil. *Microporous Mesoporous Mater.* **2000,** *35-36*, 245-252.

19. Vogt, E. T. C.; Weckhuysen, B. M., Fluid catalytic cracking: recent developments on the grand old lady of zeolite catalysis. *Chem. Soc. Rev.* **2015,** *44* (20), 7342-7370.

20. Yarulina, I.; Chowdhury, A. D.; Meirer, F.; Weckhuysen, B. M.; Gascon, J., Recent trends and fundamental insights in the methanol-to-hydrocarbons process. *Nature Catalysis* **2018,** *1* (6), 398-411.

21. Chang, C. D.; Silvestri, A. J., The conversion of methanol and other O-compounds to hydrocarbons over zeolite catalysts. *J. Catal.* **1977,** *47* (2), 249-259.

22. Burcham, L. J.; Wachs, I. E., The origin of the support effect in supported metal oxide catalysts: in situ infrared and kinetic studies during methanol oxidation. *Catal. Today* **1999,** *49* (4), 467-484.

23. Liu, Y.; Deng, J.; Xie, S.; Wang, Z.; Dai, H., Catalytic removal of volatile organic compounds using ordered porous transition metal oxide and supported noble metal catalysts. *Chinese Journal of Catalysis* **2016,** *37* (8), 1193-1205.

24. Abdulrazzaq, H. T.; Rahmani Chokanlu, A.; Frederick, B. G.; Schwartz, T. J., Reaction Kinetics Analysis of Ethanol Dehydrogenation Catalyzed by MgO–SiO2. *ACS Catal.* **2020,** *10* (11), 6318-6331.

25. Chesnokov, V. V.; Bedilo, A. F.; Heroux, D. S.; Mishakov, I. V.; Klabunde, K. J., Oxidative dehydrogenation of butane over nanocrystalline MgO, Al2O3, and VOx/MgO catalysts in the presence of small amounts of iodine. *J. Catal.* **2003,** *218* (2), 438-446.

26. Holt, T. E.; Logan, A. D.; Chakraborti, S.; Datye, A. K., The effect of catalyst preparation conditions on the morphology of MgO catalyst supports. *Applied Catalysis* **1987,** *34*, 199-213.

27. Cuenya, B. R., Synthesis and catalytic properties of metal nanoparticles: Size, shape, support, composition, and oxidation state effects. *Thin Solid Films* **2010,** *518* (12), 3127-3150.

28. Yoshida, H.; Yazawa, Y.; Hattori, T., Effects of support and additive on oxidation state and activity of Pt catalyst in propane combustion. *Catal. Today* **2003,** *87* (1), 19-28.

29. Choudhary, V. R.; Samanta, C.; Choudhary, T. V., Direct oxidation of H2 to H2O2 over Pd-based catalysts: Influence of oxidation state, support and metal additives. *Appl. Catal. A: Gen.* **2006,** *308*, 128-133.

30. Yazawa, Y.; Yoshida, H.; Takagi, N.; Komai, S.-i.; Satsuma, A.; Hattori, T., Acid Strength of Support Materials as a Factor Controlling Oxidation State of Palladium Catalyst for Propane Combustion. *J. Catal.* **1999,** *187* (1), 15-23.

31. Adschiri, T.; Furusawa, T., Relation between CO2-reactivity of coal char and BET surface area. *Fuel* **1986,** *65* (7), 927-931.

32. Salvador, P.; Kladnig, W., Surface reactivity of zeolites type H-Y and Na-Y with methanol. *Journal of the Chemical Society, Faraday Transactions 1: Physical Chemistry in Condensed Phases* **1977,** *73* (0), 1153-1168.

33. Alonso, D. M.; Wettstein, S. G.; Dumesic, J. A., Bimetallic catalysts for upgrading of biomass to fuels and chemicals. *Chem. Soc. Rev.* **2012,** *41* (24), 8075-8098.

34. Ying, Y.; Luo, X.; Qiao, J.; Huang, H., "More is Different:" Synergistic Effect and Structural Engineering in Double-Atom Catalysts. *Adv. Funct. Mater.* **2021,** *31* (3), 2007423.

35. Ellert, O. G.; Tsodikov, M. V.; Nikolaev, S. A.; Novotortsev, V. M., Bimetallic nanoalloys in heterogeneous catalysis of industrially important reactions: synergistic effects and structural organization of active components. *Russian Chemical Reviews* **2014,** *83* (8), 718-732.

36. Aziz, A.; Kim, K. S., Synergistic effect of UV pretreated Fe-ZSM-5 catalysts for heterogeneous catalytic complete oxidation of VOC: A technology development for sustainable use. *J. Hazard. Mater.* **2017,** *340*, 351-359.

37. Fu, J.; Dong, J.; Si, R.; Sun, K.; Zhang, J.; Li, M.; Yu, N.; Zhang, B.; Humphrey, M. G.; Fu, Q.; Huang, J., Synergistic Effects for Enhanced Catalysis in a Dual Single-Atom Catalyst. *ACS Catal.* **2021,** *11* (4), 1952-1961.

38. Palmisano, G.; Jitan, S. A.; Garlisi, C., Chapter 7 - Characterization techniques. In *Heterogeneous Catalysis*, Palmisano, G.; Jitan, S. A.; Garlisi, C., Eds. Elsevier: 2022; pp 243-314.

39. Delgass, W. N.; Haller, G. L.; Kellerman, R.; Lunsford, J. H., Chapter 2 - INFRARED SPECTROSCOPY. In *Spectroscopy in Heterogeneous Catalysis*, Delgass, W. N.; Haller, G. L.; Kellerman, R.; Lunsford, J. H., Eds. Academic Press: 1979; pp 19-57.

40. Matyshak, V. A.; Krylov, O. V., In situ IR spectroscopy of intermediates in heterogeneous oxidative catalysis. *Catal. Today* **1995,** *25* (1), 1-87.

41. Savara, A.; Weitz, E., Elucidation of Intermediates and Mechanisms in Heterogeneous Catalysis Using Infrared Spectroscopy. *Annu. Rev. Phys. Chem.* **2014,** *65* (1), 249-273.

42. Weckhuysen, B. M., Snapshots of a working catalyst: possibilities and limitations of in situ spectroscopy in the field of heterogeneous catalysis. *Chem. Commun.* **2002,** (2), 97-110.

43. Paukshtis, E. A.; Yurchenko, E. N., Study of the Acid–Base Properties of Heterogeneous Catalysts by Infrared Spectroscopy. *Russian Chemical Reviews* **1983,** *52* (3), 242-258.

44. Montanari, T.; Finocchio, E.; Busca, G., Infrared Spectroscopy of Heterogeneous Catalysts: Acidity and Accessibility of Acid Sites of Faujasite-Type Solid Acids. *J. Phys. Chem. C.* **2011,** *115* (4), 937-943.

45. Lamberti, C.; Zecchina, A.; Groppo, E.; Bordiga, S., Probing the surfaces of heterogeneous catalysts by in situ IR spectroscopy. *Chem. Soc. Rev.* **2010,** *39* (12), 4951-5001.

46. Parry, E. P., An infrared study of pyridine adsorbed on acidic solids. Characterization of surface acidity. *J. Catal.* **1963,** *2* (5), 371-379.

47. Datka, J.; Turek, A. M.; Jehng, J. M.; Wachs, I. E., Acidic properties of supported niobium oxide catalysts: An infrared spectroscopy investigation. *J. Catal.* **1992,** *135* (1), 186-199.

48. Emeis, C. A., Determination of Integrated Molar Extinction Coefficients for Infrared Absorption Bands of Pyridine Adsorbed on Solid Acid Catalysts. *J. Catal.* **1993,** *141* (2), 347-354.

49. Johnson, B. A.; Di Iorio, J. R.; Román-Leshkov, Y., Identification and quantification of distinct active sites in Hf-Beta zeolites for transfer hydrogenation catalysis. *J. Catal.* **2021,** *404*, 607-619.

50. Morterra, C.; Coluccia, S.; Chiorino, A.; Boccuzzi, F., Infrared study of the adsorption of pyridine on α-Al2O3. *J. Catal.* **1978,** *54* (3), 348-364.

51. Khabtou, S.; Chevreau, T.; Lavalley, J. C., Quantitative infrared study of the distinct acidic hydroxyl groups contained in modified Y zeolites. *Microporous Mater.* **1994,** *3* (1), 133-148.

52. McCue, A. J.; Mutch, G. A.; McNab, A. I.; Campbell, S.; Anderson, J. A., Quantitative determination of surface species and adsorption sites using Infrared spectroscopy. *Catal. Today* **2016,** *259*, 19-26.

53. Lothian, G. F., Beer's law and its use in analysis. A review. *Analyst* **1963,** *88* (1050), 678-685.

54. Zholobenko, V.; Freitas, C.; Jendrlin, M.; Bazin, P.; Travert, A.; Thibault-Starzyk, F., Probing the acid sites of zeolites with pyridine: Quantitative AGIR measurements of the molar absorption coefficients. *J. Catal.* **2020,** *385*, 52-60.

55. Rhee, K. H.; Brown, F. R.; Finseth, D. H.; Stencel, J. M., Infrared studies on the acidity of metal impregnated ZSM-5. *Zeolites* **1983,** *3* (4), 344-347.

56. Kung, M. C.; Kung, H. H., IR Studies of NH3, Pyridine, CO, and NO Adsorbed on Transition Metal Oxides. *Catalysis Reviews* **1985,** *27* (3), 425-460.

57. Rhee, K. H.; Udaya, V.; Rao, S.; Stencel, J. M.; Melson, G. A.; Crawford, J. E., Supported transition metal compounds: Infrared studies on the acidity of Co/ZSM-5 and Fe/ZSM-5 catalysts. *Zeolites* **1983,** *3* (4), 337-343.

58. Kiviat, F. E.; Petrakis, L., Surface acidity of transition metal modified aluminas. Infrared and nuclear magnetic resonance investigation of adsorbed pyridine. *The Journal of Physical Chemistry* **1973,** *77* (10), 1232-1239.

59. Poncelet, G.; Dubru, M. L., An infrared study of the surface acidity of germanic near-faujasite zeolite by pyridine adsorption. *J. Catal.* **1978,** *52* (2), 321-331.

60. Topaloğlu Yazıcı, D.; Bilgiç, C., Determining the surface acidic properties of solid catalysts by amine titration using Hammett indicators and FTIR-pyridine adsorption methods. *Surf. Interface Anal.* **2010,** *42* (6-7), 959-962.

61. Nesterenko, N. S.; Thibault-Starzyk, F.; Montouilliout, V.; Yushchenko, V. V.; Fernandez, C.; Gilson, J. P.; Fajula, F.; Ivanova, I. I., The use of the consecutive adsorption of pyridine bases and carbon monoxide in the IR spectroscopic study of the accessibility of acid sites in microporous/mesoporous materials. *Kinet. Catal.* **2006,** *47* (1), 40-48.

62. Buzzoni, R.; Bordiga, S.; Ricchiardi, G.; Lamberti, C.; Zecchina, A.; Bellussi, G., Interaction of Pyridine with Acidic (H-ZSM5, H-β, H-MORD Zeolites) and Superacidic (H-Nafion Membrane) Systems: An IR Investigation. *Langmuir* **1996,** *12* (4), 930-940.

63. Zecchina, A.; Scarano, D.; Bordiga, S.; Ricchiardi, G.; Spoto, G.; Geobaldo, F., IR studies of CO and NO adsorbed on well characterized oxide single microcrystals. *Catal. Today* **1996,** *27* (3), 403-435.

64. Zecchina, A.; Areán, C. O., Diatomic molecular probes for mid-IR studies of zeolites. *Chem. Soc. Rev.* **1996,** *25* (3), 187-197.

65. Lange, F.; Hadjiivanov, K.; Schmelz, H.; Knözinger, H., Low temperature infrared study of carbon monoxide adsorption on sulfated titania. *Catal. Lett.* **1992,** *16* (1), 97-107.

66. Gruver, V.; Panov, A.; Fripiat, J. J., Infrared Study of CO Chemisorbed on Brönsted and Lewis Sites in Dealuminated Acid Y and ZSM-5 Zeolites. *Langmuir* **1996,** *12* (10), 2505-2513.

67. Zaki, M. I.; Knözlngem, H., Characterization of oxide surfaces by adsorption of carbon monoxide—a low temperature infrared spectroscopy study. *Spectrochim. Acta, Pt. A: Mol. Spectrosc.* **1987,** *43* (12), 1455-1459.

68. Willner, H.; Aubke, F., Homoleptic Metal Carbonyl Cations of the Electron-Rich Metals: Their Generation in Superacid Media Together with Their Spectroscopic and Structural Characterization. *Angew. Chem., Int. Ed. Engl.* **1997,** *36* (22), 2402-2425.

69. Knözinger, H., Infrared Spectroscopy as a Probe of Surface Acidity. In *Elementary Reaction Steps in Heterogeneous Catalysis*, Joyner, R. W.; van Santen, R. A., Eds. Springer Netherlands: Dordrecht, 1993; pp 267-285.

70. Hammer, B.; Morikawa, Y.; Nørskov, J. K., CO Chemisorption at Metal Surfaces and Overlayers. *Phys. Rev. Lett.* **1996,** *76* (12), 2141-2144.

71. Hollins, P.; Pritchard, J., Infrared studies of chemisorbed layers on single crystals. *Prog. Surf. Sci.* **1985,** *19* (4), 275-349.

72. Sheppard, N.; De La Cruz, C., The reliability of vibrational spectroscopy as a means of identification of the structures of chemisorbed species on metal surfaces: the cases of CO, NO and C2 hydrocarbon surface species. *Catal. Today* **2001,** *70* (1), 3-13.

73. de la Cruz, C.; Sheppard, N., A review of vCO bond-stretching wavenumbers for CO ligands in metal coordination compounds or clusters with emphasis on the less common types of metal/CO bonding patterns, and of the relationship between vCO and the internuclear distance, r(CO). *J. Mol. Struct.* **1990,** *224*, 141-161.

74. King, D. L.; Peri, J. B., An infrared study of nitric oxide chemisorption on alumina-supported iron and alkalized iron Fischer-Tropsch catalysts. *J. Catal.* **1983,** *79* (1), 164-175.

75. Peri, J. B., Infrared study of nitric oxide and carbon monoxide adsorbed on chromia/alumina. *The Journal of Physical Chemistry* **1974,** *78* (6), 588-594.

76. Arai, H.; Tominaga, H., An infrared study of nitric oxide adsorbed on rhodium-alumina catalyst. *J. Catal.* **1976,** *43* (1), 131-142.

77. Kometer, R.; Legay, F.; Legay - Sommaire, N.; Schwentner, N., Vibrational spectroscopy of NO and (NO)2 isolated in solid neon. *The Journal of Chemical Physics* **1994,** *100* (12), 8737-8745.

78. Giordanino, F.; Vennestrøm, P. N. R.; Lundegaard, L. F.; Stappen, F. N.; Mossin, S.; Beato, P.; Bordiga, S.; Lamberti, C., Characterization of Cu-exchanged SSZ-13: a comparative FTIR, UV-Vis, and EPR study with Cu-ZSM-5 and Cu-β with similar Si/Al and Cu/Al ratios. *Dalton Trans.* **2013,** *42* (35), 12741-12761.

79. Zhang, R.; McEwen, J.-S.; Kollár, M.; Gao, F.; Wang, Y.; Szanyi, J.; Peden, C. H. F., NO Chemisorption on Cu/SSZ-13: A Comparative Study from Infrared Spectroscopy and DFT Calculations. *ACS Catal.* **2014,** *4* (11), 4093-4105.

80. Weckhuysen, B. M., Operando spectroscopy: fundamental and technical aspects of spectroscopy of catalysts under working conditions. *PCCP* **2003,** *5* (20), vi-vi.

81. Hernández-Giménez, A. M.; Ruiz-Martínez, J.; Puértolas, B.; Pérez-Ramírez, J.; Bruijnincx, P. C. A.; Weckhuysen, B. M., Operando Spectroscopy of the Gas-Phase Aldol Condensation of Propanal over Solid Base Catalysts. *Top. Catal.* **2017,** *60* (19), 1522-1536.

82. Urakawa, A., Trends and advances in Operando methodology. *Current Opinion in Chemical Engineering* **2016,** *12*, 31-36.

83. Meemken, F.; Müller, P.; Hungerbühler, K.; Baiker, A., Simultaneous probing of bulk liquid phase and catalytic gas-liquid-solid interface under working conditions using attenuated total reflection infrared spectroscopy. *Rev. Sci. Instrum.* **2014,** *85* (8), 084101.

84. Müller, P.; Hermans, I., Applications of Modulation Excitation Spectroscopy in Heterogeneous Catalysis. *Ind. Eng. Chem. Res.* **2017,** *56* (5), 1123-1136.

85. Srinivasan, P. D.; Patil, B. S.; Zhu, H.; Bravo-Suárez, J. J., Application of modulation excitation-phase sensitive detection-DRIFTS for in situ/operando characterization of heterogeneous catalysts. *Reaction Chemistry & Engineering* **2019,** *4* (5), 862-883.

86. Ortelli, E. E.; Wambach, J.; Wokaun, A., Use of periodic variations of reactant concentrations in time resolved DRIFT studies of heterogeneously catalysed reactions. *Appl. Catal. A: Gen.* **2000,** *192* (1), 137-152.

87. Müller, P.; Burt, S. P.; Love, A. M.; McDermott, W. P.; Wolf, P.; Hermans, I., Mechanistic Study on the Lewis Acid Catalyzed Synthesis of 1,3-Butadiene over Ta-BEA Using Modulated Operando DRIFTS-MS. *ACS Catal.* **2016,** *6* (10), 6823-6832.

88. Müller, P.; Wolf, P.; Hermans, I., Insights into the Complexity of Heterogeneous Liquid-Phase Catalysis: Case Study on the Cyclization of Citronellal. *ACS Catal.* **2016,** *6* (5), 2760-2769.

89. Müller, P.; Wang, S.-C.; Burt, S. P.; Hermans, I., Influence of Metal Doping on the Lewis Acid Catalyzed Production of Butadiene from Ethanol Studied by using Modulated Operando Diffuse Reflectance Infrared Fourier Transform Spectroscopy and Mass Spectrometry. *ChemCatChem* **2017,** *9* (18), 3572-3582.

90. Baurecht, D.; Fringeli, U. P., Quantitative modulated excitation Fourier transform infrared spectroscopy. *Rev. Sci. Instrum.* **2001,** *72* (10), 3782-3792.

91. Urakawa, A.; Bürgi, T.; Baiker, A., Sensitivity enhancement and dynamic behavior analysis by modulation excitation spectroscopy: Principle and application in heterogeneous catalysis. *Chem. Eng. Sci.* **2008,** *63* (20), 4902-4909.

92. Shulda, S.; Richards, R. M., Chapter 5 - Modulation Excitation Spectroscopy with Phase-Sensitive Detection for Surface Analysis. In *New Materials for Catalytic Applications*, Parvulescu, V. I.; Kemnitz, E., Eds. Elsevier: Amsterdam, 2016; pp 121-132.

93. Zaera, F., New advances in the use of infrared absorption spectroscopy for the characterization of heterogeneous catalytic reactions. *Chem. Soc. Rev.* **2014,** *43* (22), 7624-7663.

94. Mojet, B. L.; Ebbesen, S. D.; Lefferts, L., Light at the interface: the potential of attenuated total reflection infrared spectroscopy for understanding heterogeneous catalysis in water. *Chem. Soc. Rev.* **2010,** *39* (12), 4643-4655.

95. Bürgi, T., In situ Spectroscopy of Catalytic Solid–Liquid Interfaces and Chiral Surfaces. *CHIMIA* **2003,** *57* (10), 623.

96. Andanson, J.-M.; Baiker, A., Exploring catalytic solid/liquid interfaces by in situ attenuated total reflection infrared spectroscopy. *Chem. Soc. Rev.* **2010,** *39* (12), 4571-4584.

97. Harrick, N. J., *Internal reflection spectroscopy*. 1967.

98. Laroche, G.; Fitremann, J.; Gherardi, N., FTIR-ATR spectroscopy in thin film studies: The importance of sampling depth and deposition substrate. *Appl. Surf. Sci.* **2013,** *273*, 632-637.

99. Schubert, M. M.; Häring, T. P.; Bräth, G.; Gasteiger, H. A.; Behm, R. J., New DRIFTS Cell Design for the Simultaneous Acquisition of IR Spectra and Kinetic Data Using On-Line Product Analysis. *Appl. Spectrosc.* **2001,** *55* (11), 1537-1543.

100. Meunier, F. C.; Goguet, A.; Shekhtman, S.; Rooney, D.; Daly, H., A modified commercial DRIFTS cell for kinetically relevant operando studies of heterogeneous catalytic reactions. *Appl. Catal. A: Gen.* **2008,** *340* (2), 196-202.

101. Drochner, A.; Fehlings, M.; Krauß, K.; Vogel, H., A New DRIFTS Cell for the In-Situ Investigation of Heterogeneously Catalyzed Reactions. *Chemical Engineering & Technology* **2000,** *23* (4), 319-322.

102. Venter, J. J.; Vannice, M. A., Modifications of a Diffuse Reflectance Cell to Allow the Characterization of Carbon-Supported Metals by DRIFTS. *Appl. Spectrosc.* **1988,** *42* (6), 1096-1103.

103. Prairie, M. R.; Highfield, J. G.; Renken, A., Diffuse-reflectance FTIR spectroscopy for kinetic and mechanistic studies of CO2 hydrogenation in a continuous recycle reactor. *Chem. Eng. Sci.* **1991,** *46* (1), 113-121.

104. Meunier, F. C., Pitfalls and benefits of in situ and operando diffuse reflectance FT-IR spectroscopy (DRIFTS) applied to catalytic reactions. *Reaction Chemistry & Engineering* **2016,** *1* (2), 134-141.

105. Wang, S.-C.; Cendejas, M. C.; Hermans, I., Insights into Ethanol Coupling over Hydroxyapatite using Modulation Excitation Operando Infrared Spectroscopy. *ChemCatChem* **2020,** *12* (16), 4167-4175.

106. Jin, C.; Yao, M.; Liu, H.; Lee, C.-f. F.; Ji, J., Progress in the production and application of n-butanol as a biofuel. *Renew. Sust. Energ. Rev.* **2011,** *15* (8), 4080-4106.

107. Savage, N., Fuel options: The ideal biofuel. *Nature* **2011,** *474* (7352), S9-S11.

108. O'Rourke, C. E.; Kavasmaneck, P. R.; Uhl, R. E., Manufacture of <italic>n</italic>-Butanol and 2-Ethylhexanol by the Rhodium Oxo Process and Applications of the Alcohols. In *Monohydric Alcohols*, AMERICAN CHEMICAL SOCIETY: 1981; Vol. 159, pp 71-85.

109. Torres, G. M.; Frauenlob, R.; Franke, R.; Börner, A., Production of alcohols via hydroformylation. *Catal. Sci. Technol* **2015,** *5* (1), 34-54.

110. Veibel, S.; Nielsen, J. I., On the mechanism of the Guerbet reaction. *Tetrahedron* **1967,** *23* (4), 1723-1733.

111. Gabriels, D.; Hernandez, W. Y.; Sels, B.; Van Der Voort, P.; Verberckmoes, A., Review of catalytic systems and thermodynamics for the Guerbet condensation reaction and challenges for biomass valorization. *Catal. Sci. Technol* **2015,** *5* (8), 3876-3902.

112. O'Lenick Jr., A. J., Guerbet chemistry. *Journal of Surfactants and Detergents* **2001,** *4* (3), 311-315.

113. Scalbert, J.; Thibault-Starzyk, F.; Jacquot, R.; Morvan, D.; Meunier, F., Ethanol condensation to butanol at high temperatures over a basic heterogeneous catalyst: How relevant is acetaldehyde self-aldolization? *J. Catal.* **2014,** *311*, 28-32.

114. Kozlowski, J. T.; Davis, R. J., Heterogeneous Catalysts for the Guerbet Coupling of Alcohols. *ACS Catal.* **2013,** *3* (7), 1588-1600.

115. Wu, X.; Fang, G.; Tong, Y.; Jiang, D.; Liang, Z.; Leng, W.; Liu, L.; Tu, P.; Wang, H.; Ni, J.; Li, X., Catalytic Upgrading of Ethanol to n-Butanol: Progress in Catalyst Development. *ChemSusChem* **2018,** *11* (1), 71-85.

116. Tsuchida, T.; Sakuma, S.; Takeguchi, T.; Ueda, W., Direct Synthesis of n-Butanol from Ethanol over Nonstoichiometric Hydroxyapatite. *Ind. Eng. Chem. Res.* **2006,** *45* (25), 8634-8642.

117. Tsuchida, T.; Kubo, J.; Yoshioka, T.; Sakuma, S.; Takeguchi, T.; Ueda, W., Reaction of ethanol over hydroxyapatite affected by Ca/P ratio of catalyst. *J. Catal.* **2008,** *259* (2), 183-189.

118. Silvester, L.; Lamonier, J.-F.; Faye, J.; Capron, M.; Vannier, R.-N.; Lamonier, C.; Dubois, J.-L.; Couturier, J.-L.; Calais, C.; Dumeignil, F., Reactivity of ethanol over

hydroxyapatite-based Ca-enriched catalysts with various carbonate contents. *Catal. Sci. Technol* **2015,** *5* (5), 2994-3006.

119. Ben Osman, M.; Diallo Garcia, S.; Krafft, J.-M.; Methivier, C.; Blanchard, J.; Yoshioka, T.; Kubo, J.; Costentin, G., Control of calcium accessibility over hydroxyapatite by post-precipitation steps: influence on the catalytic reactivity toward alcohols. *PCCP* **2016,** *18* (40), 27837-27847.

120. Ogo, S.; Onda, A.; Iwasa, Y.; Hara, K.; Fukuoka, A.; Yanagisawa, K., 1-Butanol synthesis from ethanol over strontium phosphate hydroxyapatite catalysts with various Sr/P ratios. *J. Catal.* **2012,** *296*, 24-30.

121. Ogo, S.; Onda, A.; Yanagisawa, K., Selective synthesis of 1-butanol from ethanol over strontium phosphate hydroxyapatite catalysts. *Appl. Catal. A: Gen.* **2011,** *402* (1), 188-195.

122. Hanspal, S.; Young, Z. D.; Shou, H.; Davis, R. J., Multiproduct Steady-State Isotopic Transient Kinetic Analysis of the Ethanol Coupling Reaction over Hydroxyapatite and Magnesia. *ACS Catal.* **2015,** *5* (3), 1737-1746.

123. Moteki, T.; Flaherty, D. W., Mechanistic Insight to C–C Bond Formation and Predictive Models for Cascade Reactions among Alcohols on Ca- and Sr-Hydroxyapatites. *ACS Catal.* **2016,** *6* (7), 4170-4183.

124. Ho, C. R.; Shylesh, S.; Bell, A. T., Mechanism and Kinetics of Ethanol Coupling to Butanol over Hydroxyapatite. *ACS Catal.* **2016,** *6* (2), 939-948.

125. Young, Z. D.; Davis, R. J., Hydrogen transfer reactions relevant to Guerbet coupling of alcohols over hydroxyapatite and magnesium oxide catalysts. *Catal. Sci. Technol* **2018,** *8* (6), 1722-1729.

126. Diallo-Garcia, S.; Osman, M. B.; Krafft, J.-M.; Casale, S.; Thomas, C.; Kubo, J.; Costentin, G., Identification of Surface Basic Sites and Acid–Base Pairs of Hydroxyapatite. *J. Phys. Chem. C.* **2014,** *118* (24), 12744-12757.

127. Hill, I. M.; Hanspal, S.; Young, Z. D.; Davis, R. J., DRIFTS of Probe Molecules Adsorbed on Magnesia, Zirconia, and Hydroxyapatite Catalysts. *J. Phys. Chem. C.* **2015,** *119* (17), 9186-9197.

128. Osman, M. B.; Krafft, J.-M.; Thomas, C.; Yoshioka, T.; Kubo, J.; Costentin, G., Importance of the Nature of the Active Acid/Base Pairs of Hydroxyapatite Involved in the Catalytic Transformation of Ethanol to n-Butanol Revealed by Operando DRIFTS. *ChemCatChem* **2019,** *11* (6), 1765-1778.

129. Müller, P.; Wang, S. C.; Burt, S. P.; Hermans, I., Influence of Metal Doping on the Lewis Acid Catalyzed Production of Butadiene from Ethanol Studied by using Modulated Operando Diffuse Reflectance Infrared Fourier Transform Spectroscopy and Mass Spectrometry. *ChemCatChem* **2017,** *9* (18), 3572-3582.

130. Hexter, R. M., Excitation-Modulation Spectroscopy: A Technique for Obtaining Vibrational Spectra of Excited Electronic States*. *J. Opt. Soc. Am.* **1963,** *53* (6), 703-709.

131. Fringeli, U. P.; Günthard, H. H., Modulated Excitation Infrared Spectrophotometer. *Appl. Opt.* **1971,** *10* (4), 819-824.

132. Cheng, Z. H.; Yasukawa, A.; Kandori, K.; Ishikawa, T., FTIR Study of Adsorption of CO2 on Nonstoichiometric Calcium Hydroxyapatite. *Langmuir* **1998,** *14* (23), 6681-6686.

133. Diallo-Garcia, S.; Ben Osman, M.; Krafft, J.-M.; Boujday, S.; Guylène, C., Discrimination of infrared fingerprints of bulk and surface POH and OH of hydroxyapatites. *Catal. Today* **2014,** *226*, 81-88.

134. Kay, M. I.; Young, R. A.; Posner, A. S., Crystal Structure of Hydroxyapatite. *Nature* **1964,** *204*, 1050.

135. Hanspal, S.; Young, Z. D.; Prillaman, J. T.; Davis, R. J., Influence of surface acid and base sites on the Guerbet coupling of ethanol to butanol over metal phosphate catalysts. *J. Catal.* **2017,** *352*, 182-190.

136. Kondo, J. N.; Domen, K., IR observation of adsorption and reactions of olefins on H-form zeolites. *J. Mol. Catal. A: Chem.* **2003,** *199* (1), 27-38.

137. Schächter, Y.; Pines, H., Calcium-oxide-catalyzed reactions of hydrocarbons and of alcohols. *J. Catal.* **1968,** *11* (2), 147-158.

138. Jonson, J. E.; Borken-Kleefeld, J.; Simpson, D.; Nyíri, A.; Posch, M.; Heyes, C., Impact of excess NO _x emissions from diesel cars on air quality, public health and eutrophication in Europe. *Environmental Research Letters* **2017,** *12* (9), 094017.

139. Lu, X.; Yao, T.; Li, Y.; Fung, J. C. H.; Lau, A. K. H., Source apportionment and health effect of NOx over the Pearl River Delta region in southern China. *Environ. Pollut.* **2016,** *212*, 135-146.

140. Koebel, M.; Elsener, M.; Kleemann, M., Urea-SCR: a promising technique to reduce NOx emissions from automotive diesel engines. *Catal. Today* **2000,** *59* (3), 335-345.

141. Praveena, V.; Martin, M. L. J., A review on various after treatment techniques to reduce NOx emissions in a CI engine. *Journal of the Energy Institute* **2018,** *91* (5), 704-720.

142. Gounder, R.; Moini, A., Automotive NOx abatement using zeolite-based technologies. *Reaction Chemistry & Engineering* **2019,** *4* (6), 966-968.

143. Kwak, J. H.; Tonkyn, R. G.; Kim, D. H.; Szanyi, J.; Peden, C. H. F., Excellent activity and selectivity of Cu-SSZ-13 in the selective catalytic reduction of NOx with NH3. *J. Catal.* **2010,** *275* (2), 187-190.

144. Bates, S. A.; Verma, A. A.; Paolucci, C.; Parekh, A. A.; Anggara, T.; Yezerets, A.; Schneider, W. F.; Miller, J. T.; Delgass, W. N.; Ribeiro, F. H., Identification of the active Cu site in standard selective catalytic reduction with ammonia on Cu-SSZ-13. *J. Catal.* **2014,** *312*, 87-97.

145. Jangjou, Y.; Do, Q.; Gu, Y.; Lim, L.-G.; Sun, H.; Wang, D.; Kumar, A.; Li, J.; Grabow, L. C.; Epling, W. S., Nature of Cu Active Centers in Cu-SSZ-13 and Their Responses to SO2 Exposure. *ACS Catal.* **2018,** *8* (2), 1325-1337.

146. Lomachenko, K. A.; Borfecchia, E.; Negri, C.; Berlier, G.; Lamberti, C.; Beato, P.; Falsig, H.; Bordiga, S., The Cu-CHA deNOx Catalyst in Action: Temperature-Dependent NH3-Assisted Selective Catalytic Reduction Monitored by Operando XAS and XES. *J. Am. Chem. Soc.* **2016,** *138* (37), 12025-12028.

147. Krishna, S. H.; Jones, C. B.; Gounder, R., Temperature dependence of Cu(I) oxidation and Cu(II) reduction kinetics in the selective catalytic reduction of NOx with NH3 on Cu-chabazite zeolites. *J. Catal.* **2021,** *404*, 873-882.

148. Paolucci, C.; Di Iorio, J. R.; Schneider, W. F.; Gounder, R., Solvation and Mobilization of Copper Active Sites in Zeolites by Ammonia: Consequences for the Catalytic Reduction of Nitrogen Oxides. *Acc. Chem. Res.* **2020,** *53* (9), 1881-1892.

149. Zhang, T.; Qiu, F.; Chang, H.; Li, X.; Li, J., Identification of active sites and reaction mechanism on low-temperature SCR activity over Cu-SSZ-13 catalysts prepared by different methods. *Catal. Sci. Technol* **2016,** *6* (16), 6294-6304.

150. Gao, F.; Peden, C. H. F., Recent Progress in Atomic-Level Understanding of Cu/SSZ-13 Selective Catalytic Reduction Catalysts. *Catalysts* **2018,** *8* (4), 140.

151. Borfecchia, E.; Lomachenko, K. A.; Giordanino, F.; Falsig, H.; Beato, P.; Soldatov, A. V.; Bordiga, S.; Lamberti, C., Revisiting the nature of Cu sites in the activated Cu-SSZ-13 catalyst for SCR reaction. *Chemical Science* **2015,** *6* (1), 548-563.

152. Paolucci, C.; Parekh, A. A.; Khurana, I.; Di Iorio, J. R.; Li, H.; Albarracin Caballero, J. D.; Shih, A. J.; Anggara, T.; Delgass, W. N.; Miller, J. T.; Ribeiro, F. H.; Gounder, R.; Schneider, W. F., Catalysis in a Cage: Condition-Dependent Speciation and Dynamics of Exchanged Cu Cations in SSZ-13 Zeolites. *J. Am. Chem. Soc.* **2016,** *138* (18), 6028-6048.

153. Martini, A.; Borfecchia, E.; Lomachenko, K. A.; Pankin, I. A.; Negri, C.; Berlier, G.; Beato, P.; Falsig, H.; Bordiga, S.; Lamberti, C., Composition-driven Cu-speciation and reducibility in Cu-CHA zeolite catalysts: a multivariate XAS/FTIR approach to complexity. *Chemical Science* **2017,** *8* (10), 6836-6851.

154. Li, H.; Paolucci, C.; Khurana, I.; Wilcox, Laura N.; Göltl, F.; Albarracin-Caballero, J. D.; Shih, A. J.; Ribeiro, F. H.; Gounder, R.; Schneider, W. F., Consequences of exchange-site heterogeneity and dynamics on the UV-visible spectrum of Cu-exchanged SSZ-13. *Chemical Science* **2019,** *10* (8), 2373-2384.

155. Negri, C.; Signorile, M.; Porcaro, N. G.; Borfecchia, E.; Berlier, G.; Janssens, T. V. W.; Bordiga, S., Dynamic CuII/CuI speciation in Cu-CHA catalysts by in situ Diffuse Reflectance UV–vis-NIR spectroscopy. *Appl. Catal. A: Gen.* **2019,** *578*, 1-9.

156. Hun Kwak, J.; Zhu, H.; Lee, J. H.; Peden, C. H. F.; Szanyi, J., Two different cationic positions in Cu-SSZ-13? *Chem. Commun.* **2012,** *48* (39), 4758-4760.

157. Kwak, J. H.; Varga, T.; Peden, C. H. F.; Gao, F.; Hanson, J. C.; Szanyi, J., Following the movement of Cu ions in a SSZ-13 zeolite during dehydration, reduction and adsorption: A combined in situ TP-XRD, XANES/DRIFTS study. *J. Catal.* **2014,** *314*, 83-93.

158. Bregante, D. T.; Wilcox, L. N.; Liu, C.; Paolucci, C.; Gounder, R.; Flaherty, D. W., Dioxygen Activation Kinetics over Distinct Cu Site Types in Cu-Chabazite Zeolites. *ACS Catal.* **2021,** *11* (19), 11873-11884.

159. Godiksen, A.; Stappen, F. N.; Vennestrøm, P. N. R.; Giordanino, F.; Rasmussen, S. B.; Lundegaard, L. F.; Mossin, S., Coordination Environment of Copper Sites in Cu-CHA Zeolite Investigated by Electron Paramagnetic Resonance. *J. Phys. Chem. C.* **2014,** *118* (40), 23126-23138.

160. Gao, F.; Walter, E. D.; Karp, E. M.; Luo, J.; Tonkyn, R. G.; Kwak, J. H.; Szanyi, J.; Peden, C. H. F., Structure–activity relationships in NH3-SCR over Cu-SSZ-13 as probed by reaction kinetics and EPR studies. *J. Catal.* **2013,** *300*, 20-29.

161. Borfecchia, E.; Beato, P.; Svelle, S.; Olsbye, U.; Lamberti, C.; Bordiga, S., Cu-CHA – a model system for applied selective redox catalysis. *Chem. Soc. Rev.* **2018,** *47* (22), 8097-8133.

162. Gao, F.; Washton, N. M.; Wang, Y.; Kollár, M.; Szanyi, J.; Peden, C. H. F., Effects of Si/Al ratio on Cu/SSZ-13 NH3-SCR catalysts: Implications for the active Cu species and the roles of Brønsted acidity. *J. Catal.* **2015,** *331*, 25-38.

163. Shan, Y.; Du, J.; Yu, Y.; Shan, W.; Shi, X.; He, H., Precise control of post-treatment significantly increases hydrothermal stability of in-situ synthesized cu-zeolites for NH3-SCR reaction. *Applied Catalysis B: Environmental* **2020,** *266*, 118655.

164. Shih, A. J.; González, J. M.; Khurana, I.; Ramírez, L. P.; Peña L, A.; Kumar, A.; Villa, A. L., Influence of ZCuOH, Z2Cu, and Extraframework CuxOy Species in Cu-SSZ-13 on N2O Formation during the Selective Catalytic Reduction of NOx with NH3. *ACS Catal.* **2021,** *11* (16), 10362-10376.

165. Villamaina, R.; Liu, S.; Nova, I.; Tronconi, E.; Ruggeri, M. P.; Collier, J.; York, A.; Thompsett, D., Speciation of Cu Cations in Cu-CHA Catalysts for NH3-SCR: Effects of SiO2/AlO3 Ratio and Cu-Loading Investigated by Transient Response Methods. *ACS Catal.* **2019,** *9* (10), 8916-8927.

166. Kim, Y. J.; Lee, J. K.; Min, K. M.; Hong, S. B.; Nam, I.-S.; Cho, B. K., Hydrothermal stability of CuSSZ13 for reducing NOx by NH3. *J. Catal.* **2014,** *311*, 447-457.

167. Luo, J.; Gao, F.; Kamasamudram, K.; Currier, N.; Peden, C. H. F.; Yezerets, A., New insights into Cu/SSZ-13 SCR catalyst acidity. Part I: Nature of acidic sites probed by NH3 titration. *J. Catal.* **2017,** *348*, 291-299.

168. Pappas, D. K.; Borfecchia, E.; Dyballa, M.; Pankin, I. A.; Lomachenko, K. A.; Martini, A.; Signorile, M.; Teketel, S.; Arstad, B.; Berlier, G.; Lamberti, C.; Bordiga, S.; Olsbye, U.; Lillerud, K. P.; Svelle, S.; Beato, P., Methane to Methanol: Structure–Activity Relationships for Cu-CHA. *J. Am. Chem. Soc.* **2017,** *139* (42), 14961-14975.

169. Negri, C.; Martini, A.; Deplano, G.; Lomachenko, K. A.; Janssens, T. V. W.; Borfecchia, E.; Berlier, G.; Bordiga, S., Investigating the role of Cu-oxo species in Cu-nitrate formation over Cu-CHA catalysts. *PCCP* **2021,** *23* (34), 18322-18337.

170. Rhoda, H. M.; Plessers, D.; Heyer, A. J.; Bols, M. L.; Schoonheydt, R. A.; Sels, B. F.; Solomon, E. I., Spectroscopic Definition of a Highly Reactive Site in Cu-CHA for Selective Methane Oxidation: Tuning a Mono-μ-Oxo Dicopper(II) Active Site for Reactivity. *J. Am. Chem. Soc.* **2021,** *143* (19), 7531-7540.

171. Göltl, F.; Bhandari, S.; Lebrón-Rodríguez, E. A.; Gold, J. I.; Zones, S. I.; Hermans, I.; Dumesic, J. A.; Mavrikakis, M., Identifying hydroxylated copper dimers in SSZ-13 via UV-vis-NIR spectroscopy. *Catal. Sci. Technol* **2022**.

172. Göltl, F.; Bhandari, S.; Mavrikakis, M., Thermodynamics Perspective on the Stepwise Conversion of Methane to Methanol over Cu-Exchanged SSZ-13. *ACS Catal.* **2021**, 7719-7734.

173. Ipek, B.; Wulfers, M. J.; Kim, H.; Göltl, F.; Hermans, I.; Smith, J. P.; Booksh, K. S.; Brown, C. M.; Lobo, R. F., Formation of [Cu2O2]2+ and [Cu2O]2+ toward C–H Bond Activation in Cu-SSZ-13 and Cu-SSZ-39. *ACS Catal.* **2017,** *7* (7), 4291-4303.

174. Szanyi, J.; Kwak, J. H.; Zhu, H.; Peden, C. H. F., Characterization of Cu-SSZ-13 NH3 SCR catalysts: an in situ FTIR study. *PCCP* **2013,** *15* (7), 2368-2380.

175. Lee, H.; Song, I.; Jeon, S. W.; Kim, D. H., Inter-particle migration of Cu ions in physically mixed Cu-SSZ-13 and H-SSZ-13 treated by hydrothermal aging. *Reaction Chemistry & Engineering* **2019,** *4* (6), 1059-1066.

176. Di Iorio, J. R.; Gounder, R., Controlling the Isolation and Pairing of Aluminum in Chabazite Zeolites Using Mixtures of Organic and Inorganic Structure-Directing Agents. *Chem. Mater.* **2016,** *28* (7), 2236-2247.

177. Verma, A. A.; Bates, S. A.; Anggara, T.; Paolucci, C.; Parekh, A. A.; Kamasamudram, K.; Yezerets, A.; Miller, J. T.; Delgass, W. N.; Schneider, W. F.; Ribeiro, F. H., NO oxidation: A probe reaction on Cu-SSZ-13. *J. Catal.* **2014,** *312*, 179-190.

178. Concepción, P.; Boronat, M.; Millán, R.; Moliner, M.; Corma, A., Identification of Distinct Copper Species in Cu-CHA Samples Using NO as Probe Molecule. A Combined IR Spectroscopic and DFT Study. *Top. Catal.* **2017,** *60* (19), 1653-1663.

179. Göltl, F.; Sautet, P.; Hermans, I., Can Dynamics Be Responsible for the Complex Multipeak Infrared Spectra of NO Adsorbed to Copper(II) Sites in Zeolites? *Angew. Chem. Int. Ed.* **2015,** *54* (27), 7799-7804.

180. Sushkevich, V. L.; van Bokhoven, J. A., Revisiting copper reduction in zeolites: the impact of autoreduction and sample synthesis procedure. *Chem. Commun.* **2018,** *54* (54), 7447-7450.

181. Palagin, D.; Sushkevich, V. L.; Knorpp, A. J.; Ranocchiari, M.; van Bokhoven, J. A., Mapping Vibrational Spectra to the Structures of Copper Species in Zeolites Based on Calculated Stretching Frequencies of Adsorbed Nitrogen and Carbon Monoxides. *J. Phys. Chem. C.* **2021,** *125* (22), 12094-12106.

182. Knorpp, A. J.; Pinar, A. B.; Baerlocher, C.; McCusker, L. B.; Casati, N.; Newton, M. A.; Checchia, S.; Meyet, J.; Palagin, D.; van Bokhoven, J. A., Paired Copper Monomers in Zeolite Omega: The Active Site for Methane-to-Methanol Conversion. *Angew. Chem. Int. Ed.* **2021,** *60* (11), 5854-5858.

183. Göltl, F.; Love, A. M.; Schuenzel, S. C.; Wolf, P.; Mavrikakis, M.; Hermans, I., Computational description of key spectroscopic features of zeolite SSZ-13. *PCCP* **2019,** *21* (35), 19065-19075.

184. Davydov, A. A.; Budneva, A. A., IR spectra of CO and NO adsorbed on CuO. *React. Kinet. Catal. Lett.* **1984,** *25* (1), 121-124.

185. Kuterasiński, Ł.; Podobiński, J.; Rutkowska-Zbik, D.; Datka, J., IR Studies of the Cu Ions in Cu-Faujasites. *Molecules* **2019,** *24* (23), 4250.

186. Wang, B.; Jin, M.; An, H.; Guo, Z.; Lv, Z., Hydrogenation Performance of Acetophenone to 1-Phenylethanol on Highly Active Nano Cu/SiO2 Catalyst. *Catal. Lett.* **2020,** *150* (1), 56-64.

187. Xu, J.; Armstrong, R. D.; Shaw, G.; Dummer, N. F.; Freakley, S. J.; Taylor, S. H.; Hutchings, G. J., Continuous selective oxidation of methane to methanol over Cu- and Fe-modified ZSM-5 catalysts in a flow reactor. *Catal. Today* **2016,** *270*, 93-100.

188. Sheppard, T.; Hamill, C. D.; Goguet, A.; Rooney, D. W.; Thompson, J. M., A low temperature, isothermal gas-phase system for conversion of methane to methanol over Cu–ZSM-5. *Chem. Commun.* **2014,** *50* (75), 11053-11055.

189. Tomkins, P.; Ranocchiari, M.; van Bokhoven, J. A., Direct Conversion of Methane to Methanol under Mild Conditions over Cu-Zeolites and beyond. *Acc. Chem. Res.* **2017,** *50* (2), 418-425.

190. Groothaert, M. H.; Smeets, P. J.; Sels, B. F.; Jacobs, P. A.; Schoonheydt, R. A., Selective Oxidation of Methane by the Bis(μ-oxo)dicopper Core Stabilized on ZSM-5 and Mordenite Zeolites. *J. Am. Chem. Soc.* **2005,** *127* (5), 1394-1395.

191. Vanelderen, P.; Hadt, R. G.; Smeets, P. J.; Solomon, E. I.; Schoonheydt, R. A.; Sels, B. F., Cu-ZSM-5: A biomimetic inorganic model for methane oxidation. *J. Catal.* **2011,** *284* (2), 157-164.

192. Wang, Q.; Chen, X.; Jha, A. N.; Rogers, H., Natural gas from shale formation – The evolution, evidences and challenges of shale gas revolution in United States. *Renew. Sust. Energ. Rev.* **2014,** *30*, 1-28.

193. Pontzen, F.; Liebner, W.; Gronemann, V.; Rothaemel, M.; Ahlers, B., CO2-based methanol and DME – Efficient technologies for industrial scale production. *Catal. Today* **2011,** *171* (1), 242-250.

194. Ravi, M.; Ranocchiari, M.; van Bokhoven, J. A., The Direct Catalytic Oxidation of Methane to Methanol—A Critical Assessment. *Angew. Chem. Int. Ed.* **2017,** *56* (52), 16464-16483.

195. Zakaria, Z.; Kamarudin, S. K., Direct conversion technologies of methane to methanol: An overview. *Renew. Sust. Energ. Rev.* **2016,** *65*, 250-261.

196. Gesser, H. D.; Hunter, N. R.; Prakash, C. B., The direct conversion of methane to methanol by controlled oxidation. *Chem. Rev.* **1985,** *85* (4), 235-244.

197. Foster, N. R., Direct catalytic oxidation of methane to methanol — a review. *Applied Catalysis* **1985,** *19* (1), 1-11.

198. Borfecchia, E.; Pappas, D. K.; Dyballa, M.; Lomachenko, K. A.; Negri, C.; Signorile, M.; Berlier, G., Evolution of active sites during selective oxidation of methane to methanol over Cu-CHA and Cu-MOR zeolites as monitored by operando XAS. *Catal. Today* **2019,** *333*, 17-27.

199. Brezicki, G.; Zheng, J.; Paolucci, C.; Schlögl, R.; Davis, R. J., Effect of the Co-cation on Cu Speciation in Cu-Exchanged Mordenite and ZSM-5 Catalysts for the Oxidation of Methane to Methanol. *ACS Catal.* **2021,** *11* (9), 4973-4987.

200. Markovits, M. A. C.; Jentys, A.; Tromp, M.; Sanchez-Sanchez, M.; Lercher, J. A., Effect of Location and Distribution of Al Sites in ZSM-5 on the Formation of Cu-Oxo Clusters Active for Direct Conversion of Methane to Methanol. *Top. Catal.* **2016,** *59* (17), 1554-1563.

201. Wang, X.; Arvidsson, A. A.; Cichocka, M. O.; Zou, X.; Martin, N. M.; Nilsson, J.; Carlson, S.; Gustafson, J.; Skoglundh, M.; Hellman, A.; Carlsson, P.-A., Methanol Desorption from Cu-ZSM-5 Studied by In Situ Infrared Spectroscopy and First-Principles Calculations. *J. Phys. Chem. C.* **2017,** *121* (49), 27389-27398.

202. Beznis, N. V.; Weckhuysen, B. M.; Bitter, J. H., Cu-ZSM-5 Zeolites for the Formation of Methanol from Methane and Oxygen: Probing the Active Sites and Spectator Species. *Catal. Lett.* **2010,** *138* (1), 14-22.

203. Woertink, J. S.; Smeets, P. J.; Groothaert, M. H.; Vance, M. A.; Sels, B. F.; Schoonheydt, R. A.; Solomon, E. I., A [Cu₂O]²⁺ core in Cu-ZSM-5, the active site in the oxidation of methane to methanol. *Proc. Natl. Acad. Sci.* **2009,** *106* (45), 18908-18913.

204. Smeets, P. J.; Hadt, R. G.; Woertink, J. S.; Vanelderen, P.; Schoonheydt, R. A.; Sels, B. F.; Solomon, E. I., Oxygen Precursor to the Reactive Intermediate in Methanol Synthesis by Cu-ZSM-5. *J. Am. Chem. Soc.* **2010,** *132* (42), 14736-14738.

205. Wu, J.-F.; Gao, X.-D.; Wu, L.-M.; Wang, W. D.; Yu, S.-M.; Bai, S., Mechanistic Insights on the Direct Conversion of Methane into Methanol over Cu/Na–ZSM-5 Zeolite: Evidence from EPR and Solid-State NMR. *ACS Catal.* **2019,** *9* (9), 8677-8681.

206. Mota, N.; Millán Ordoñez, E.; Pawelec, B.; Fierro, J. L. G.; Navarro, R. M., Direct Synthesis of Dimethyl Ether from CO2: Recent Advances in Bifunctional/Hybrid Catalytic Systems. *Catalysts* **2021,** *11* (4), 411.

207. Millán, E.; Mota, N.; Guil-López, R.; Pawelec, B.; García Fierro, J. L.; Navarro, R. M., Direct Synthesis of Dimethyl Ether from Syngas on Bifunctional Hybrid Catalysts Based on Supported H3PW12O40 and Cu-ZnO(Al): Effect of Heteropolyacid Loading on Hybrid Structure and Catalytic Activity. *Catalysts* **2020,** *10* (9), 1071.

208. Catizzone, E.; Bonura, G.; Migliori, M.; Frusteri, F.; Giordano, G., CO2 Recycling to Dimethyl Ether: State-of-the-Art and Perspectives. *Molecules* **2018,** *23* (1), 31.

209. Zhang, D.; Yang, R. T., N2O Formation Pathways over Zeolite-Supported Cu and Fe Catalysts in NH3-SCR. *Energy Fuels* **2018,** *32* (2), 2170-2182.

210. Liu, B.; Yao, D.; Wu, F.; Wei, L.; Li, X.; Wang, X., Experimental Investigation on N2O Formation during the Selective Catalytic Reduction of NOx with NH3 over Cu-SSZ-13. *Ind. Eng. Chem. Res.* **2019,** *58* (45), 20516-20527.

211. Feng, Y.; Janssens, T. V. W.; Vennestrøm, P. N. R.; Jansson, J.; Skoglundh, M.; Grönbeck, H., The Role of H+- and Cu+-Sites for N2O Formation during NH3-SCR over Cu-CHA. *J. Phys. Chem. C.* **2021,** *125* (8), 4595-4601.

212. Pérez-Ramírez, J.; Kapteijn, F.; Schöffel, K.; Moulijn, J. A., Formation and control of N2O in nitric acid production: Where do we stand today? *Applied Catalysis B: Environmental* **2003,** *44* (2), 117-151.

213. Ravishankara, A. R.; Daniel, J. S.; Portmann, R. W., Nitrous Oxide (N₂O): The Dominant Ozone-Depleting Substance Emitted in the 21st Century. *Science.* **2009,** *326* (5949), 123-125.

214. Skiba, U.; Jones, S. K.; Dragosits, U.; Drewer, J.; Fowler, D.; Rees, R. M.; Pappa, V. A.; Cardenas, L.; Chadwick, D.; Yamulki, S.; Manning, A. J., UK emissions of the greenhouse gas nitrous oxide. *Philosophical Transactions of the Royal Society B: Biological Sciences* **2012,** *367* (1593), 1175-1185.

215. Muñoz, C.; Paulino, L.; Monreal, C.; Zagal, E., Greenhouse gas (CO2 and N2O) emissions from soils: a review. *Chilean journal of agricultural research* **2010,** *70* (3), 485-497.

216. Qin, K.; Guo, L.; Ming, S.; Zhang, S.; Guo, Y.; Pang, L.; Li, T., The Comparative Study of Reaction Mechanisms and Catalytic Performances of Cu–SSZ-13 and Fe–SSZ-13 for the NH3-SCR Reaction. *Catalysis Surveys from Asia* **2022**.

217. Gao, F., Fe-Exchanged Small-Pore Zeolites as Ammonia Selective Catalytic Reduction (NH3-SCR) Catalysts. *Catalysts* **2020,** *10* (11), 1324.

218. Gao, F.; Zheng, Y.; Kukkadapu, R. K.; Wang, Y.; Walter, E. D.; Schwenzer, B.; Szanyi, J.; Peden, C. H. F., Iron Loading Effects in Fe/SSZ-13 NH3-SCR Catalysts: Nature of the Fe Ions and Structure–Function Relationships. *ACS Catal.* **2016,** *6* (5), 2939-2954.

219. Bols, M. L.; Rhoda, H. M.; Snyder, B. E. R.; Solomon, E. I.; Pierloot, K.; Schoonheydt, R. A.; Sels, B. F., Advances in the synthesis, characterisation, and mechanistic understanding of active sites in Fe-zeolites for redox catalysts. *Dalton Trans.* **2020,** *49* (42), 14749-14757.

220. Zhang, T.; Qiu, Y.; Liu, G.; Chen, J.; Peng, Y.; Liu, B.; Li, J., Nature of active Fe species and reaction mechanism over high-efficiency Fe/CHA catalysts in catalytic decomposition of N2O. *J. Catal.* **2020,** *392*, 322-335.

221. Gao, F.; Kollár, M.; Kukkadapu, R. K.; Washton, N. M.; Wang, Y.; Szanyi, J.; Peden, C. H. F., Fe/SSZ-13 as an NH3-SCR catalyst: A reaction kinetics and FTIR/Mössbauer spectroscopic study. *Applied Catalysis B: Environmental* **2015,** *164*, 407-419.

222. Szanyi, J.; Gao, F.; Kwak, J. H.; Kollár, M.; Wang, Y.; Peden, C. H. F., Characterization of Fe2+ ions in Fe,H/SSZ-13 zeolites: FTIR spectroscopy of CO and NO probe molecules. *PCCP* **2016,** *18* (15), 10473-10485.

223. Zhang, R.; Anderst, E.; Groden, K.; McEwen, J.-S., Modeling the Adsorption of NO and NH3 on Fe-SSZ-13 from First-Principles: A DFT Study. *Ind. Eng. Chem. Res.* **2018,** *57* (40), 13396-13405.

224. Aguirre, A.; Collins, S. E., Design of an optimized DRIFT cell/microreactor for spectrokinetic investigations of surface reaction mechanisms. *Molecular Catalysis* **2020,** *481*, 100628.

225. Qi, L.; Alamillo, R.; Elliott, W. A.; Andersen, A.; Hoyt, D. W.; Walter, E. D.; Han, K. S.; Washton, N. M.; Rioux, R. M.; Dumesic, J. A.; Scott, S. L., Operando Solid-State NMR Observation of Solvent-Mediated Adsorption-Reaction of Carbohydrates in Zeolites. *ACS Catal.* **2017,** *7* (5), 3489-3500.

226. Feng, W.; Wang, Y.; Wu, G.; Lin, Y.; Xu, J.; Shi, H.; Zhang, T.; Wang, S.; Wu, X.; Yao, P., Liquid phase propylene epoxidation with H2O2 on TS-1/SiO2 catalyst in a fixed-bed reactor: experiments and deactivation kinetics. *J. Chem. Technol. Biotechnol.* **2015,** *90* (8), 1489-1496.

227. Bregante, D. T.; Potts, D. S.; Kwon, O.; Ayla, E. Z.; Tan, J. Z.; Flaherty, D. W., Effects of Hydrofluoric Acid Concentration on the Density of Silanol Groups and Water Adsorption in Hydrothermally Synthesized Transition-Metal-Substituted Silicalite-1. *Chem. Mater.* **2020,** *32* (17), 7425-7437.

228. Gordon, C. P.; Engler, H.; Tragl, A. S.; Plodinec, M.; Lunkenbein, T.; Berkessel, A.; Teles, J. H.; Parvulescu, A.-N.; Copéret, C., Efficient epoxidation over dinuclear sites in titanium silicalite-1. *Nature* **2020,** *586* (7831), 708-713.

229. Tan, J. Z.; Bregante, D. T.; Torres, C.; Flaherty, D. W., Transition state stabilization depends on solvent identity, pore size, and hydrophilicity for epoxidations in zeolites. *J. Catal.* **2022,** *405*, 91-104.